January 2022

Development Of Biomass-Derived Nanoparticles For Biological And Medical Applications

Sarah Elizabeth Reagen

DEVELOPMENT OF BIOMASS-DERIVED NANOPARTICLES FOR BIOLOGICAL AND MEDICAL APPLICATIONS

by

Sarah E. Reagen

B.S. Chemistry, University of North Dakota, 2018

A Dissertation

Submitted to the Graduate Faculty

of the

University of North Dakota

in partial fulfillment of the requirements

For the degree of

Doctor of Philosophy

Grand Forks, North Dakota

August 2022

Name: Sarah Reagen

Degree: Doctor of Philosophy

This document, submitted in partial fulfillment of the requirements for the degree from the University of North Dakota, has been read by the Faculty Advisory Committee under whom the work has been done and is hereby approved.

DocuSigned by:
Dr. Julia Xiaojun Zhao
Julia Zhao

DocuSigned by:
Alena Kubatova
Alena Kubatova

DocuSigned by:
David Pierce
David Pierce

DocuSigned by:
Evguenii Kozliak
Evguenii Kozliak

DocuSigned by:
Yun Ji
Yun Ji

This document is being submitted by the appointed advisory committee as having met all the requirements of the School of Graduate Studies at the University of North Dakota and is hereby approved.

DocuSigned by:
Chris Nelson
Chris Nelson
Dean of the School of Graduate Studies

7/26/2022
Date

PERMISSION

Title: Development of biomass-derived nanoparticles for biological and medical applications

Department: Chemistry

Degree: Doctor of Philosophy

In presenting this document in partial fulfillment of the requirements for a graduate degree in philosophy from the University of North Dakota, I agree that the library at this university can make inspection freely available. Extensive copying for scholarly purposes may be granted by the professor who supervised this dissertation work or, in his/her absence, by the Chairperson of the department or Dean of the Graduate School. My written permission is required for any copying, publication, or other use of this dissertation for financial gain. Recognition is also required to be given to me and to the University of North Dakota for any scholarly use which consists of any material in my dissertation.

Sarah E. Reagen

August 2022

ABBREVIATIONS

AIHA	American Industrial Hygiene Association
BALF	Bronchoalveolar Lavage Fluid
CAPS	3-(cyclhexylamino)-1-propanesulfonic acid
CBDA-2	*Cis*-3,4-di(furan-2-yl)cyclobutane-1,2-dicarboxylic acid
CHES	2-(cyclohexylamino)ethanesulfonic acid
DLS	Dynamic Light Scattering
ENMs	Engineered Nanomaterials
FE-TEM	Field Emission-Transmission Electron Microscopy
FT-IR	Fourier Transform Infrared Spectrometry
GQDs	Graphene Quantum Dots
HEPES	2-[4-(2-hydroxyethyl)piperazin-1-yl]ethanesulfonic acid
hMSNs	Hollow Mesoporous Silica Nanoparticles
hPDLF	Human Periodontal Ligament Fibroblasts
HRTEM	High Resolution Transmission Electron Microscopy
ICP-MS	Inductively Coupled Plasma Mass Spectrometry
ICP-Q-MS	Inductively Coupled Plasma Quadrupole Mass Spectrometry
ICP-SF-MS	Inductively Coupled Plasma Sector Field Mass Spectrometry

KC-GRO	Keratinocyte Chemoattractant Growth-regulated Oncogene
LDH	Lactate Dehydrogenase
mALB	Micro-Albumin
mDF	Mouse Dermal Fibroblast
mTP	Micro-total Protein
MTT	3-[4,5-dimethylthiazole-2-yl]-2,5-diphenyltetrazolium bromide
MWCNTs	Multiwalled Carbon Nanotubes
NIR	Near Infrared
NPs	Nanoparticles
OECD	Organization for Economic Co-operation and Development
PEO	Post Exposure
PGQDs	Porphyrin Graphene Quantum Dots
QDs	Quantum Dots
QY	Quantum Yield
ROS	Reactive Oxidative Species
SEI-XPS	Sputtering-enabled Intracellular X-ray Photoelectron Spectroscopy
SEM	Scanning Electron Microscopy
SWCNT	Single-walled Carbon Nanotubes

TCPP	Meso-tetra(4-carboxyphenyl)porphine
TEM	Transmission Electron Microscopy
TNF-alpha	Tumor Necrosis Factor-alpha
USEPA	United States Environmental Protection Agency
UV-Vis	Ultraviolet-Visible
XPS	X-ray Photoelectron Spectroscopy
XRD	X-ray Diffraction

TABLE OF CONTENTS

LIST OF FIGURES

Figure Page

LIST OF TABLES

Table Page

LIST OF SCHEMES

Scheme Page

ACKNOWLEDGEMENTS

I'd like to thank my advisor, Dr. Julia Zhao, for all her support and encouragement during my time in graduate school, and helping to mold me into a better scientist. Thank you to my committee members, Dr. David Pierce, Dr. Alena Kubátová, Dr. Evguenii Kozliak, and Dr. Yun Ji, for assisting me throughout the years and for their valuable assistance on my research. I'd also like to thank the faculty members in the chemistry department for contributing to my education and helping me learn how to better teach laboratories and outreach events. I'm also grateful to my group members, Wen Sun, Di Sun, Yingfen Wu, Juan Han, Xiao Liu, and Sultan Mahmud, for their support and assistance both inside and outside of the lab.

To my non-group member friends, Jessica Emond, Audrey LaVallie, and Solène Bechelli, thank you for always lending assistance and feedback, and for being a listening ear when times were hard. I'm also grateful to the entire chemistry graduate student body and the friends I've made along the way for always having a strong sense of community where we look out for one another and help each other in whatever way we can.

Thank you to my wonderful parents, William and Deborah Reagen. I would never have made it this far in chemistry without my dad and graduate school was made possible knowing I could turn to him with any question. My mom has always been my North Star, I've turned to her countless times for advice and emotional support, I'd be lost without her guidance. Thank you, as well, to my brothers Ian, Ben, and Max Reagen for being there when I needed them most. Although we don't talk as much as we used to, the unspoken truth is that we're always waiting nearby should we need each other.

ABSTRACT

Quantum dots (QDs) are a subset of nanoparticles (NPs) that have several unique optical and electrical properties that make them viable for fluorescent cell labeling applications. However, these QDs in the past were composed of toxic heavy metals such as lead and cadmium, and therefore, graphene-based QDs (GQDs) have been examined as an alternative material for these cell labeling applications for their increased biocompatibility. Furthermore, GQDs can produced singlet oxygen ($^1O_2$) for photodynamic therapy (PDT), making them capable of being used as a PS agent for cancer treatment. Additionally, hollow mesoporous silica nanoparticles (hMSNs) are capable of being an alternative treatment to cancer as hMSNs have displayed exceptional drug loading and delivery abilities. The work described in this dissertation will have four primary goals that are all essential for fluorescent cell imaging and cancer treatment using QDs and NPs. The first goal is to investigate current analytical methods for NPs toxicity determination and detection, as well as new protocols for toxicity evaluation. The second goal is to synthesize GQDs using biomass-derived material and hMSNs by a modified Stöber method to improve their biocompatibility and biodegradation. The third is to characterize the newly synthesized GQDs and hMSNs using various analytical methods to better determine their chemical and physical properties. The final goal is to apply the GQDs for fluorescent cell imaging and PDT treatment applications, and the hMSNs for drug loading and delivery into cancer cells.

The first project focuses on the investigation of current and advancing analytical methods for nanotoxicity determination and nanoparticle detection. The advancing field of nanoscience has produced lower mass, smaller size, and expanded chemical composition nanoparticles over recent years. These new nanoparticles have challenged traditional analytical methods in terms of qualitative and quantitative analysis. Such advancements of nanoparticles and nanomaterials have

captured the attention of toxicologists with concerns regarding the environment and human health impacts.

The second project focuses on graphene quantum dots (GQDs), a subset of fluorescent nanomaterials, that have piqued recent interest due to their photoluminescence properties, low toxicity and biocompatibility features for bioanalysis and bioimaging. However, it is still a challenge to prepare highly near-infrared (NIR) fluorescent GQDs using a facile pathway. In this project, NIR GQDs were synthesized from the biomass-derived organic molecule, *cis*-cyclobutane-1,2-dicarboxylic acid and their applicability for cell-labeling was tested using RAW 264.7 and MCF-7 cells.

The third project focuses on red and near infrared emission GQDs, which is a highly desirable feature for fluorescent nanoparticles in biological applications. This is mainly due to longer wavelengths which may penetrate tissues, organs, skin, and other organic components while less autofluorescence interference is produced. Additionally, GQDs that contain unique optical and electrical features have been targeted for their use in cell labeling applications as well as environmental analysis. However, GQDs are frequently reported to have blue-green emission light and not the more advantageous red/NIR emission light. Furthermore, porphyrins are a subgroup of heterocyclic macrocycle organic compounds and have been used previously to synthesize nanomaterials and for nanoparticle doping in order to incorporate the red/NIR emission light property into particles that otherwise do not contain the desired emission light. Meso-tetra(4-carboxyphenyl)porphine (TCPP) is one type of porphyrin with a large conjugated π-electron system and four carboxyl groups on its exterior benzene rings. These two key characteristics of TCPP makes it ideal for incorporation into GQDs as it would design and synthesize red-emissive material as well as give rise to excellent water solubility. In this work, TCPP is used in tangent

with *cis*-cyclobutane-1,2-dicarboxylic acid (CBDA-2), a biomass derived organic molecule, to synthesize “green” porphyrin-based graphene quantum dots (PGQDs) with red-emission. Their imaging application was tested using HeLa cells via confocal microscopy.

In the fourth project, the GQDs used previously were combined with silica-based nanoparticles for fluorescent imaging and dual cancer treatment applications. Nano-based cancer therapeutics have been researched and developed, with some nanomaterials being shown to possess anticancer properties. GQDs are one such class of nanoparticles due to their valuable characteristics such as photoluminescence, biocompatibility, and water solubility. When it comes to cancer treatment, GQDs contain the ability to generate $^1O_2$, a reactive oxidative species (ROS), allowing for the synergistic imaging and photodynamic therapy (PDT) of cancer. However, due to their small particle size, GQDs struggle to remain in the target area for long periods of time in addition to being poor drug carriers. To combat this, hollow mesoporous silica nanoparticles (hMSNs) have been extensively researched for drug delivery applications. hMSNs also contain exceptional biocompatibility in addition to high drug-loading capacities and easy surface functionalization. This project investigates the utilization and combination of GQDs and hMSNs to make GQDs-hMSNs for an enhanced double treatment of cancer; using GQDs for $^1O_2$ generation and fluorescent imaging *in vitro* that would have biodegradable hMSNs synthesized around them to serve as the drug deliverer into the target cancer cell. RAW 264.7 cells were utilized again for the GQDs-hMSNs biological and medical applicational use.

CHAPTER I

INTRODUCTION TO GRAPHENE QUANTUM DOTS AND SILICA NANOPARTICLES

1.1. Background and research importance

Nanoparticles (NPs) are a class of engineered particles defined and limited by their size definition, being that one dimension must be within 1-100 nm.[1] However, this is only a limit of size and therefore nanoparticles contain a diverse field of composition from elemental makeup, surface modification, shape, and size range (within 1-100 nm). Due to this feature, nanoparticles can be found in a broad range of research disciplines as they can be freely modified to fit the needs of various target applications.

Although nanoscience can be traced back to the early 5th century B.C., it wasn't until the late 1950s that the field of nanotechnology was developed.[2] The establishment of this field of study allowed for extensive research and utilization of nanoparticles and nanomaterials in order to further develop their applicational uses in essential disciplines such as chemistry, physics, biology, and medicine.[2] Today, nanoparticles have been incorporated into every-day items such as sunscreens[3], textiles[4], food preservatives[5], and water filters[6] to name a few.

Cancer is one of the leading causes of death worldwide as of 2017.[7] Since its discovery, researchers have been trying to find new alternatives to harsh treatment methods such as chemotherapy and radiology that are not as taxing on the patient.[8] Additionally, scientists have been searching for ways to better detect cancer early on to help treat the patient before questionable areas become malignant. One problem circling early cancer detection is the current limitation of fluorescent cell labeling dyes, such as FITC, AlexaFluor, etc. These traditional dyes suffer from

poor photostability and fluorescence quenching, which all contribute to short analysis times of potential cancerous cells.[9]

Nanotechnology is one such area of research that has been looking at ways to utilize NPs for both cancer imaging and detection, in addition to cancer treatment.[10] Quantum dots (QDs) are a subset of NPs with unique optical and electrical properties that are further defined by their size range of 1-10 nm.[11] Because NPs and QDs can be drastically altered in terms of their shape, elemental composition, surface modification, and size distribution, it is difficult to predict successful synthesis methods that result in the desired or designed NPs.[12,13] Furthermore, NPs and QDs in the past have been composed of heavy metals such as lead and cadmium, which are toxic to biological matrices and therefore are not useful in biological and medical settings.[14]

1.2. Synthesis of nanoparticles

Graphene quantum dots (GQDs) will be synthesized from biomass-derived materials via bottom-up methods, which will make them synthetically green and environmentally friendly.[15] The use of biomass-derived material for the GQDs will also aid in their biocompatibility and decreased cytotoxicity compared to traditional QDs composed of heavy metals.[16] Furthermore, GQDs possess improved fluorescence properties for prolonged imaging applications as well as being natural singlet oxygen ($^1O_2$) generators that allow for their use in photodynamic therapy (PDT) of cancer cells as a photosensitizer (PS).[17]

Additionally, due to GQDs typically containing blue-green emission light, porphyrins (a class of natural pigments that are heterocyclic macrocycle organic compounds) will be investigated as to whether or not they can successfully be doped onto the GQDs surface. This will result in porphyrin graphene quantum dots (PGQDs) that ideally will shift the blue-green fluorescence light

to red emission. This will allow for lower background interference signals, better tissue penetration, and lower cell and tissue damage when investigating their cell imaging applicability.[18]

Furthermore, hollow mesoporous silica nanoparticles (hMSNs) will be synthesized by a slightly modified Stöber method to improve their biodegradation that will assist in avoiding particle accumulation and induced toxicity for drug delivery into cancer cells[19,20]. Lastly, although their introduction into such products is beneficial to better-life development, there are arising concerns of nanotoxicity, particularly around their detection[21], environmental and biological contamination[22,23], and toxicity assessment[24]. Therefore, current and new analytical methods of nanotoxicity and nanoparticle detection will be investigated for challenges surrounding accuracy and certainty.

1.3. Methodologies

There are a variety of analytical methods used to characterize and detect nanoparticles. Several methods need to be used in tandem in order to determine the exact composition, size, lattice, and fluorescence characteristics of the NPs and QDs as many current instruments and methods struggle to accurately detect and measure these small particles.

1.3.1. Morphology and particle size distribution

As stated previously, NPs and QDs have a strict size range limitation of 1-100 nm for NPs and 1-10 nm for QDs. Particle morphology also plays a significant role in biological applications as lattice and surface functional groups impact interactions with cells. To best determine the size distribution of these new particles, a combination of transmission electron microscopy (TEM), high-resolution TEM (HRTEM), and dynamic light scattering (DLS) will be used. TEM and HRTEM allow for the physical observation of the particles for measurement and lattice formation

detection, while DLS provides the average hydrodynamic size range of the particles that also allows for the analysis of concentration agglomeration effects. Additionally, surface morphology analysis will be conducted by zeta potential measurements, which provide information on the surface charge by measuring the electrical potential at the slipping plane. Zeta potential of particles is also valuable to determine for the particles' use in biological applications. Surface charge of the NPs and QDs impact their interaction with the surface of the cell as well as overall particle stability in solution. Therefore, zeta potential data will be collected to determine particle charge and solution stability in different pH conditions.

1.3.2. Elemental composition and lattice formation

Due to the GQDs, PGQDs, and hMSNs use in biological applications, elemental composition must be determined to ensure they are not comprised of toxic elements. Therefore, X-ray photoelectron spectroscopy (XPS), Fourier-transform infrared spectroscopy (FT-IR), and X-ray diffraction (XRD) will be used to determine bond formation and elemental composition of the particles. XPS provides insight into the overall elemental composition with high-resolution scans also providing more in-depth information on the types of bonds present between the elements. FT-IR will help confirm the bonds found in XPS and also provide insight into different functional groups present that can impact particle interaction with cells and toxicity. Lastly, XRD is essential as it provides details on the lattice of the particles. Due to one particle type in this proposal being graphene, it is important to confirm the formation of the graphene lattice, otherwise, the GQDs must be classified as carbon-based particles rather than graphene based.

1.3.3. Optical properties

Cell labeling is one targeted application for these particles and therefore it is vital to characterize the excitation and emission light for fluorescent imaging. To do this, absorption and

fluorescence spectroscopy will be examined. Additionally, pH can cause fluorescence quenching in particles, therefore, the GQDs and PGQDs will be tested in a wide range of pHs (1.0-11.0) to determine any quenching. Lastly, as mentioned previously, traditional fluorescent dyes such as FITC, AlexaFluor, etc. all suffer from poor photostability as their fluorescence signal drastically decreases in a short amount of analysis time. The particles synthesized in this dissertation will ideally provide greater photostability, and thus, this too will be examined.

1.4. Goals of this dissertation

The first goal of this dissertation is to investigate the quickly advancing field of nanoscience and what current and new analytical methods are being applied to detect and measure nanotoxicity. With nanoparticle synthesis and research developing at an expediated rate with more nanoparticles and nanomaterials being incorporated into everyday products, it is essential to understand their impact on biological and environmental systems before toxicity takes place.

The second goal is to find new starting compounds for bottom-up synthesis of GQDs that are more environmentally friendly. Using biomass-derived material is one way to accomplish this. By using compounds that were derived from cornstalks, traditional synthesis conditions and methods can be applied to the new compounds and produce environmentally friendly and synthetically green GQDs for improved biocompatibility and *in vitro* fluorescent imaging. Additionally, since GQDs commonly contain emission fluorescence in the blue-green wavelengths, introducing red-emissive porphyrins, a naturally occurring pigment, into the synthesis will ideally change the fluorescence from blue to red and produced PGQDs. Red-emissive particles contain lower background signals, better tissue penetration, and lower cell damage, making them highly desirable. Lastly, a modified Stöber method will be used to produce

biodegradable hMSNs, that can break down within simulated biological conditions in a few days, avoiding accumulated particles that could induce toxicity.

The third goal is to characterize the newly synthesized GQDs, PGQDs, and GQDs-hMSNs using various analytical methods. It is essential to characterize the new particles in terms of their size distribution, surface charge, elemental composition, functional group formation, photostability, fluorescence excitation and emission, absorbance, and cytotoxicity. To achieve this, instruments such as TEM, HRTEM, DLS, UV-Vis, spectrophotometer, FT-IR, XPS, and XRD will be used in addition to changing the pHs conditions, nanoparticle concentration, and excitation wavelength to determine any agglomeration effects and radiation dependency. MTT and LDH assays will be used for cytotoxicity analysis as the nanoparticles should not induce toxicity within cells.

The fourth goal is to apply the GQDs, PGQDs, and GQDs-hMSNs in different biological and medical applications. All nanoparticles investigated for *in vitro* fluorescent imaging using confocal microscopy. Additionally, the GQDs-hMSNs will be applied in drug delivery and PDT treatment methods for cancer, utilizing FITC as a mock drug and lysosome kits for PDT assessment.

CHAPTER II

ANALYSIS OF NANOMATERIALS IN BIOLOGICAL AND ENVIRONMENTAL SYSTEMS AND NEW ANALYTICAL METHODS FOR IMPROVED DETECTION

2.1. Introduction

Nanoscience has consistently been a developing and advancing field with a great diversity of applications in medicine, energy, electronics, biotechnology, materials, etc.[25] Engineered nanomaterials (ENMs) and nanoparticles (NPs) are simply defined as materials with at least one dimension of 1 - 100 nm in size.[26] This definition means that their various chemical and physical properties allow them to be altered and changed in order to perform their targeted functions and tasks.[26-28] Additionally, due to their vast diversity in multiple fields of research, nanoparticles have now been incorporated into common everyday products such as food preservatives, cosmetics, clothes, etc.[28] This constant unseen contact with nanoparticles has promoted the field of nanotoxicology in order to study the greater impact these ENMs have on both biological and environmental systems (Figure 2.1).[29] However, due to limitations in analytical instrumentation and analytical test methods directly applicable to measure ENMs in the environmental and biological matrices, nanotoxicity remains an underdeveloped field as it struggles to keep up with the advancing research and development of nanoparticles and nanoparticle-based materials actively being developed.[30,31]

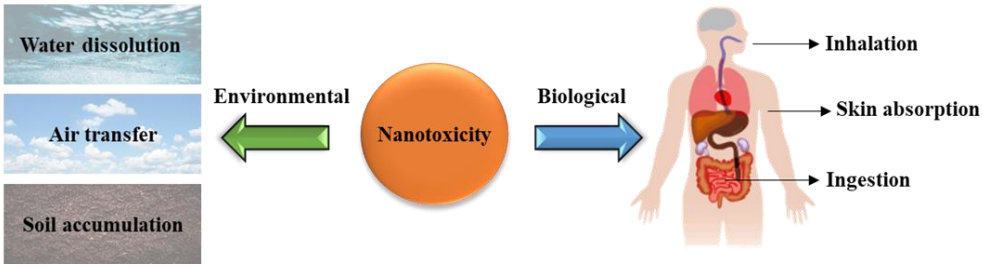

Figure 2.1: Nanotoxicity exposures for environmental and biological matrices.

One differentiating characteristic is the size of the nanoparticles, which can make them chemically different from larger particles and bulk materials (e.g., diffusivity across cell membranes).[26,28-32] Additional unique biological cell interaction comes in the form of ENMs surface charge, with anionic and neutral ENMs generally having a lower toxicity than cationic materials. ENMs surface charge may also have an additional influence on the particles' overall shape and the shape of ENMs can alter cell membranes as well, thus heavily influencing the cellular uptake mechanism.[29,32,33] Surface coatings of ENMs can alter their toxicity by providing additional electrostatic forces, molecular adhesion, and atomic layer deposition which have contributed to cell death.[33] Furthermore, the elemental composition of ENMs contributes to their overall toxicity to both biological and environmental systems.[34] Such elements can range from transition metals (gold, silver, copper, iron, etc.) to non-metals (silica, carbon) and can greatly alter the previously listed properties of size, morphology, coating, physical, and chemical properties.

NPs and ENMs are primarily introduced into the environment through consumer products.[35] This problem has many arising concerns due to detection of low concentrations, usually ng/L, and the current limits of detection of analytical instruments[36]. NPs can be integrated into the human body by a multitude of ways, but most commonly through inhalation, ingestion, and skin absorption, while environmental exposure is usually through the air, water, and soil integration.[28] For biological matrices, ENMs can impact the mitochondrial function of cells in addition to producing reactive oxidative species (ROS). The analytical measurement of mitochondrial function, damage, and ROS levels in biological systems remains a primary tool in the assessment of toxicity.[37] Cell metabolism is greatly impacted by ROS levels as they are natural byproducts in cell metabolism and contribute to cell survival, death, signaling, inflammation, and differentiation.[37] An imbalance of ROS leads to disrupted redox homeostasis in cells, which

ultimately interferes with the cell's overall function in relation to DNA/RNA breakage, membrane destruction, protein carbonylation, and other means.[38] However, ROS compounds have been considered previously as an alternative to chemotherapy for cancer treatment.[39] Radical compounds such as superoxide ($O_2^{\bullet-}$), hydroxyl ($HO^{\bullet}$), hydroperoxyl ($HO_2^{\bullet}$), peroxyl ($RO_2^{\bullet}$), alkoxyl ($RO^{\bullet}$), carbon dioxide ($CO_2^{\bullet-}$), carbonate ($CO_3^{\bullet-}$) and singlet oxygen ($^1O_2$) are involved in key cell reactions that revolve around signaling and homeostasis processes.[37-39] However, high levels of ROS compounds can result in oxidative damage to healthy cells and interfere with cell metabolism with accumulation of ROS contributing to normal cells turning into cancer cells.[40,41] NPs introduction into biological systems can interfere with ROS generation in several ways depending on the characteristics of the NPs.[37]

With the field of nanoscience and nanotoxicity expanding, the purpose of this chapter is to investigate what analytical techniques are used in toxicology assessments to effectively measure ENMs and NPs toxicity. Furthermore, this chapter will also include advancing analytical techniques to better detect and evaluate ENMs and NPs in biological and environmental matrices and what future methods could be introduced to better detect ENMs toxicity. There is no current federal or state legislation in the United States specifically for the regulation and testing of nanomaterials. Regulatorily, there are agencies such as the intergovernmental Organization for Economic Co-operation and Development (OECD), the American Industrial Hygiene Association (AIHA), and the US Environmental Protection Agency (USEPA) that investigate ENMs and NPs and their greater impact on human health and the environment as well as regulate analytical methods of testing ENMs. Given the increasing amount of ENMs integrating into consumer and industrial products, the OECD has identified a greater need than ever to have accurate testing methods since the potential risks and impacts of nanomaterials is not well developed. To date, the

OECD has documented over 780 studies on specific physiochemical properties of nanomaterials that contribute to plant/animal toxicity as well as ecotoxicity.[42] Additionally, with the evolving field of ENMs, the OECD has continued to modify current methods and promote new ones as a means of keeping up with the advancing technology around ENMs.[42]

2.2. Current methods and concerns for *in vitro* nanotoxicity determination

Due to the variety of factors that impact ENMs and NPs toxicity, as previously mentioned, there is no single method for accurate detection of ENMs and NPs toxicity. Rather, there are several methods that are commonly used in combination to help identify the characteristics of ENMs and NPs and their overall toxicity.[43] Dynamic light scattering (DLS) is most commonly used to determine particle hydrodynamic size and zeta potential (also determined by the DLS instrument) determines particle surface charge, while methods such as scanning electron microscopy (SEM) and transmission electron microscopy (TEM) allow for the visual detection of ENMs and NPs that can then be measured for their size distribution. Although these methods give insight on the characteristics of the ENMs and NPs, they do not give toxicity analyses. For this, researchers turn to *in vitro* and *in vivo* examinations.

To examine *in vitro* toxicity first, one standard technique to measure ENMs and NPs toxicity in *in vitro* studies is by MTT (3-[4,5-dimethylthiazole-2-yl]-2,5-diphenyltetrazolium bromide) assays, which assess the cells' mitochondrial function by detecting mitochondrial dehydrogenase through an enzymatic reduction. Another standard measurement technique for toxicity determination is by examining ROS formation within the cells, which indicates oxidative stress and interference in cell function. In order to measure intracellular ROS, a fluorescent ROS indicator is typically utilized. This indicator, when in the presence of ROS, will chemically change

and thus yield a different fluorescent signal. This signal can be observed through fluorescence spectroscopy[44,45] or through confocal microscopy[46]. The most common *in vitro* assays are summarized in Table 2.1.[47]

Table 2.1: *In vitro* assay types used for the analysis of nanotoxicity.

Assay Type	Cell Toxicity Investigation
Proliferation	Cell metabolism
Apoptosis	DNA, protein, and lipid damage
Necrosis	Membrane Integrity
Oxidative Stress	DNA/RNA damage, lipid peroxidation, protein oxidation/nitration, ROS generation, antioxidant counterbalance

However, these two methods are not completely accurate means of determining toxicity. For example, an interesting study was performed by Dönmez Güngüneş et al. where three different kinds of the NPs (Fe_3O_4, fullerenes (C_{60}), and single walled carbon nanotubes (SWCNT)) were tested in two different cell lines (human periodontal ligament fibroblasts (hPDLF) and mouse dermal fibroblast (mDF)).[48] Although the MTT assay and ROS analyses of the three different kinds of NPs showed that the hPDLF cells, compared to the mDF cells, were more susceptible to all three NPs (showing higher ROS levels and larger MTT decrease in cell viability), Dönmez Güngüneş et al. utilized a relatively newer analytical method known as xCELLigence where a gold microelectrode is labeled with an antigen to which the test cells are exposed. The current between the gold and reference electrode will increase as the cells neutralize the antigen blocking the signal on the gold surface which allows for a real-time kinetic measurement of cell health and behavior. Dönmez Güngüneş et al. found that although the human cells were more susceptible to the NPs in terms of raw cell viability in the MTT assays and mitochondrial failure due to ROS formation, the

internal mechanism of the cells remained unchanged with all three types of NPs tested. The mouse cells, however, showed internal failure as most of the cells no longer performed as they should, an indication of some toxic effects within the cells. Without this third analysis in xCELLigence, one could have concluded that the mouse cells were relatively unaffected by the NPs solely based on the MTT and ROS analyses without knowing the true impact on the intercellular mechanisms that were impacted to a larger degree compared to the human cells.

2.3. Current methods and concerns for *in vivo* nanotoxicity determination

Furthermore, there are concerns around unintended particle accumulation in organs, and thus induced toxicity, for *in vivo* studies, where the potentially hazardous NPs are directly or indirectly introduced into living organisms with measurements of toxicology endpoints. Several nanoparticles, such as gold-based and other metal-based NPs, have shown to display toxic effects and organ accumulation, however, the toxicity pathways are not fully understood.[49,50] The most common organs tested for, and impacted by, NPs accumulation are the liver, heart, kidney, spleen, lungs, intestine, and stomach with the liver and organs with high blood flow being the most unintended accumulation sites.[51,52] Which organs are impacted more depends on the elemental composition and size of the NPs.[53] For instance, carbon-based NPs show the most unintended accumulation in the liver[54], however, smaller carbon-based particles less than 20 nm, such as quantum dots (QDs), showed increased accumulation in the brain parenchyma[55]. The QDs can pass through the BBB pathway and through the trigeminal nerve or olfactory epithelium, which can cause additional problems when investigating *in vivo* toxicity.[56,57] However, despite the accumulation of carbon-based particles in organs, due to their chemical makeup, carbon-based

NPs typically display little to no significant increase in toxicity when examining *in vivo*[58], however, some toxic effects have been recorded[59].

Silica-based NPs show similar low toxicity when accumulated in organs compared to carbon-based NPs; although some uterine metabolic issues have been discovered in mice.[60] Silica NPs appear to accumulate the most in the liver, lungs, and spleen[61], with some kidney accumulation[62] also being observed. Histological studies of silica-based NPs showed no ill effects in organs when the NPs are cleared from the organs within a few months.[63,64] For NPs composed of less harmful chemicals such as carbon and silica, their size plays a much greater role in their toxicity in addition to their chemical composition. Generally, smaller particles are more toxic due to their size allowing them to better interact with cellular components such as proteins, fatty acids, and nucleic acids.[65] However, larger silica NPs have also been shown to possess greater toxicity than smaller silica NPs.[64] Polymer- and metal-based NPs with low clearance rates generally showed the greatest toxicity and organ accumulation,[66,67] sometimes containing greater metabolic disturbance[68].

However, there remain several limitations to *in vivo* analysis of NPs organ accumulation and long-term toxicity. For some studies, a lack of macrophage uptake and blood circulation suggests the need for better assays.[69] Additionally, *in vivo* studies with animas do not necessarily carry over to human studies as many nanoparticles never reach their intended site and are cleared from the bloodstream quickly[70], adding to the difficulty of detecting *in vivo* toxicity and attributing it to NPs. Furthermore, most *in vivo* studies examine toxicity on week- or month-long analyses. Year-long analyses are rarely examined in research primarily due to time constraints despite being informative and essential.[71] Nonetheless, these are all considerable parameters when examining *in vivo* nanotoxicity, with several current methods needing improved testing parameters and animal

models for more accurate assessments of toxicity, especially when examining the complexity of human health.[72] The most commonly used *in vivo* analysis methods are listed in Table 2.2.[47]

Table 2.2: *In vivo* methods for nanotoxicity determination.

Methods	Toxicity Analysis Examination Types
Radiolabeling	Radioisotope tracking of NPs through biological systems examined for biodistribution
Clearance	Excretion and metabolism of NPs examined after various exposure times
Serum Chemistry	Enzymes, lipids, hormones, and proteins in serum examined for metabolic interferences
Histopathology	Cells, tissues, and organs examined for disease manifestation
Hematology	Red and white blood cells, platelets, and coagulation system examined for disorders

To specifically measure nanotoxicity *in vivo*, several factors are taken into consideration. Immune system response compounds such as globulin, TNF-alpha, and KC-GRO are typically analyzed in order to determine toxicity. However, correlation is not necessarily causation, as simply analyzing these markers after the introduction of ENMs is not an accurate means of analyzing toxicity. A far more exact means of determining ENMs toxicity *in vivo* is by utilizing ICP-MS and microwave digestion; where tissue and organic samples are prepared via microwave digestion before being subjected to ICP-MS. This is a more accurate way of confirming ENMs integration and concentration within key organs, as shown in a study by Weaver et al.[73]. This is because there needs to be a way to confirm that the amount of ENMs or NPs injected into the animal remained in the organs and did not pass through the bloodstream without interacting. Unfortunately, the use of ICP-MS is limited to metal-based NPs and cannot be used for NPs that are, for example, polymer-based. For these NPs, it is much more difficult to accurately determine their concentration and integration *in vivo*. Therefore, methods previously mentioned (such as

fluorescence, bioluminescence, microscopy, and spectroscopy) are utilized as accurately as possible.[74,75] Additionally, smaller sized NPs concentrations tend to be more difficult to determine[76]; with the importance of concentration control for *in vitro* and *in vivo*, it is vital to accurately determine in biological target tissue the concentration for nanotoxicity tests.[77] However, despite the extensive means to confirm ENMs integration and concentration, *in vitro* and *in vivo* toxicity tests have been known to be highly inconsistent and sometimes do not agree with each other[78,79], possibly due to variation between cell culture lines and animal species[80] and issues with testing method accuracy[81]. The OECD has made several adjustments to their nanotoxicity testing protocols to combat this variation problem; however, to this day, no single method has proven to be the golden standard for testing nanotoxicity in ENMs, and methods continue to be tested and enhanced/modified to keep up with the accelerating ENMs development field.[82]

For example, the OECD has implemented newly revised inhalation toxicity testing guidelines, 412 and 413, for 28-day and 90-day inhalation toxicity studies, respectively, for carbon based ENMs. These methods focus on inhalation since it is a primary route of ENMs exposure to humans[83], with employees of carbon-based ENMs manufacturing being the largest group at risk of physical contact and, due to an increase in the number of applicational fields, there is a growing concern about overall hazardous potential when it comes to inhalation.[84] However, according to a study performed by Kim et al., there is a significant lack of data for the toxicity regarding multi-walled carbon nanotubes (MWCNTs).[85,86] Nonetheless, following the OECD guideline[87], Kim et al. investigated the 28-day inhalation toxicity study by exposing rats to MWCNTs at 0, 0.257, 1.439, and 4.253 mg/m^3 for 28 days.[85] They generated their MWCNTs aerosols by using an acoustic dry aerosol generator and made sure to test the aerosol chamber concentrations using OC/EC and field emission-transmission electron microscope (FE-TEM) to confirm MWCNTs

exposure. Cytotoxicity markers such as lactate dehydrogenase (LDH), micro-albumin (mALB), and micro-total protein (mTP) were examined in bronchoalveolar lavage fluid (BALF) for toxicity analysis as proposed by the OECD method. Samples of the rat lungs were taken after 1-day, 7-day, and 28-day post exposure (PEO-1, PEO-7, and PEO-28). They noticed that the alveolar macrophages of the lungs contained MWCNTs material in all the samples. Low concentration (0.257 mg/m^3) did not show any pneumocyte damage or cell inflammation. Agglomerated MWCNTs, however, were seen throughout the lungs including the bronchi, alveolar ducts, and alveoli.[84] Additionally, the moderate and high concentration samples (1.439 and 4.253 mg/m^3) showed granulomatous lesions filled with MWCNTs in all PEO sampling days. It is of note that Kim et al. did not find any significant organ weight changes after exposure for all time periods, demonstrating that solely relying on organ weight as an indication of toxicity is inadequate, which was also pointed out in the study by Weaver et al. However, toxicity results varied drastically between similar studies and studies that used different types of MWCNTs.[85,88,89] Although the new OECD method significantly improved their previous 412 method, the lack of data available on MWCNTs proved to still be a major setback with general testing methods.

2.4. New and enhanced methods of nanotoxicity determination and particle detection

Although the above methods help detect the toxicity of ENMs and NP, there remains an issue with the accuracy of the methods.[81,90] Part of the reason is due to the lack of technology applied to analytical methods. With the ever-advancing field of nanomaterials, analytical methods lag behind or suffer due to lack of data, as shown previously with the OECD 412 method. Additionally, if there are no measures taken to confirm the successful integration of the ENMs or NPs into the cells/organisms being tested for toxicity, then there cannot be an accurate follow-up evaluation/conclusion that the concentration of ENMs/NPs injected caused toxicity. Furthermore,

research articles do not necessarily expand beyond their target application when it comes to the ENM degradation and integration into other matrices and systems, particularly their environmental exposure/fate[91], leading to many published articles in the nanotoxicity field to be limited and questionable[92]. In fact, most published ENMs test methods for environmental or biological testing applications have not been validated following the procedures set by the USEPA or other regulatory bodies.[81] Although the regulatory guidance for the testing of chemicals set by the USEPA, OECD, and AIHA provide extensive guidelines that help protect both humans and the environment, there remains limited guidance for analytical test methods or toxicity assessment procedures for direct measurements of ENMs, rather than indirect measurements.[89] This exemplifies the need to further advance analytical instrumentation and test methods in order to better directly evaluate ENMs both qualitatively and quantitatively, especially in complex biological matrices and environmental matrices (e.g., air, sludge, and water).[93] In many cases with environmental and biological testing, there is a lack of sufficient standards to compare with real-time measurement analyses.[94,95] Ultimately, analytical methods need to be improved or new methods developed in order to counter the detection and accuracy problems seen in nanotoxicity assessments.[96]

Such advancements in both analytical instrumentation and test methods can be seen across several recently published articles. The first being by Mader et al., who applied the USEPA analytical test method validation guidance in the development of a new test method for the quantitation of engineered NPs in water matrices.[90] The validated ENMs analytical test method for water is not limited to metal containing NPs and was applied to two OECD ecotoxicity test methods for both *Daphnia* and algae; by direct measurement of nanoparticle size distribution and concentration in the ecotoxicity test matrix. Analytical NP measurement was performed on a

Liquid Nanoparticle Sizer[97], Differential Mobility Analyzer[98], and Nano Water-Based Condensation Particle Counter[99]. The role of the Liquid Nanoparticle Sizer was crucial as it quantitatively diluted sample solutions using ultrapure water by a 20:1 to 20,000:1 ratio prior to nebulization. The nebulizer was adjusted to produce an aqueous aerosol with a droplet size of 300 nm with the sample dilution ensuring that statistically only one particle was present in each droplet. The resulting nebulized aerosol was then dried, classified and counted. This combination of the two instruments allowed for the measurement of the number of each size of particles in a volume of air. Additionally, by scanning a range of particle mobility in the differential mobility analyzer the number-weighted NP size distribution could be determined. The validated Mader et al. method quantified both the NP size distribution and dose level verification concentrations in the *Daphnia* and algae ecotoxicity test matrices. The most important factor in accurate quantitative measurements for the method was the application of matrix-matched NP standard calibration curves to minimize analytical response factor difference between standards and test matrices.[60] The analytical method requires the use of certified NP reference materials for calibration standard preparations and, because of the availability of other certified metal and nonmetal NP materials, it is possible to adapt their EPS guidance validated test method for other ENMs and in other water matrices (e.g., drinking water, wastewater, groundwater).[90]

Additionally, Savić-Zdraković et al.[100] also utilized an OECD testing guideline, in this case guideline 218,[101] for the examination of CeO_2 NP uptake in relation to oxidative stress parameters, *in vivo* genotoxic effects, larvae, and life-trait toxicity parameters, using ICP-MS analysis. Through this study, the importance of establishing a standardized methodology for larvae lethality and sub-lethality cutoffs was established as their results indicated that the larvae were not at risk of CeO_2 NP toxicity; however, accumulation of these particles could impact organisms that

consume the larvae. Therefore, much like the Kim et al. study, the value of the OECD guideline is greatly impacted by the lack of data surrounding CeO_2 NP toxicity testing which also contributes to these NPs being listed on the OECD priority list of environmental impact assessment.[100]

Another method that advanced the analytical side of NP detection was by Hadioui et al. who discussed detecting NPs in the environment by inductively coupled plasma mass spectrometry (ICP-MS), due to it being one of the best analytical techniques for detecting ENMs.[102,103] In addition to ICP-MS being limited to metal-based NPs, it is also limited by particle size detection limits, with many NPs and their oxides being out of detection range. Hadioui et al. helped to improve this detection limit by adjusting the kind of aerosols introduced into the ICP-MS. They examined different nebulization desolvating techniques; distinguished as "dry" and "wet" aerosols. Hadioui et al. noted an increased number of counts in the dry mode, and for smaller particles (9 nm Ag) more ions were extracted using the desolvator for both wet and dry aerosols. Both desolvating systems lead to an increased signal intensity of the 9 nm Ag and 25 nm TiO_2 NPs. Thus, dry aerosols had a better detection and resolved peak intensities for small NPs.[102] Additionally, an increase in sensitivity was also noted for the 5 nm Ag NPs. Injecting 2.3 ng/L, the dry aerosol compared to the wet aerosol showed a drastic increase in the particles that were detected; and no particles were detected when using the ICP-Q-MS (the quadrupole ICP-MS used to evaluate instrument sensitivity).[101] The size detection limit for ICP-Q-MS was 17 nm while single particle sector field ICP-MS (ICP-SF-MS) was 5 nm, which could further be reduced to 3 nm using the desolvating nebulizer. Thus, by using dry aerosols for ICP-MS, Hadioui et al. successfully improved sensitivity and enhanced ion extraction.[102]

Cui et al., in their study, helped examine the fate and improved detection of TiO_2 NPs in the environment using ICP-MS by changing synthesis parameters, utilizing Ho as a chemical

marker in their NPs and thus designing $NaHoF_4@TiO_2$ NPs. By using an $Al(OH)_3$ layer around Ho in $NaHoF_4$, the added colloidal stability and hydrophilic surface helped TiO_2 deposition and coating when synthesizing the NPs.[104] The goal of the Cui et al. study was to be able to detect engineered TiO_2 NPs in the environment without Ti background interference. Using their unique synthesis, the addition of Ho as a tracer significantly helped detect the engineering TiO_2 NPs in the environment, despite being in low concentrations (100 million-fold dilutions or 5000-200,000 particles/mL).[104]

As for biological fates of nanoparticles, studies such as Turco et al.[105] and López-Serrano Oliver et al.[106] provide valuable insights into biological nanotoxicity testing. Turco et al. utilized a sputtering-enabled intracellular X-ray photoelectron spectroscopy (SEI-XPS) method in which metallic NPs were cultured in media and cells before being directly measured for their internalization, stability, and oxidation state. Utilizing this technique, Turco et al. provided a possible method to help assess NP integration, accumulation, and longevity and thus provide valuable insight into nanotoxicity. López-Serrano Oliver et al. also investigated metal-based nanoparticles, in the form of silver, and focused on developing a new method of mass cytometry that can quantify NP numbers per single cell.[106] Although they were able to make some interesting and important discoveries for new nanotoxicity analyses of NPs, there remains an issue with NP monitoring and intracellular uptake of NPs out of the mass range of mass cytometers.

Lastly, a fairly recent method to determine nanotoxicity is through *in silico* analyses. These methods have proven advantageous as they bypass the costs of extensive *in vitro* and *in vivo* experiments and removed the need for animal experiments.[107] These *in silico* studies helped provide insight into potential alternative testing methods for nanotoxicity as existing experimental data surrounding the tested NPs and ENMs confirmed the results of the computational data

obtained.[108,109] However, the main issue with *in silico* analyses is similar to the *in vitro* and *in vivo* experiments, which is the inconsistency and lack of data. *In silico* methods are dependent on existing nanotoxicity data to confirm the model's accuracy.[110] Therefore, the accuracy of future *in silico* analysis is also dependent on advancing current analytical methods to better analyze nanotoxicity experimentally.

Through all of these studies it is seen that analytical methods and the increased availability of certified analytical NP standards are vital in the measurement of ENMs and NPs in toxicity assessments, as these materials need to be accurately identified and quantified in both biological and environmental matrices.[111] Although progress has been made in developing toxicity assessments and testing methods, the accuracy of these methods have been called into question on more than one occasion.[112] Agencies like OECD and AIHA help provide guidelines for nanotoxicity testing, however, a repeated problem across studies is the lack of data and certified analytical standards surrounding the NPs and ENMs, particularly the newer ones that are being produced at a rate that is not matched by development of the analytical instrumentation, even with enhanced methods and new analytical techniques[113]. There is also the problem with long-term ENMs and NPs exposure/integration, with toxic degradation particles potentially never being assessed as NPs and ENMs production continues. Generational and long-term biological and environmental impacts of ENMs and NPs nanotoxicity is an underdeveloped field, but one that should be considered for exploration.[114]

2.5. Summary and Conclusions

When it comes to the world of nanoscience, its vast diversity in engineered materials makes this area of research rich in possibility but ultimately leads to uncertainty in the health of humans

and the environment they come into contact with. Truly, there is an abundance of nanotoxicity data among research articles, but small groups of ENMs and NPs tend to be studied and their long-term environmental fate or chemical/physical changes over time are not analyzed.[115] Even with several agencies and organizations across multiple countries pooling their information together on the topic of nanotoxicity safety policies[116] the problem still remains. As the field of nanoscience advances, analytical instrumentation and methods struggle to find applicability when it comes to accurately measuring ENMs' and NPs' harmful effects and possible integration into alternate media. Although traditional biological testing such as *in vitro* and *in vivo* help glimpse the impact NPs might have on chosen cells and living organisms, the methods tend to be indirect measurements of ENMs, by analyzing organ weight, mitochondrial function, and ROS levels. Indirect methods tend to only analyze the cell's or organism's response to the ENMs without confirming the exact amounts of ENMs that were involved in the negative or positive response to the ENMs. As a result, there has been a movement to develop direct methods of measuring ENMs in the environment and in biological systems as it remains a challenge to multiple national and international agencies to accurately assess the toxicity of ENMs. As new nanoparticles and nanomaterials are synthesized, many existing protocols and methods for their detection have been amended by researchers outside of the agencies that designed them, still with no single method being suitable for all ENMs. A significant limitation with the development of nanomaterials is that traditional regulatory and scientific methods used to assess the biological and environmental toxicity of chemicals do not generally apply to the assessment of nanomaterials. This limitation is directly related to the need for advancements and further developments of analytical instrumentation, analytical test methods, and analytical standards for the direct measurement of ENMs and NPs in biological and environmental matrices.

There is no doubt that NPs and ENMs pose potential risks environmentally and biologically.[117] Without addressing the issues of accurate and consistent nanotoxicity determination, unknown degradation products, accumulation, and induced toxicity are of increasing concern. Given that ENMs and NPs are continually being advanced and incorporated into commercial products and medical treatments, the potential risk of undetected toxicity in the short- or long-term is also increasing. Particularly for the use of NPs in medicine, it is of utmost importance that treatment NPs are precisely characterized, detected and traceable, that their degradation products are not harmful, and that short- and long-term toxicity is not induced in the treated patient, especially for human trials. Similarly, the environmental fate of NPs and ENMs needs to be heavily considered as they can accumulate in the soil, water, plates, and animals. If not properly detected, quantified, and removed as contaminants, NPs and ENMs, both whole or degraded, can pose increasing environmental risk and potentially cause irreversible harm to the ecosystem. With 9806 products[118] currently having incorporated nanomaterials, it is vital to address the problem of detection limits and improve analytical testing methods.

CHAPTER III

SYNTHESIS OF HIGHLY NEAR-INFRARED FLUORESCENT GRAPHENE QUANTUM DOTS (GQDS) USING BIOMASS-DERIVED MATERIALS FOR IN VITRO CELL IMAGING AND METAL ION DETECTION

3.1. Introduction

A wide range of fluorescent nanomaterials have been implemented into vast areas of research since the development of nanotechnology. These nanomaterials include quantum dots, metal nanoparticles, rare-earth metal doped nanoparticles, inorganic dye-doped silica nanoparticles, polymer-encapsulated organic nanoparticles, and carbon nanomaterials.[117-122] Previously, semiconducting quantum dots (QDs) were ideal fluorescent probes, but due to the fact that most of these QDs are composed of heavy metals such as cadmium, which can cause both biological and environmental hazards in large enough quantities, alternative materials such has graphene and carbon have been considered.[123,123] The derivative material of graphene has several important properties from mechanical to thermal with recent developments that have shown an increase in research interest for graphene quantum dots (GQDs). The most favorable characteristics include low toxicity, chemical inertness, stability, and biocompatibility compared to traditional QDs.[123-136] GQDs also present fluorescence properties, which allows GQDs to be used in the detection of both inorganic and organic materials such as metal ions, organic polymer molecules, and anions.[133] In particular, fluorescence itself has been a vital tool for the development of imaging techniques to visualize key details in living cells and animals without involving potentially harmful radioactivity or electron burning.[128]

The combination of these factors has made GQDs a considerable candidate in applications that involve bioimaging and metal sensing, among other applications.[129,131] Additionally GQDs

have potential advancements for *in vivo* and *in vitro* fluorescence imaging due to functionalized GQDs having the capability of interacting with biological systems.[127,137-139] However, the field of GQDs is still relatively new with a need of more extensive research in order to broaden the use for *in vitro* and *in vivo* bioimaging techniques, especially when the GQDs can detect key biomarkers.[126,140,141] Furthermore, GQDs with near infrared (NIR) fluorescence are extremely rare and scarcely reported despite being highly desirable for biomedical imaging applications.[142] Although there have been recent reports of NIR containing GQDs[143] and carbon dots[144], there remain several undesirable traits during synthesis procedures such as the use of strong acids[145], element doping[146,147], lengthy reactions[148], and forms of graphene oxide[149]. Additionally, may synthesized GQDs with NIR fluorescence usually contain their peak in the lower NIR region[142,150,151] (650-810 nm) or are dependent on larger GQD particle size[152]. NIR fluorescent materials for bioimaging are sought after due to their deep tissue penetration, weak emission light scattering, and lower background, which helps improve signal-to-noise ratios.[142,153,154] Having a carbon-based nanomaterial that emits fluorescence in the NIR region would provide not only the above listed imaging benefits but also reduced toxicity and easier cellular uptake and integration because of their chemical make-up and small particle size.

GQDs have two primary means of synthesis; top-down or bottom-up.[126,140,141,155,156] The top-down method breaks down carbon source material by several different methods to synthesize GQDs; including lithography, oxidation, microfluidization, electrochemical, solvothermal, and microwave-assisted hydrothermal.[139,156] The bottom-up method combines smaller groups of benzene derivatives and carbonization from organic polymers to form larger quantities of GQDs using stepwise solution chemistry, oxidation, hydrothermal heating, and pyrolysis.[126,139,156] The top-down method tends to be more extensive than the bottom-up approach, although the latter is

more precise yet complicated with many synthesis steps.[157] Typically, molecules containing polycyclic aromatic rings are used as reliable precursors to form high-quality GQDs via the bottom-up approach.[156-159] These precursors are traditionally produced from non-renewable sources such as coal and petroleum coke. The rapidly increasing world population and irreversible consumption of limited fossil resources have been motivating researchers to develop new materials using sustainable sources. Several reports have recently suggested that renewable, inexpensive, and readily available biomass waste, such as rice husk,[160] dead leaves[161], waste peels[162], or food waste[163], have the potential to emerge as an alternative feedstock to produce GQDs. Meanwhile, efforts have been made to utilize biomass-derived chemicals as precursors, including citric acid[164] and L-glutamic acid.[165] However, there are still few examples of high-quality GQDs derived from biomass when compared to the non-renewable petrochemicals.[166] Therefore, developing reliable biomass-derived precursors for creating high-quality GQDs instead of petrochemical-based precursors for suitable applications remains highly desirable.

Furfural, one of the most valued biobased chemicals, is derived from an array of agro-residues such as wheat bran, corncobs, sugar cane bagasse, and sawdust.[167,168] Furfural has been serving as a vital starting material to produce a wide range of specialty chemicals and renewable building blocks for designing new materials.[169,170] One such furfural derived building block is *cis*-3,4-di(furan-2-yl)cyclobutane-1,2-dicarboxylic acid (CBDA-2).[171] This furfural derived building block has shown potential applications in developing 100% bio-based cyclobutane-containing polymers (CBPs) exhibiting desirable chemical and thermal properties, which are potentially important in industry. In this work, GQDs were synthesized by the bottom-up process using biomass-derived diacid CBDA-2 in a NH_4OH/water solution. The obtained GQDs were analyzed for fluorescence characteristics and chemically characterized by various analytical methods for *in*

vitro imaging and metal ion detection applications. These analytical techniques include UV-Vis absorption spectroscopy, fluorescence spectroscopy, dynamic light scattering (DLS) for size distribution and zeta potential analysis, Fourier transform infrared spectroscopy, high resolution transmission electron spectroscopy (HRTEM), X-ray photoelectron spectroscopy (XPS), and confocal microscopy. Lastly, the GQDs were subjected to several concentrations of multiple metal ions to determine their capability of detecting these ions.

3.2. Experimental

3.2.1. Materials

2-[4-(2-hydroxyethyl)piperazin-1-yl]ethanesulfonic acid (HEPES buffer, 99.5%), 3-(cyclhexylamino)-1-propanesulfonic acid (CAPS buffer, ≥99%), 2-(cyclohexylamino)ethanesulfonic acid (CHES buffer, ≥99%), maleic acid (≥99%), citric acid (≥99.5%), $FeCl_3$, $Pb(Ac)_2 \cdot 3H_2O$, and $CuSO_4$ were purchased from Sigma-Aldrich (St. Louis, MO, USA). Ammonium hydroxide (99%) and fluorescein dye were both purchased from Fisher Scientific (Hampton, NH, USA). $HgCl_2$ was purchased from ACROS Organics (Fair Lawn, NJ, USA) and $FeSO_4 \cdot 7H_2O$ was purchased from Sargent-Welch VWR Scientific (Buffalo Grove, IL, USA). Dulbecco's Modified Eagle Medium was purchased from Life Technologies/Thermo Fisher Scientific (Waltham, MA, USA). Fetal bovine serum was purchased from Peak Serum (Wellington, CO, USA). Penicillin-strep was purchased from Sigma Aldrich/Millipore (St. Louis, MO).8-well Chambered Coverglass with non-removable wells and TO-PRO®-3 Stain were purchased from Thermo Fisher(Waltham, MA,USA). Fluoromount-G® mounting medium was purchased from SouthernBiotech (Birmingham, AL). CytoTox 96® Non-Radioactive Cytotoxicity Assay kit was purchased from Promega (Madison, WI, USA).

3.2.2. Sample solution preparation

The 20 mM HEPES buffer solutions of pH 1.0, 3.0, 5.0, 7.0, 9.0, and 11.0 were prepared with the pH being adjusted by the addition of NaOH and HCl. For investigating photostability, all the samples were sonicated for 30 min before analysis. For the detection of metal ions, 100, 10, and 1.0 µM solutions of $CuSO_4$, $FeCl_3$, $FeSO_4$, $Pb(Ac)_2$, and $HgCl_2$ were prepared in water. Based on the GQDs response to mercury ions, an optimization experiment was designed to test four changing factors of pH, temperature, concentration of Hg^{2+} and concentration of GQDs. These four parameters were used to design a 2^4 screening factorial design in order to identify important factors impacting fluorescence intensity and to better analyze optimal analysis conditions.

3.2.3. Instrumentation for the characterization of GQDs

A Perkin Elmer Lambda 1050 UV-250 UV/Vis/NIR spectrophotometer was used for the UV/Vis absorption measurements of the GQDs. The fluorescence spectra and photostability measurements were acquired by a Shimadzu RF-6000 spectrophotometer. NIR fluorescence was measured by a Jobin-Yvon-Horiba Fluorometer 3 Model (FL 3-11 spectrofluorometer). A Marlwen model of Nano-ZS Zetasizer was used to measure the zeta potential and size distribution of GQDs in HEPES buffer with different pH values. A JEOL Jem 2100 Electron Microscope was used to obtain high resolution transmission electron microscopy (HRTEM) images of the GQDs. A Thermo Fisher Scientific Nicolet iS5 Fourier transform infrared spectrometer (FT-IR) was utilized to obtain the IR spectra of CBDA-2 and the GQDs. X-ray diffraction (XRD) measurements were analyzed on a Rigaku SmartLab and X-ray photoelectron spectroscopy (XPS) analysis was conducted on a Perkin Elmer model PHI 40-700. An Olympus FV3000 Laser Scanning Confocal Microscope was used for the *in vitro* cell imaging of the GQDs. Two channels were used for the imaging; those being red (Fura-Red (Ca-free)) and green (Alexa 488). MCF-7 cells were cultured

over night with 100 µL of 0.8 mg/mL GQDs and TOPRO-3 labeled nuclei. Bright-field images were also collected at the same time for clarification of cell growth and location on the coverslips. A ELX800 plate reader was used for the cell viability experiments. GQDs with gradient concentrations were incubated overnight and the cell viability assay was followed using the protocol of CytoTox 96® Non-Radioactive Cytotoxicity Assay kit.

3.2.4. Synthesis of GQDs

CBDA-2 was synthesized from furfural in two steps.[162] In the first step, a key intermediate - *trans*-3-(2-furyl)acrylic acid was constructed by Knoevenagel condensation between furfural and malonic acid and the subsequent decarboxylation. In the second step, 2.0 g crystalline *trans*-3-(2-furyl)acrylic acid was ground into a fine powder and suspended in 100 mL of hexane in an Erlenmeyer flask equipped with magnetic stirring. The continuously stirred suspension was subjected to UV radiation of eight 13-watts residential blacklight (Feit Electric BPESL15T/BLB compact fluorescent twist bulb) for 12 h. After completion of reaction, the slurry was filtered to give CBDA-2 as a white solid (1.9 g, 95%).

To prepare GQDs, CBDA-2 was dissolved in DI-water with a final concentration of 4.0 mg/mL before the pH was brought to 10.0 using NH_4OH. The solution was then autoclaved for 12 h at 200 ˚C. Furthermore, a Spectra/Por Dialysis Membrane BioTech CE Tubing of MWCO 100-500 Da was used for the dialysis of the GQDs for 12 h before being centrifuged for 30 min. The final concentration of the GQDs was calculated to be 2.0 mg/mL, which was stored in a fridge for future usage.

3.2.5. Quantum yield measurement

The quantum yield was calculated for the visible GQDs peak (440 nm) using Equation 3-1 below with quinine sulfate in 0.1 M H_2SO_4 as the standard reference.[172] Quinine sulfate in 0.1

M H_2SO_4 was previously determined to have a Φ_{st} of 0.54 with η_{st}^2 being equal to 1 in the case of 0.1 M H_2SO_4.[172] Similarly, the GQDs would also have η_x^2 equal to 1 when prepared in a pH 7.0 HEPES buffer. The quantum yield was calculated to be 45%.

$$\Phi_x = \Phi_{st}\left(\frac{Grad_x}{Grad_{st}}\right)\left(\frac{\eta_x^2}{\eta_{st}^2}\right) \qquad (3-1)$$

3.3. Results and Discussions

3.3.1. Design of the synthesis of GQDs using biomass

The goal of this work was to develop a simple yet effect method for the synthesis of fluorescent graphene quantum dots that could be used in bioimaging applications as well as metal ion detection. Traditional bottom-up methods for GQDs synthesis utilize organic precursors, such as amino acids, citric acid, histidine, L-glutamic acid, and glucose.[156] Inspired by those starting materials and the low-cost properties of biomass materials, we developed a method for synthesizing GQDs using a biomass derived molecule from furfural, CBDA-2. CBDA-2 was obtained from biomass that was also non-toxic. After dissolving CBDA-2 in NH_4OH/water and heating at 200 ˚C for 12 h, the fluorescent GQDs were synthesized. Under the irradiation of UV light, the prepared GQDs showed bright blue fluorescence (Scheme 3.1).

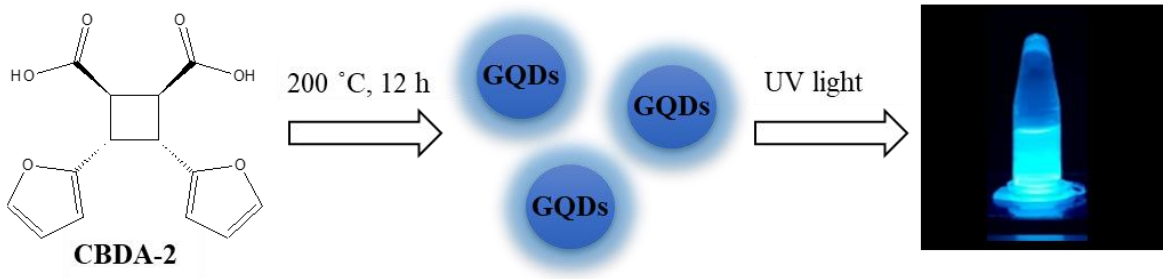

Schematic 3.1: CBDA-2 conversion to GQDs by pyrolysis under basic conditions. Exposure to UV light shows that the newly synthesized material contains fluorescent properties.

3.3.2. Characterization of the synthesized GQDs

To characterize the newly synthesized GQDs, a number of experiments were conducted. First, the morphology and size of the GQDs were characterized. To clearly observe the crystal structure of the GQDs, a high-resolution transmission electron microscope (HRTEM) was employed. The results are shown in Figure 3.1. Both larger clusters (Figure 1A) and enlarged single particle GQDs (Figure 1B) were observed.

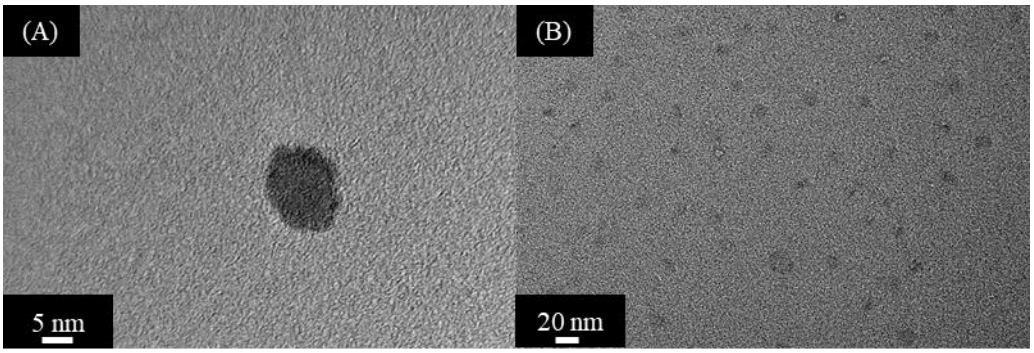

Figure 3.1: HRTEM images of the GQDs, 2.0 mg/mL. (A) individual particle that are ~ 4-7 nm in diameter; (B) image of particle dispersion that show no agglomeration.

The size distribution of the GQDs was statistically measured using DLS (Figure 3.2). To better observe the individual particles, the GQDs were sonicated for 30 min prior to analysis. The resulting table shows that the GQDs range from approximately 3-10 nm with an average size of 6.5 $\pm$ 3.5 nm. This is conclusive with the HRTEM images, which show individual particles around 4-7 nm, with a decent dispersion of the particles.

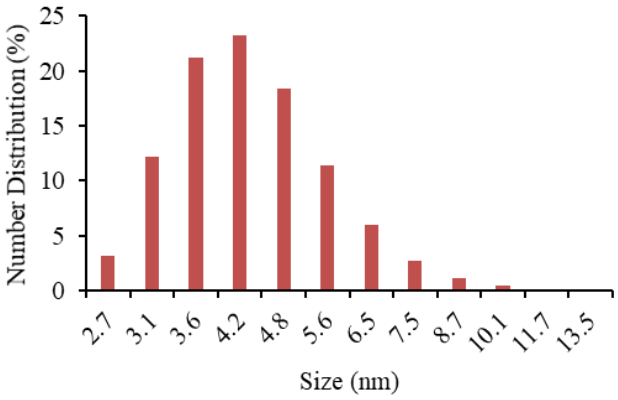

Figure 3.2: Size distribution of sonicated GQDs in water by DLS, 20 µg/mL. Individual GQDs are approximately 3-10 nm.

The zeta potential of the GQDs in different pHs was also analyzed (Figure 3.3). The results showed that in the range of pH 7.0-11.0, GQDs had high zeta potentials of -35.6, -26.2, and -22.5 mV, respectively. Comparatively, pH 5.0 showed a moderate decrease of zeta potential at -9.7 mV. The remaining solutions of pH 3.0 and 1.0 showed the lowest zeta potentials of approximately -2.2 and +7.3 mV, and therefore contain the highest agglomerates. Based on these results, the GQDs were more stable in basic pH solutions of 7.0-11.0 and stable moderately at pH 5.0.

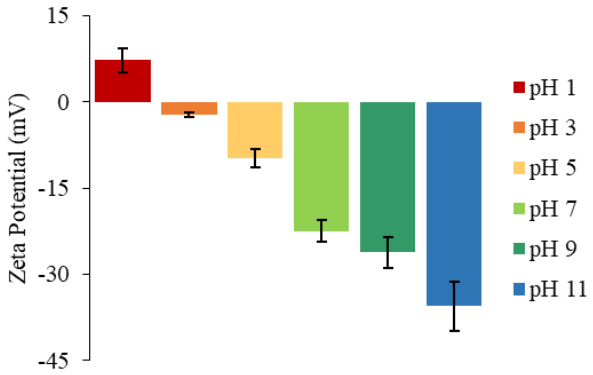

Figure 3.3: Zeta potential measurements of the GQDs in the maelate (pH 1.0), citrate (pH 3.0 and 5.0), HEPES (pH 7.0), CHES (pH 9.0) and CAPS (pH 11.0) buffers. All GQD solutions were in concentrations of 0.2 mg/mL.

Furthermore, the functional groups of the GQDs were investigated using FT-IR spectra (Figure 3.4). First, the starting material of CBDA-2 was measured (Figure 3.4, red). The spectrum of CBDA-2 showed two clear peaks at 3103 and 1697 cm^{-1} that are attributed to -OH and C=O functional groups, respectively.[173,174] The GQDs contained four characteristic peaks of -OH at 3207 cm^{-1}, sp^3C-H at 2923 cm^{-1}, C=O at 1684 cm^{-1}, and C=C at 1559 cm^{-1} (Figure 3.4, blue).[175-179] In comparison, CBDA-2 shared some similar functionality in the forms of the alcohol and carbonyl groups. However, the GQDs show additional peaks of the olefin type and additional sp^3 hybridized C-H bonds. This strongly indicating a reaction that charged the chemical structure of the GQDs from CBDA-2, with the additionally π-bonds in the GQDs contributing to their fluorescent properties.

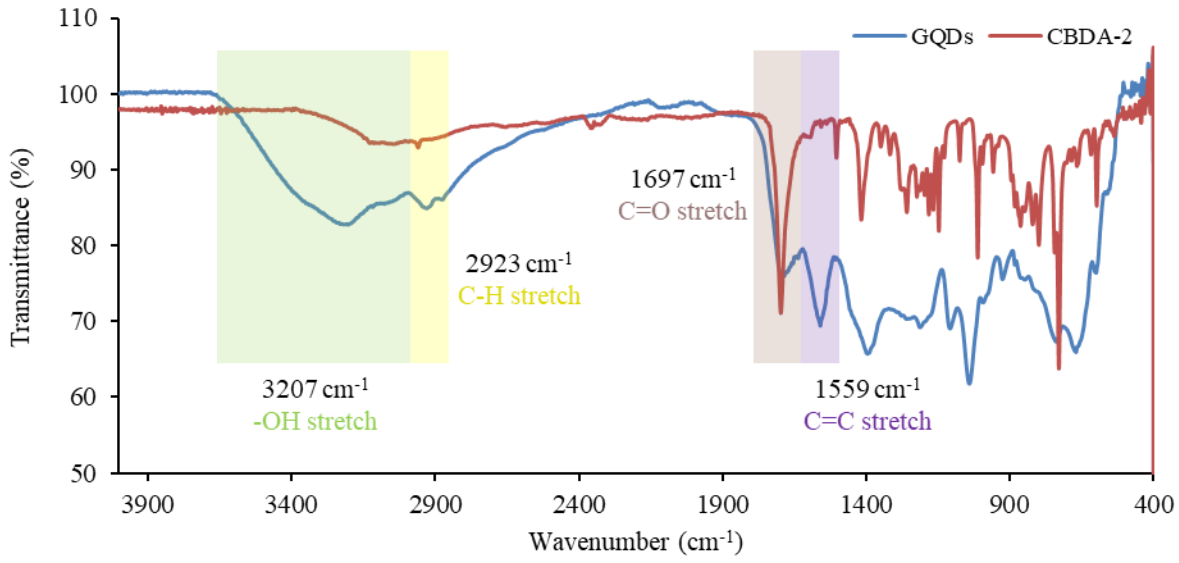

Figure 3.4: FT-IR spectra of CBDA-2 (red) and the GQDs (blue). The two compounds share similar peaks in the alcohol and carbonyl regions but differs with the GQDs having additional olefin and sp^3 C-H peaks.

The composition of the GQDs was further analyzed using XRD and XPS techniques. As shown in Figure 3.5, the XPS analysis results suggested that the prepared GQDs are composed

mainly of carbon and oxygen with two main peaks: oxygen (531 eV) and carbon (284 eV) (Figure 3.5A), which is in agreement with the literature.[180] Also, two smaller peaks were seen in the range of 1020-970 eV, which is consistent with carbon as graphite.[180] Additionally, it is of note that the oxygen peak has a left-field shift; typical oxygen peaks have a range of 528-534 eV while this oxygen peak has a range of approximately 529-538 eV. This is also consistent in the mica (blank) spectrum; thus, it was deduced that the functionality ranges within the oxygen peak were also shifted to the left. The carbon peak was not shifted for either the mica or the GQDs, and remains in the functionality ranges of the peak. Therefore, the shifted oxygen peak could have been a calibration issue with the instrument. High-resolution XPS of C 1s demonstrated three peaks at 286.7, 285.67, and 288.11 eV, which were attributed to C-O-C, C-C, and C=O, respectively (Figure 3.5B). The O 1s spectrum showed two major peaks at 531.14 and 533.05 eV for C=O and C-O, respectively (Figure 3.5C).

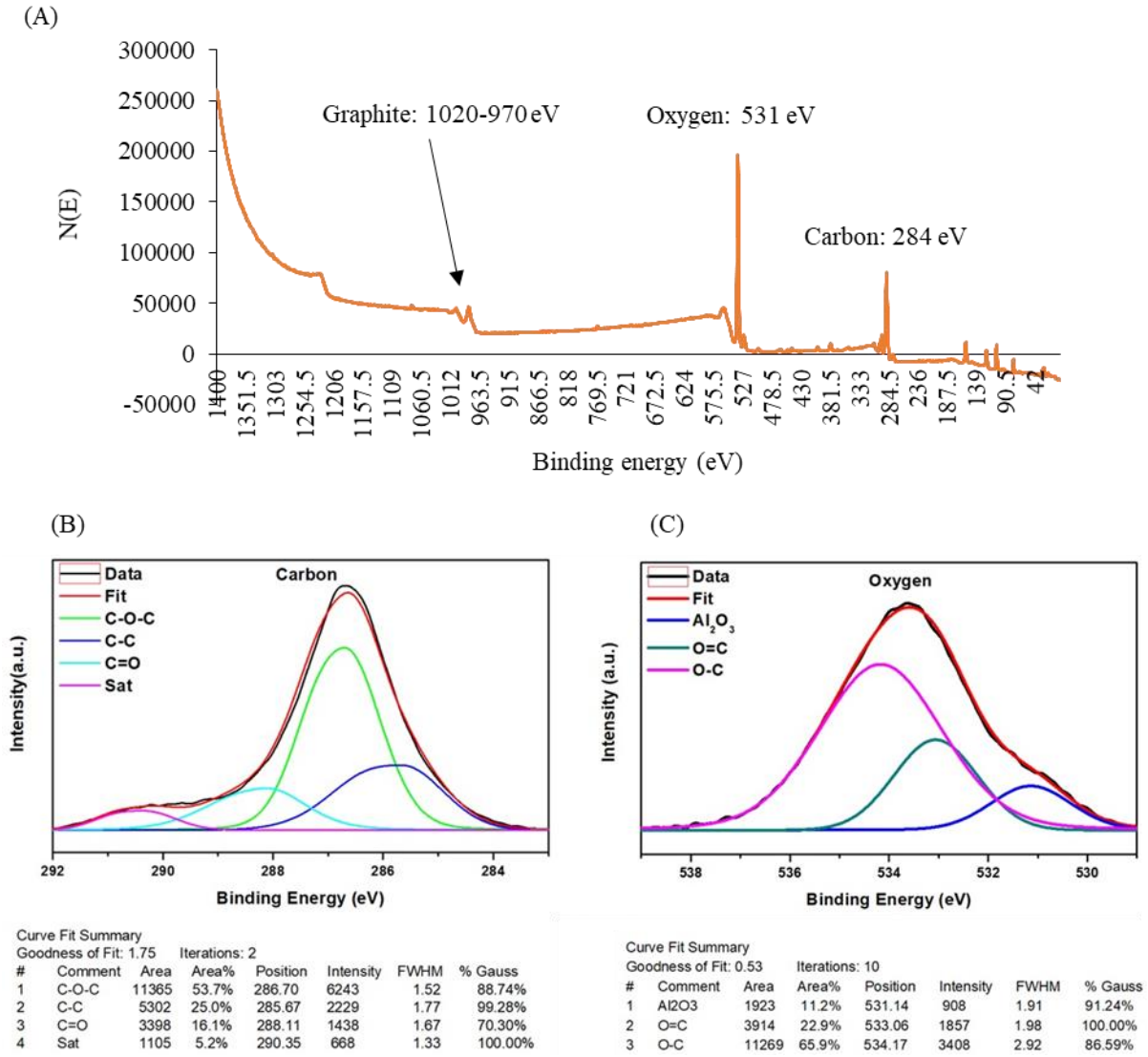

Figure 3.5: (A) Entire XPS spectrum of the GQDs shows the left-field shift of the oxygen peak at around 531 eV and the carbon peak at 284 eV. Graphite peaks are visible in the 1020-970 eV range. XPS graphs of the carbon (B) and oxygen (C) peaks of the GQDs (2 mg/mL). The carbon peak shows clear distribution of the functional groups within. The oxygen peak has regions of unknown groups, most likely due to the peak shift of the instrument.

Additionally, the XRD pattern (Figure 3.6) of the GQDs showed a broad peak centered at 20° (d spacing = 0.44 nm) that could be attributed to the π-π stacking of GQDs. Neither a characteristic (002) peak of graphene oxide at around 10° nor a sharp 0020 peak of graphene at

26.5° were observed, which implies the two-dimensional nature of the GQDs which lack a long distance order (i.e. a small thickness) along (002) direction (*c*-axis). These results were strongly consistent with the results of previous reports.[181-183]

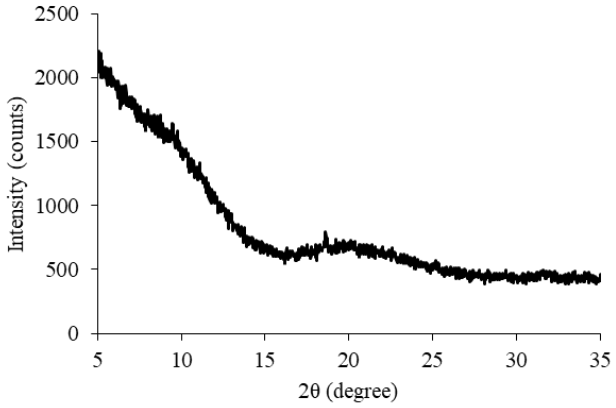

Figure 3.6: XRD analysis of the GQDs shows a distinctive peak at 20°, an indication of graphene within the sample.

3.3.3. Optical properties of the GQDs

The most important designed feature of the GQDs is their fluorescence properties. This property was investigated using both spectroscopy and microscopy. The UV-Vis absorption and fluorescence emission spectra of the GQDs were recorded in a 0.2 mg/mL aqueous solution. As shown in Figure 3.7A, the GQDs showed two UV-Vis adsorption peaks at about 230 and 300 nm, which were attributed to $\pi - \pi^*$ transition of the C-C bond and the n- π^* transition of the oxygen-containing groups. When the GQDs were excited with 310 nm radiation, the GQDs emitted a strong fluorescence peak at 440 nm (Figure 3.7B).

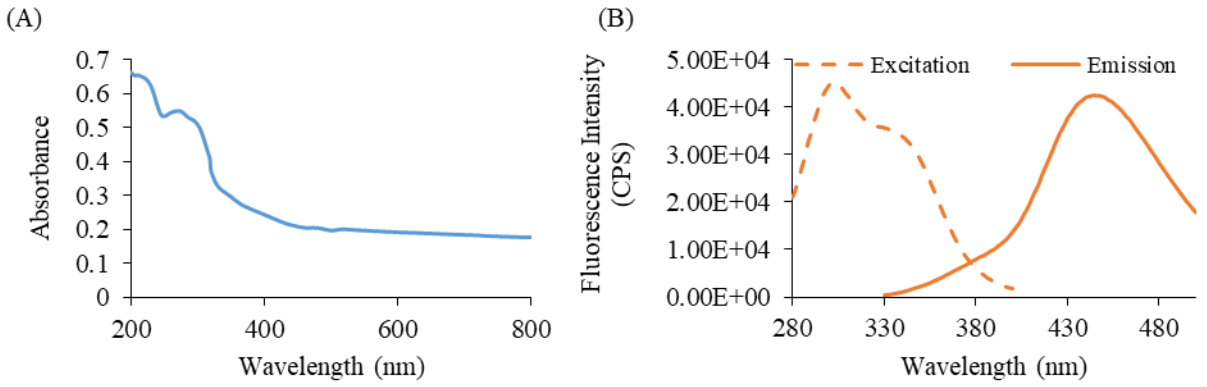

Figure 3.7: (A) GQDs absorption profile in water at concentration of 0.1 mg/mL. Clear absorption can be observed at ~ 300 nm. (B) Fluorescence profile of the GQDs (0.2 mg/mL in water) that showed the 310 nm excitation and 440 nm emission peaks.

Then, the 3D fluorescence map was collected by changing the excitation wavelength from 280 to 500 nm for both the GQDs in pH 7.0 and the pH 7.0 blank. This observation was witnessed again in the 2D fluorescence spectra (Figure 3.8A) which showed two fluorescence peaks in the GQDs, centering at 440 and 850 nm. In order to prove that the fluorescence was coming from the GQDs and not from the precursor, solvent, or second order excitation, spectra of CBDA-2, DI-water, and 20 mM HEPES pH 7.0 buffer were also collected. The GQDs showed the strong fluorescence emission at 440 and 850 nm, indicating that the prepared GQDs could be used as a strong fluorescent tag in the visible and NIR range. To further confirm that the NIR peak was indeed coming from the GQDs, several concentrations of the material were prepared and analyzed. Figure 3.8B shows that the fluorescence intensity of the GQDs in the NIR region was proportional to concentration (25 - 3.125 µg/mL). Similar with the other reported GQDs, the prepared GQDs showed excitation-dependent fluorescence emission. As shown in Figure 3.8C, the visible emission peak of the GQDs shifted from 440 nm to 520 nm when the excitation wavelength was changed from 280 nm to 500 nm. The highest fluorescence emission was obtained when the

excitation wavelength was 300 nm, with an emission peak at 440 nm. Comparatively, the NIR emission peak (Figure 3.8D) also showed an excitation light dependency, shifting from 850 to 900 nm. The highest fluorescence emission peak was recorded at a 340 nm excitation light.

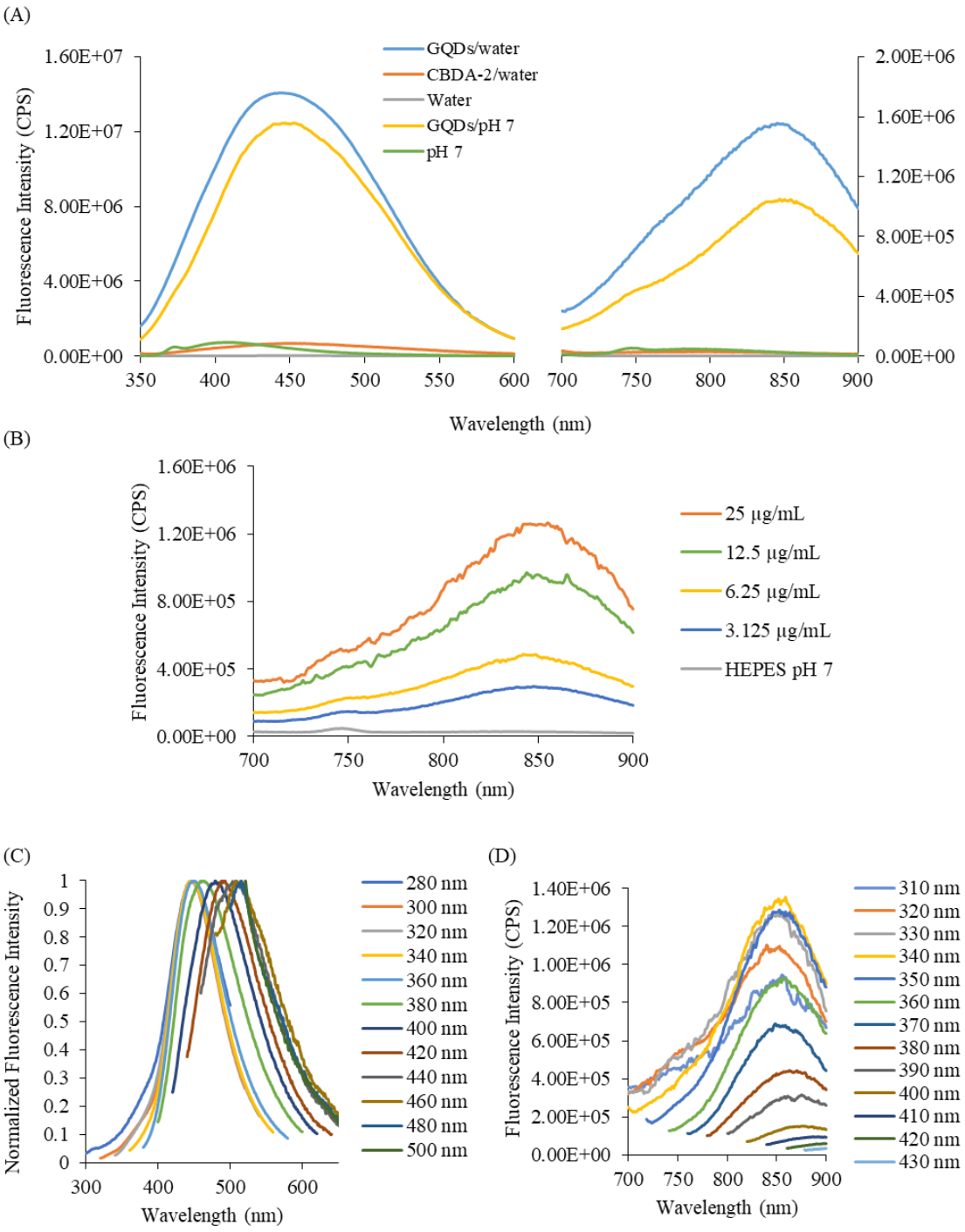

Figure 3.8: (A) Emission profile of the GQDs under 310 nm excitation light that yields two peaks. CBDA-2, pH 7.0, and water (solvent) were tested for interference effects. CBDA-2 and pH 7.0 showed slight emission at 440 nm but no peak was observed at 850 nm. (B) Changing concentration of GQDs NIR peak, indicating fluorescence is being emitted from the material. (C) Excitation light dependent behavior for the visible peak at 440 nm emission. (D) Excitation light dependent behavior for the NIR peak at 850 nm emission.

To be utilized as a fluorescent tag in bioanalysis and bioimaging, the stability of the GQDs is critical. Therefore, the fluorescence intensity of the GQDs were studied in different pH conditions from 1.0 to 11.0 using the HEPES buffer. The results depicted that the GQDs contained the highest fluorescence intensity in the range of pH 5.0-9.0 (Figure 3.9), which is ideal for biological samples. Under pH 5.0 or higher than pH 9.0, the fluorescence intensity of the GQDs decreased. Especially, the GQDs were unstable in pH 1.0 (maleate) where the largest quenching was observed, which might be caused by the fact that the zeta potential of the GQDs at pH 1.0 became almost zero, resulting in the aggregation-induced quenching of the GQDs.

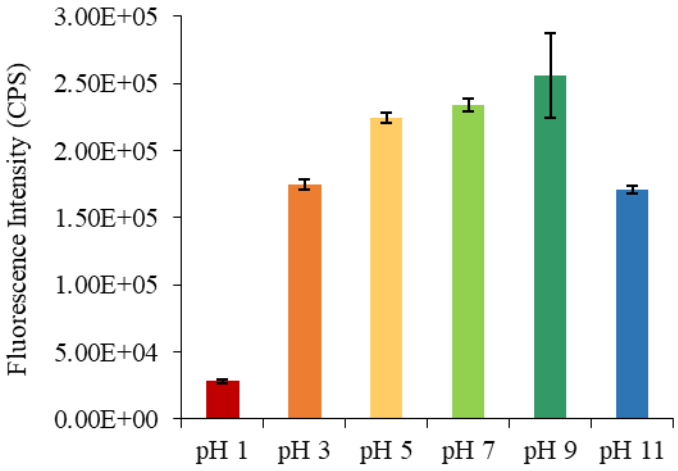

Figure 3.9: Fluorescence intensity measurements of the GQDs shows quenching effects in maelate pH 1.0 while pHs 3.0 – 11.0 (citrate, HEPES, CHES, and CAPS) depict relatively no significant difference in decrease or increase of intensity. All solutions were 0.2 mg/mL GQDs.

The photostability of the GQDs was analyzed with a sample of FITC being used as the standard comparison dye. The resulting data can be found in Figure 3.10 below. Both FITC (20 µM) and the GQDs (80 µg) were cultured in MCF-7 cells. Cells were incubated with GQDs for 3 h before being fixed. After 30 min of imaging, the GQDs bleached to only 60% of their original intensity while FITC bleached to 20% in the first 300-400 seconds. This experiment provided

helpful insight into the GQDs photostability and potential to be used for prolonged analyses in other applications that require it.

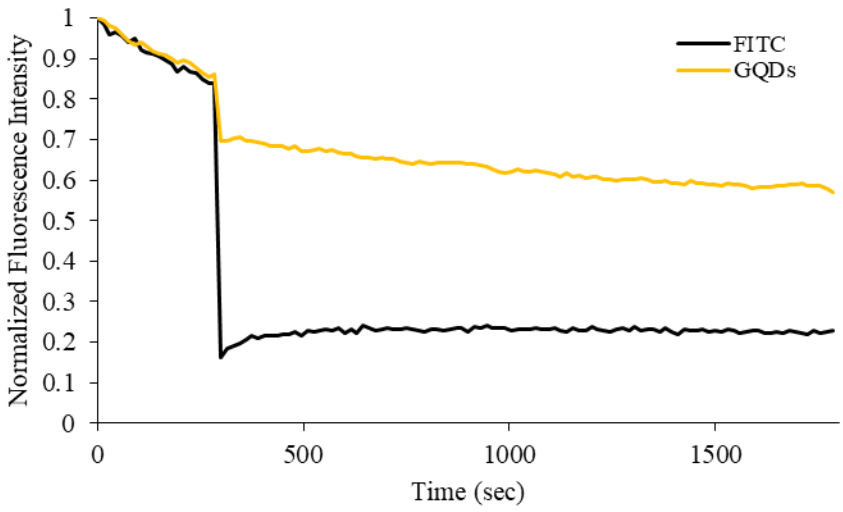

Figure 3.10: Photostability of the GQDs compared to FITC dye.

3.3.4. In vitro cell imaging with MCF-7 cells doped with GQDs

Based on the promising fluorescence properties, we tested the feasibility of the GQDs to be used as a fluorescent agent for cell labeling. Before the imaging application, the cytotoxicity of the GQDS was evaluated by MTT assay in RAW 264.7 cells due to the pinocytosis property. The results showed that negligible toxicity was observed even when the concentration of the GQDs was as high as 200 µg/mL (Figure 3.11), indicating the superior biocompatibility of GQDs obtained from the biomass. However, GQDs have been reported to show toxic effects and a decrease in cell viability at 500 µg/mL exposures.[184,185]

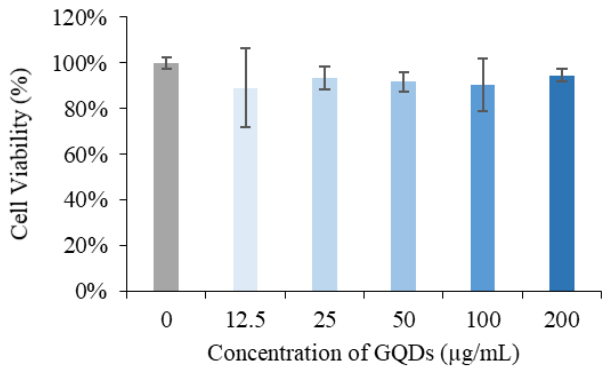

Figure 3.11: Cultured RAW cells with various concentrations of GQDs. The highest cell death occurs at 12.5 µg/mL, while no culture exceeded 20% total cell death compared to the control.

MCF-7 cells were used for the GQDs confocal imaging because of the epithelial-like morphology and the formed monolayer. GQDs were incubated with the MCF-7 cells for 3 hours, the cells were fixed and imaged using a fluorescence confocal microscope. As shown in Figure 3.12, the MCF-7 cells incubated with the GQDs showed strong green fluorescence (Alex 488 channel) upon excitation at 405 nm, indicating that the GQDs entered the cells through endocytosis.[186,187] In contrast, no apparent fluorescence was observed in the green channel when the MCF-7 cells were incubated with TO-PRO-3 labeled nuclei (Figure 3.12A). The fluorescence intensity of the cells were quantified using ImageJ software, and the results demonstrated that that of the fluorescence intensity of the MCF-7 cells incubated with the GQDs was three-fold higher than the pure cells, indicating that GQDs could be used as strong fluorescent tags to label both cell membranes and the cytoplasm. Incubating the GQDs with MCF-7 cells resulted in the GQDs entering the cells through endocytosis and imaged using confocal microscopy. The two colored channels and the bright-field images are depicted below (Figure 3.12B). It is clearly observed that when the GQDs were added, the intensity across the channels also increased, mostly in the green channel but a slight increase was also observed for the red channel.

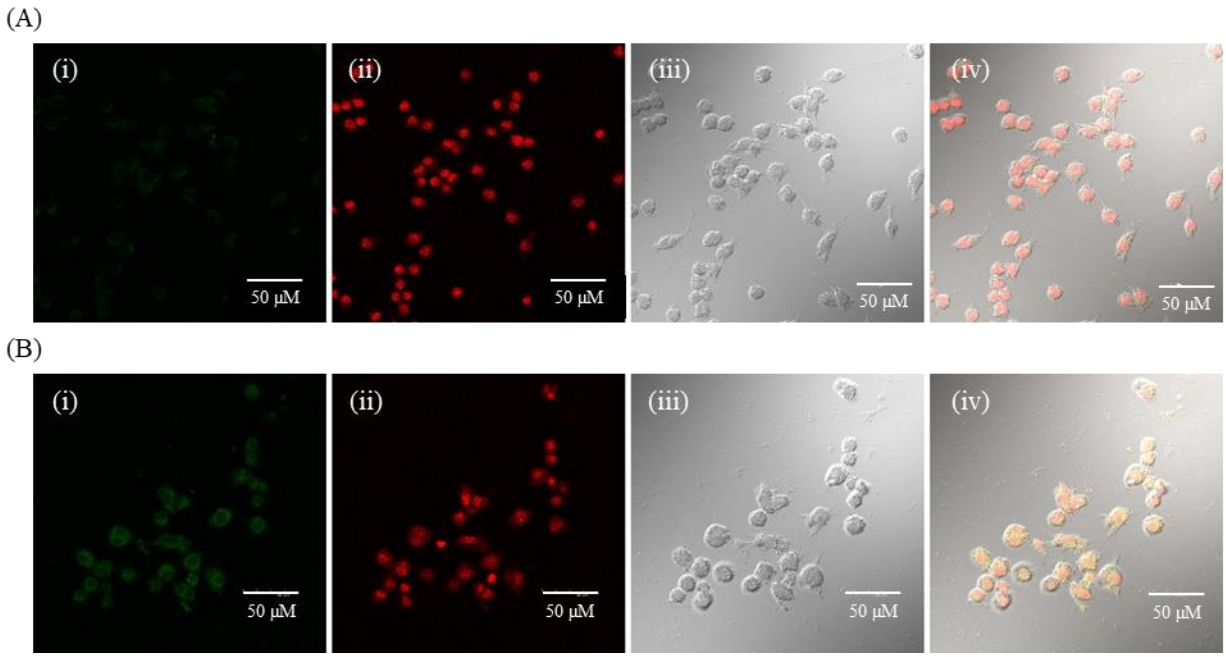

Figure 3.12: *In vitro* images of MCF-7 cells cultured with GQDs: (A) TOPRO-3 labeled nuclei of MCF-7 cells; (B) 100 µL of 0.8 mg/mL GQDs and MCF-7 cells. Columns are two excitation channels used as well as the microscope images: (i) Alexa 488, (ii) Fura-Red (Ca-free), (iii) Bright-field and (iv) Overlaid.

3.3.5. Metal ion detection using the GQDs

The fluorescence bioimaging is the main application of the developed GQDs. Additionally, the GQDs were found to be capable of metal ion detection. Thus, five common metal ions in solution: Cu^{2+}, Fe^{3+}, Fe^{2+}, Hg^{2+}, and Pb^{2+} were tested using the GQDs (Figure 3.13). As a result, Hg^{2+} showed the greatest quenching at the highest concentration of 100 µM. Pb^{2+} showed little to no quenching across the concentrations and the remaining ions of Cu^{2+}, Fe^{3+}, and Fe^{2+} showed quenching at the highest concentration (100 µM) but no significant decrease in fluorescence was observed for the 10 and 1.0 µM solutions. Therefore, the detection of Hg^{2+} was further studied using the GQDs by optimization of experimental conditions temperature and pH.

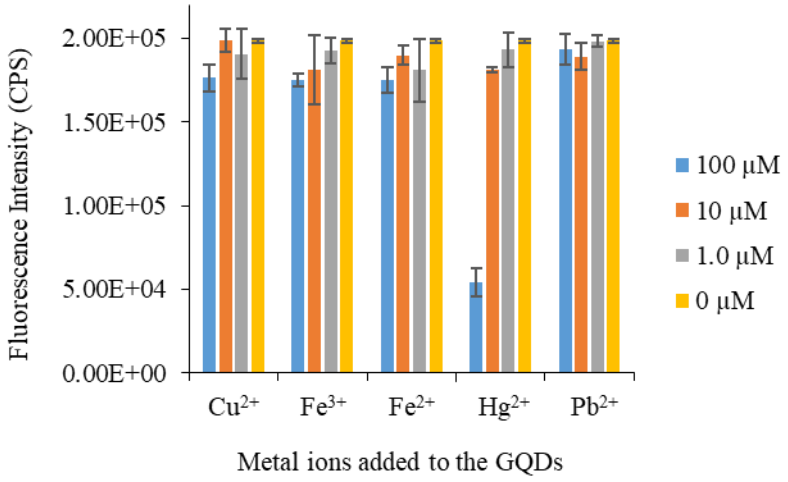

Figure 3.13: Metal ion detection using 0.1 mg/mL GQDs in HEPES buffer pH 7.0: Cu^{2+}, Pb^{2+}, Fe^{2+}, Fe^{3+}, and Hg^{2+} were added in 100, 10, and 1 µM final concentrations.

For optimization, 2^4 factorial screening was first used to identify estimated parameters for optimal conditions, those being pH, temperature, concentration of Hg^{2+}, and concentration of GQDs. The high and low conditions can be found in Table 3.1 as well as the center point conditions. After screening, a regression model was fitted to the data to estimate the relationships between the dependent variables. A normality test of the residuals helped to verify the model's accuracy, yielding a p-value greater than the α-value of 0.05, which indicates that the residuals are normally distributed. Due to this, the model interference can be confirmed as validated and thus an optimization analysis on the data was performed as well.

Table 3.1: 2^4 factorial screening DOE method applied to the optimization analysis of the GQDs, Hg^{2+}, temperature, and pH conditions.

Factor	Low (-1)	High (+1)	Center Point (CtPt)
pH	3.0	9.0	6.0
Temperature	2 °C	50 °C	26 °C
Concentration of Hg^{2+}	1.0 µM	100 µM	50.5 µM
Concentration of GQDs	0.02 mg/mL	0.50 mg/mL	0.26 mg/mL

After analyzing the results, the Pareto chart of all factors and interactions (Figure 3.14A) shows that out of the four factors, only concentration of Hg^{2+} and concentration of GQDs were significant. Temperature had no effect as a main factor, nor did its interaction have any impact on the overall fluorescence intensity. Additionally, pH as a main factor had no direct effect, however, its interaction with both the mercury ion and GQD concentrations were significant. Therefore, all insignificant factors and interactions were removed from the terms and the Pareto chart was plotted again (Figure 3.14B).

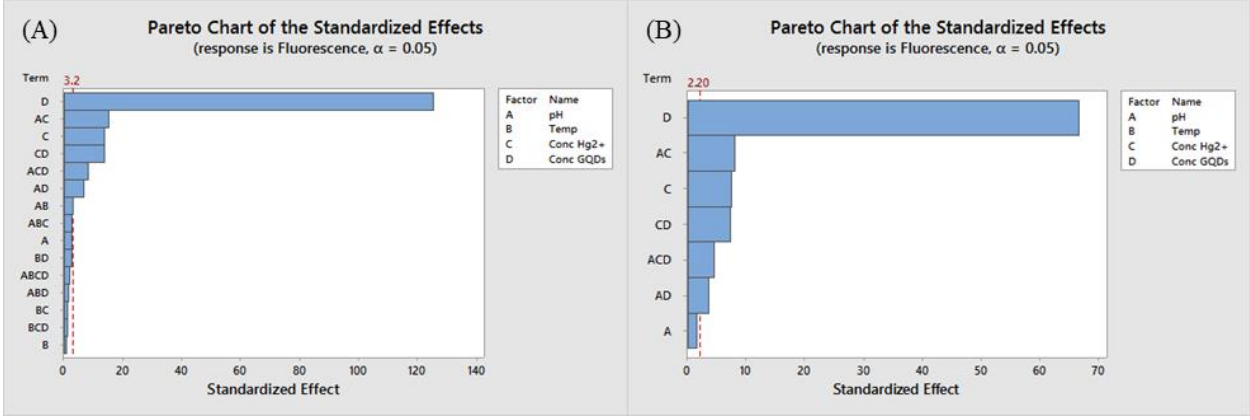

Figure 3.14: (A) Pareto chart of the full factorial analysis of fluorescence intensity with all interactions included. (B) Pareto chart of refined terms of the full factorial analysis after removing temperature as well as other insignificant interactions.

As previously stated, the optimization analysis was also conducted to help verify the 2^4 design above. To confirm this, the model was set to predict the conditions that would yield the highest fluorescence intensity. The model predicted that pH 9.0, 0.50 mg/mL GQDs, and 1.0 µM Hg^{2+} were the most optimal conditions for the highest intensity. For convenience, the triplicate runs of the optimal conditions were conducted at room temperature (26 °C) given that the model predicted temperature to be an insignificant factor. Figure 3.15 depicts all sixteen factorial samples and the four center points in comparison to the optimal condition samples in gray. The triplicate runs confirmed the DOE experiment by having an equal average fluorescence intensity as sample 10 (pH 9.0, 2 °C, 1.0 µM Hg^{2+}, 0.50 mg/mL GQDs), which had the highest fluorescence out of the twenty screening samples and sample 12 (pH 9.0, 50 °C, 1.0 µM Hg^{2+}, 0.50 mg/mL GQDs) was second. Additionally, the optimization predictor showed that for higher concentrations of Hg^{2+}, a more acidic environment yielded a higher fluorescence intensity and for lower concentrations, basic conditions had higher fluorescence intensities. Furthermore, decreasing the concentration of the GQDs decreased the quenching sensitivity, as the 0.02 mg/mL samples yielded nearly the same intensity for the 100 and 1.0 µM Hg^{2+} additives, regardless of temperature and pH. However, increasing the concentration of GQDs to 0.5 mg/mL also did not drastically increase the sensitivity, with similar complications arose from the 1.0 µM detection, as observed in Figure 3.13 with 0.2 mg/mL of GQDs.

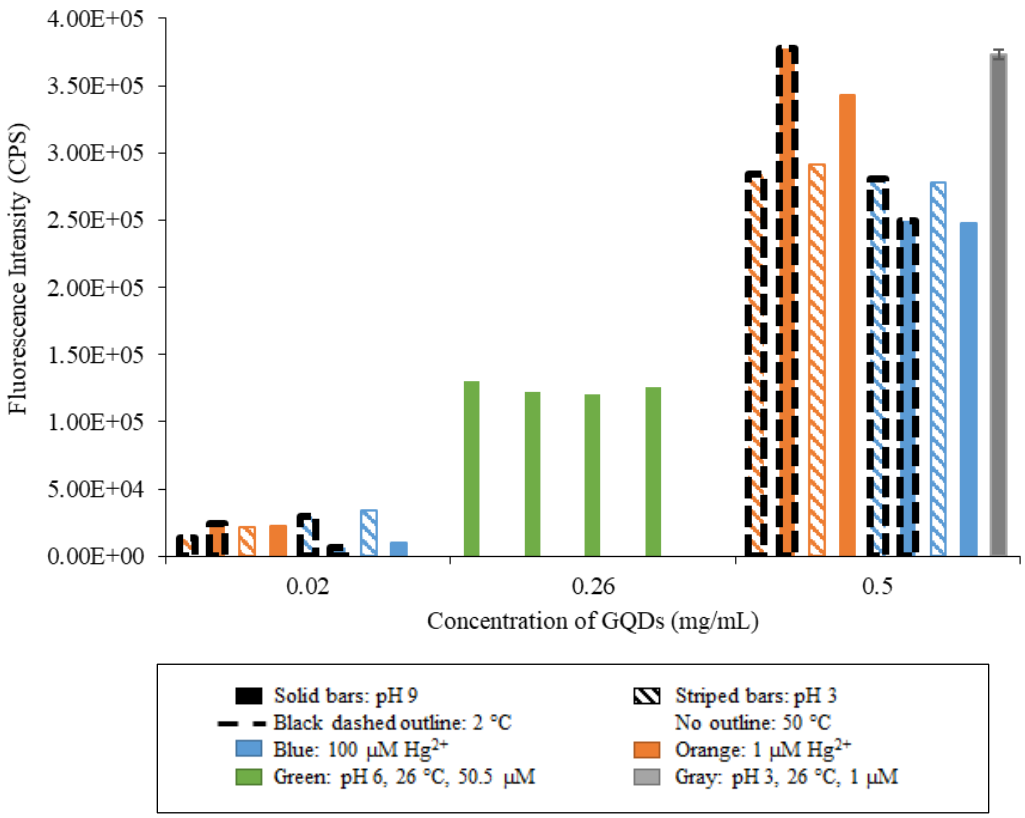

Figure 3.15: All sixteen samples and four center points in comparison to the optimal condition samples (gray). The optimized samples were run in triplicate and their average result contained the highest fluorescence intensity.

Additional concentrations of Hg^{2+} ions were then tested for a better detection limit analysis, ranging from 1 to 100 µM (Figure 3.16). At lower concentrations, 1 and 5 µM, not only did the standard deviation increase but the difference compared to the control was negligible. Concentrations greater than 10 µM where better detected, with a limit of detection (LOD) of 2.5 µM and limit of quantitation (LOQ) of 8.3 µM.

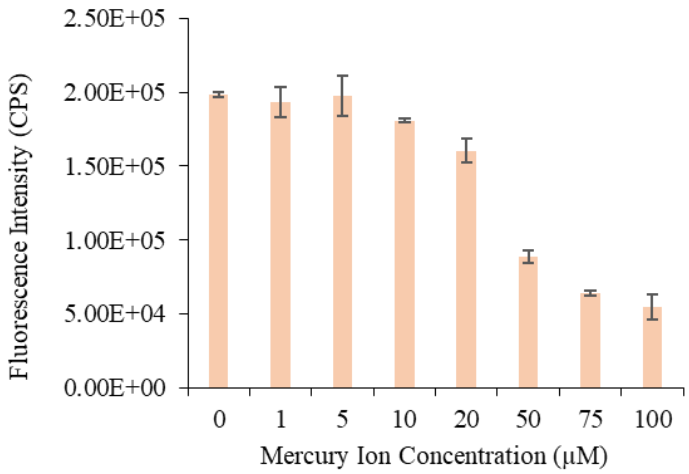

Figure 3.16: Mercury ion detection using the (0.2 mg/mL) GQDs at room temperature in 20 mM pH 7.0 HEPES buffer. LOD: 2.5 µM. LOQ: 8.3 µM.

3.4. Conclusion

Graphene quantum dots (GQDs) were successfully synthesized from biomass-derived CBDA-2 under basic conditions. The optical properties were thoroughly investigated and the GQDs yielded two distinct emission peaks (440 and 850 nm) with one excitation wavelength (310 nm). The GQDs were also stable across a wide pH range, only showing quenching at pH 1.0 and prolonged photostability up to 30 min. When exposed to various metal ions, the GQDs were only quenched by mercury ions down to 10 µM concentrations, LOQ of 8.3 µM. The *in vitro* imaging of MCF-7 depicted strong fluorescent images of the GQDs in the Alexa 488 channel in and RAW 264.7 cells showed excellent biocompatibility. Overall, we developed strong fluorescent GQDs from biomass, providing a novel method for generating fluorescent GQDs for bioanalysis and bioimaging.

CHAPTER IV

SYNTHESIS OF RED-EMISSIVE PORPHYRIN-BASED GRAPHENE QUANTUM DOTS (PGQDS) USING BIOMASS-DERIVED MATERIAL FOR IN VITRO CELL IMAGING

4.1. Introduction

Graphene quantum dots (GQDs) are a subset of semiconductor carbon-based nanoparticles that are defined by their size limitation, being 2-10 nm in diameter.[188,189] GQDs contain unique optical and electrical features that are attributed to the sp^2-hybridized carbon atoms within the lattice of the GQDs which allows them to have a π-conjugated system.[190] This property allows GQDs to be utilized primarily in biological, biomedical, and biosensing fields of study. More specifically, their unique quenching properties enable them to be used for environmental analysis as well as biological, typically in the form of trace molecules, metal ions, cation, and anion detection.[191-194] Additionally, their carbon-based makeup of graphene gives GQDs a low cytotoxicity, further enhancing their use in biological matrices and cell imaging applications. However, GQDs have been reported to typically have blue or green emission light[194-196], which is not optimal for cellular imaging, as shorter wavelength emission light cannot as effectively penetrate tissues, organs, skin, etc. in a biological setting due to light scattering.[197] Red or near infrared (NIR) emission light is a more suitable option for biological imaging, especially for *in vitro* and *in vivo* confocal microscopy.[197,198] However, as previously stated, GQDs and carbon-based nanomaterials are scarcely reported to be synthesized to have a red or NIR emission light.[199] Therefore, researchers have investigated alternative synthesis methods to address this issue and give new GQDs a longer wavelength emission. One such method involves doping GQDs with other elements (nitrogen[200], metals[201,202], etc.) or other nanoparticles[203].

Subsequently, a subgroup of organic molecules that have recently become of interest are porphyrins which, much like GQDs, have unique optical, electrical, and biological properties. Porphyrins are a class of heterocyclic macrocycle organic compounds that are commonly found in nature such as in redox active enzymes like hemoglobin and cytochromes as well as in plant photosynthetic apparatuses.[204] In recent history, porphyrin-based materials have primarily been used for chemical and ion sensing[205], photocatalysis[206], light harvesting[207], and photothermal therapy[208,209]. Porphyrins naturally contain red-emissive fluorescence making them useful for biological imaging applications, however, like other fluorescent dyes, porphyrins lack photostability for prolonged imaging analysis as well as contain self-quenching problems.[210]

To overcome the poor photostability of porphyrins, in combination with an additional photostable carbon molecule may be useful. *Cis*-3,4-di(furan-2-yl)cyclobutane-1,2-dicarboxylic acid (CBDA-2) was used previously and successfully synthesized GQDs with exceptional photostability and cytotoxicity, however, it contained the common emission peak of 440 nm and therefore did not contain the desired red emission.[211] Considering the above mentioned properties of porphyrins and CBDA-2, the goal of this research is to develop porphyrin-based graphene quantum dots (PGQDs) for enhanced red-emission nanomaterial for bioimaging and metal ion detection applications. Meso-tetra(4-carboxyphenyl)porphine (TCPP) is one type of porphyrin with a large conjugated π-electron system and four carboxyl groups on its exterior benzene rings. Given that TCPP has successfully been used previously to nanomaterial synthesis[210] and biological imaging[212] and sensing[213] applications, here, TCPP has also been selected for the porphyrin of choice, while the main carbon contribution will be supplied from biomass-derived CBDA-2 to form PGQDs. Additionally, utilizing CBDA-2, a biomass-derived molecule due to it being derived

from furfural[214], makes this process a synthetically green reaction and the resulting environmentally friendly PGQDs.

4.2. Experimental

4.2.1. Materials

3-(Cyclohexylamino)-1-propanesulfonic acid (CAPS buffer, ≥99%), 2-(cyclohexylamino)ethanesulfonic acid (CHES buffer, ≥99%), 2-[4-(2-hydroxyethyl)piperazin-1-yl]ethanesulfonic acid (HEPES buffer, 99.5%), citric acid (≥99.5%), maleic acid (≥99%), meso-tetra(4-carboxyphenyl)porphine (TCPP). $FeCl_3$, $Pb(Ac)_2 \cdot 3H_2O$, and $CuSO_4$ were purchased from Sigma-Aldrich (St. Louis, MO, USA). $HgCl_2$ was purchased from ACROS Organics (Fair Lawn, NJ, USA). Micro cover glass and $FeSO_4 \cdot 7H_2O$ was purchased from Sargent-Welch VWR Scientific (Buffalo Grove, IL, USA). Fluorescein dye along with ammonium hydroxide (99%) and 96-well plate were purchased from Fisher Scientific (Hampton, NG, USA). CytoTox 96® Non-Radioactive Cytotoxicity Assay kit (showed as LDH assay in following sections) was purchased from Promega (Madison, WI, USA). Deionized (DI) water was produced by a Millipore water purification system (18.3 Ω · cm). HeLa cell line was purchased from ATCC (Manassas, VA, USA). Cell culture media, penicillin-streptomycin and trypsin were purchased from Gibco (Waltham, MA, USA). 4% paraformaldehyde (PFA) was purchased from Electron Microscopy Sciences (Hatfield, PA, USA). Fetal bovine serum (FBS) was purchased from Peak Serum, Inc (Wellington, CO, USA). Fluoromount-G mounting media was purchased from Southern Biotech (Birmingham, AL, USA). 96-well plate was purchased from Thermo Fisher Scientific (Waltham, MA, USA). Cell culture plates were purchased from Greiner Bio One (Kremsmunster, Austrian). Lab-Tek II Chamber Slide system was purchased from Nalge Nunc International Corp (Naperville, IL, USA).

4.2.2. Sample solution preparation

The buffer solutions of CAPS, CHES, HEPES, citric acid, and maleic acid were prepared in concentrations of 20 mM and the pHs of 1.0, 3.0, 5.0, 7.0, 9.0, and 11.0 were adjusted by the addition of NaOH or HCl. For experiments of investigating photostability, dynamic light scattering, and zeta potential measurements, samples were sonicated for 10 – 30 min before analysis. For the detection of metal ions, 1.0 mM solutions of $CuSO_4$, $FeCl_3$, $FeSO_4$, $Pb(Ac)_2$, and $HgCl_2$ were prepared in DI-water for further dilutions as needed.

4.2.3. Instrumentation for the characterization of porphyrin-based GQDs

A Perkin Elmer Lambda 1050 UV-250 UV/Vis/NIR spectrophotometer was used for the UV-Vis absorption measurements of the PGQDs. The fluorescence spectra and photostability measurements were acquired by a Shimadzu RF-6000 spectrophotometer. A Marlvern model of Nano-ZS Zetasizer was used to measure size distribution of the PGQDs as well as the zeta potential at various pHs. A Thermo Fisher Scientific Nicolet iS5 Fourier transform infrared spectrometer (FT-IR) was utilized to obtain the IR spectra of PGQDs, TCPP, CBDA-2 and the GQDs. A Hitachi 7500 Transmission Electron Microscope (TEM) and a JEOL JEM-F200 High-resolution Transmission Electron Microscope (HRTEM) were used for particle imaging. Powder X-ray diffraction (XRD) measurement was conducted on a Rigaku SmartLab X-ray diffractometer at a scan rate of 4 °/min with Cu Kα irradiation ($\lambda = 0.15418$) at an accelerating voltage of 40 kV and a tube current of 44 mA. The fine powder sample was loaded on a zero-background silicon wafer sample holder. An Olympus FV1000 MPE Basic Multiphoton Microscope was used for *in vitro* confocal imaging. HeLa cells were cultured over night with gradient concentrations of the PGQDs for *in vitro* imaging and cytotoxicity analysis. A ELX800 plate reader was used for the cell viability experiments using the protocol of CytoTox 96® Non-Radioactive Cytotoxicity Assay kit.

4.2.4. Synthesis of PGQDs

16.0 mg of CBDA-2 and 12.5 mg of TCPP were dissolved in 15.0 mL of DI-water and 100 µL of ethylenediamine before sonication for 30 min. The resulting solution was then autoclaved for 12 h at 200 °C. After those 12 h the solution was removed and allowed to cool to room temperature before filtration using a 0.22 µm syringe filter and then dialyzed for 3 days using a 500-1000 Da membrane against DI-water. When exposed to UV light, the PGQDs solution visibly showed red-emission light compared to GQDs blue-emission.

4.2.5. Quantum yield

The quantum yield of the PGQDs (650 nm) peak in HEPES buffer pH 7.0 was calculated against quinine sulfate in 0.1 M H_2SO_4 (Φ_{st} of 0.54) and FITC in 0.1 M NaOH (Φ_{st} of 0.79) as both were used as the standard reference.[172] Calibration curves of fluorescence intensity *vs* absorbance for the PGQDs and standard references were generated and, utilizing Equation 4-1 below, the quantum yield of PGQDs was calculated to be 46.6% against both standards; where Φ_x is the fluorescence quantum yield of the PGQDs, Φ_{st} is the quantum yield of the standard, $Grad_x$ and $Grad_{st}$ are the gradients of the calibration curve fluorescence intensity *vs* absorbance for the PGQDs and standards, respectively. η_x and η_{st} are the refractive index of the solvents for the PGQDs and standards. This is an exceptional quantum yield for graphene-based quantum dots, and additionally acceptable for PGQDs as well.

$$\Phi_x = \Phi_{st}\left(\frac{Grad_x}{Grad_{st}}\right)\left(\frac{\eta_x^2}{\eta_{st}^2}\right) \qquad (4-1)$$

4.2.6. Cell experiments and cell imaging

The viability of cells exposed to PGQDs was tested with a CytoTox 96® Non-Radioactive Cytotoxicity Assay kit. Briefly, the cells were incubated with PGQDs in a 96-well plate overnight.

A gradient concentration of PGQDs (0, 1, 5, 10, 20, 50, 100, and 200 μg/mL) was added into the wells. After 24 h, 50 μL aliquots of media from all groups were transferred to a new 96-well plate and mixed with 50 μL of the CytoTox 96® Reagent solution. After a 30 min incubation in the dark, 50 μL of the Stop Solution were added to the wells and viability was assessed by reading absorbance at 490 nm.

HeLa cells were plated into an 8-well chamber slide overnight for *in vitro* imaging. 20 mg/mL PGQDs were added into different wells for 3 h while a control was prepared for each sample. Then the slide was washed with PBS and the cells were fixed with 4% paraformaldehyde (PFA). The chamber wells were removed, and the slide was coverslipped for imaging

4.3. Results

4.3.1. Design of the PGQDs synthesis

A key component of this synthesis is using a biomass-derived molecule, making the product synthetically "green" and environmentally friendly. CBDA-2 was successfully derived from hemicellulose taken from agriculture corn waste products through a serious of chemical reactions including Knoevenagel condensation and blacklight radiation.[214] There are several means of which to incorporate the red emission into GQDs as discussed previously. Keeping true to the use of natural material in order to reduce waste and the use of harmful chemicals, porphyrins were examined as an alternative. Given the status of porphyrins being pigments found throughout nature in several different forms, these unique molecules already contain the highly desirable red-emission. However, like other fluorescent dyes and pigments, porphyrins suffer from poor photostability and photobleaching. The design of this experiment is to utilize the strengths of both porphyrins and CBDA-2 such that they counter each other's weaknesses. In this work, the

porphyrin TCPP was chosen to be incorporated with CBDA-2 due to its successful use in nanoparticle synthesis in other studies[215]. Given that the use of porphyrins to synthesize nanoparticles is limited, and to minimize potential unforeseen issues in the synthesis procedure, it was vital to use a porphyrin that was successfully used previously when used in this work because the two components of CBDA-2 and TCPP have never been used in tandem. The synthesis route was shown in Schematic 4.1.

To synthesize the PGQDs, 20.0 mg CBDA-2 and 16.0 mg TCPP were dissolved in 20 mL of DI-water. To aid the compounds dissolving, the solution pH needs to be adjusted to a basic pH of 10.0 for CBDA-2. NH_4OH was used for this pH adjustment before autoclaving the sample at 200 °C for 12 h. The resulting solution was allowed to cool to room temperature before it was filtered with a 0.22 µm syringe filter and subjected to dialysis for 3 days against a 500-1000 Da membrane. Although GQDs contain an absorption at approximately 300 nm, the PGQDs showed a strong absorption peak at 420 nm which is consistent with TCPP absorption (416 nm), just slightly shifted. However, despite filtration and dialysis, residual TCPP was still accumulated in the solution as Q-bands were observed in the range of 475 – 655 nm, which are not typically retained after synthesis into forms of nanoparticles (Figure 4.1).

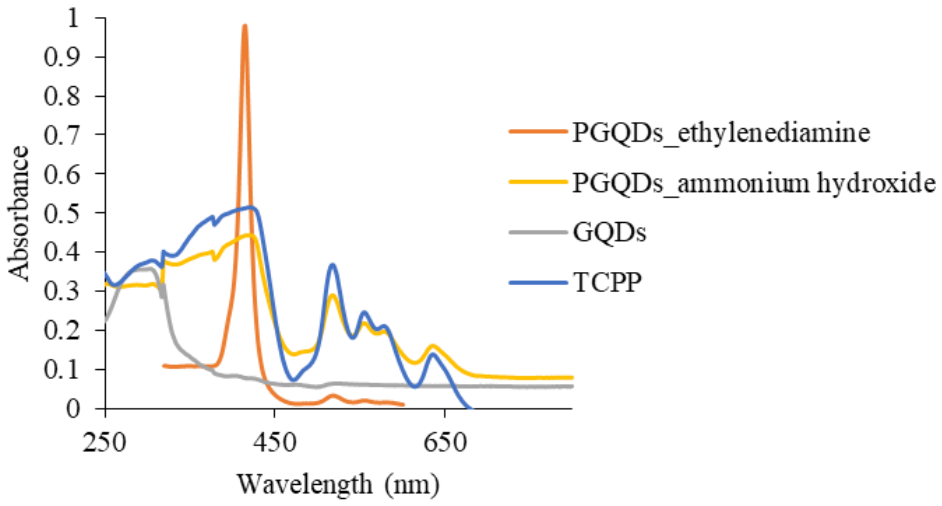

Figure 4.1: Synthesis of PGQDs utilizing NH_4OH (75 µg/mL) and ethylenediamine (40 µg/mL) compared to GQDs (20 µg/mL) previously synthesized and TCPP (50 µg/mL).

To resolve this issue of residual TCPP and Q-bands, the synthesis was adjusted and instead of using NH_4OH to dissolve CBDA-2 and TCPP, 100 µL ethylenediamine was used due to its greater nucleophilic tendencies toward oxygen functional groups on the formed GQDs.[216] The rest of the reaction synthesis remained the same (Schematic 4.1) and after dialysis, the PGQDs were dried at 60 °C in an autoclave oven which also helped remove any residual TCPP while still containing the red-emissive particles, as discussed later.

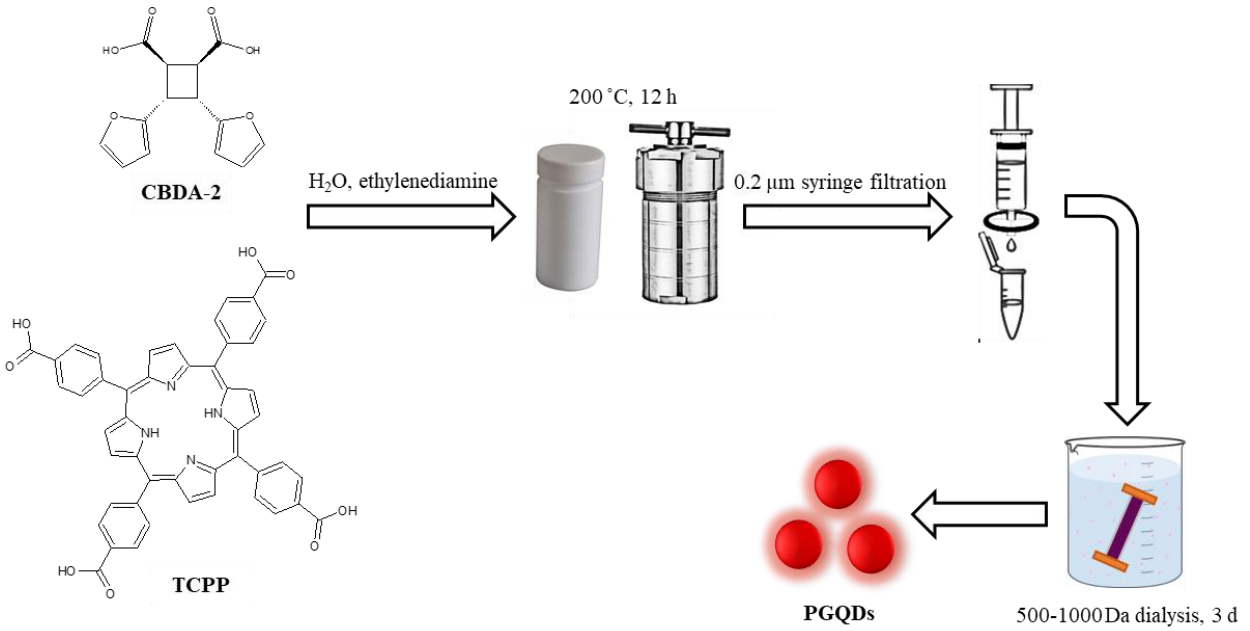

Schematic 4.1: Combination of CBDA-2 and TCPP to synthesize PGQDs. Experimental conditions: 200 °C for 12 h before 0.2 µm syringe filtration and dialysis for 3 d in 500-1000 Da membrane against DI-water.

4.3.2. Characterization of PGQDs

4.3.2.1. Morphology and size of PGQDs

QDs have a strict size definition of 2 – 10 nm and therefore it is essential to determine the size distribution of the newly synthesized particles to ensure their characterization as QDs. To do this, the morphology of the PGQDs was characterized using both regular TEM and high-resolution TEM (HRTEM). TEM images were first acquired (Figure 4.2A), which depicted large particles clusters; the largest being 24.7 nm and smaller particles ranging from 2.7 – 4.7 nm. The smaller particles were more abundant than the larger particles, however, the lower resolution of the TEM images made it difficult to distinguish clusters from large individual particles. Therefore, HRTEM images were also examined in order to better differentiate particles from each other. HRTEM images (Figure 4.2B) depicted particles with an average diameter of 7.5 nm. Furthermore, the

internal graphene lattice was visible in the image. However, additional complications arose with HRTEM imaging as the carbon-based PGQDs were set against a carbon mesh, resulting in the smaller particles fading into the background and becoming difficult to accurately measure the lattice size. To confirm the graphene lattice, XRD of the PGQDs was analyzed, which will be discussed later.

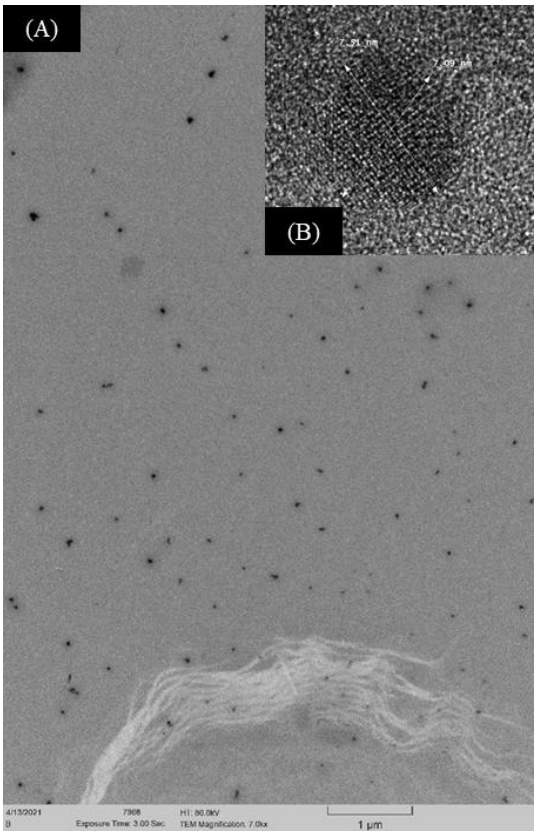

Figure 4.2: TEM images of 750 µg/mL PGQDs; (A) TEM image of cluster with particles 2.7 – 4.7 nm in size. (B) HRTEM image of single 7.51 nm particle with graphene lattice.

With the HRTEM carbon-mesh imaging complications, and after seeing some agglomeration of the PGQDs in the TEM images, the particles were analyzed by DLS at various concentrations with various sonication times in order to optimize conditions for minimal agglomeration and more accurate determine particle size distribution. Ultimately, it was found that

the sonication time was proportional to the concentration of PGQDs. Lower concentrations required less sonication time. If the sonication was prolonged, the PGQDs would agglomerate. Concentrations of 5.0 µg/mL only required 5 min of sonication to limit agglomeration, however, exceeding 10 min of sonication showed a drastic increase in agglomeration. The same was true of higher concentrations, such as 30 µg/mL, which required a minimum sonication time of 30 min, but could not exceed 60 min without showing the same drastic increase in agglomeration. The optimal conditions for PGQDs to limit agglomeration was 5.0 – 30.0 µg/mL with proportional sonication times, not exceeding 60 min for the highest concentration (Figure 4.3). The average particle size utilizing DLS was 7.9 ± 4.1 nm which is consistent with the observable particles in both the TEM and HRTEM images.

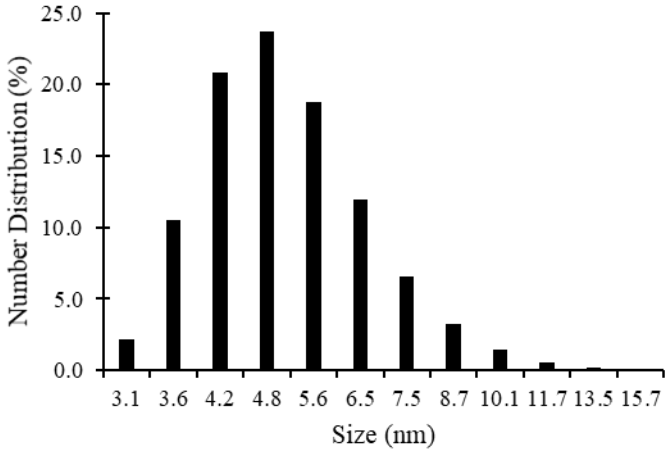

Figure 4.3: DLS analysis of 5.0 µg/mL PGQDs in DI-water (sonicated for 5-10 min). Average particle size was found to be 7.93 ± 4.1 nm.

4.3.2.2. Surface functional groups and elemental characterization of PGQDs

With the morphology and size characterization of the PGQDs showing encouraging results, further analysis was required to better understand the composition of the PGQDs. Therefore, the elemental makeup and functional group formation needed to be determined. The initial particle

surface characterization was found through zeta potential, an electrical potential found at the slipping plane, of particles in suspension that is used to help predict surface interactions and long-term stability. Zeta potential of particles is also valuable to determine whether the particles could be used in biological applications, as the surface charge of the particles impacts their interaction with the surface of the cell. However, there are many factors that affect zeta potential and one of the more important factors is pH. More basic conditions will result in a buildup of negative charge while acidic conditions will build up a positive charge. Depending on the charge of the particles, switching the charge to positive or negative can result in the particles' surface charge being neutralized, resulting in a zero zeta potential that causes the particles to agglomerate and fall out of suspension. Due to these particles being targeted for biological applications, it is vital to determine that the PGQDs are stable in neutral pHs and do not agglomerate.

Therefore, the zeta potentail of PGQDs was tested in a pH range of 1.0 - 11.0, and the PGQDs depict an interesting trend. Despite the pH range of 1.0 - 11.0, the PGQDs showed relatively stable zeta potentials throughout compared to regular GQDs[211] with no clear linear trend (Figure 4.4). This is most likely due to the nitrogen in TCPP that can maintain a positive charge in solution with decreasing pH as traditional GQDs do not contain nitrogen groups for positive charge stability. The most stable zeta potential was observed at pH 11.0 (-35.0 mV), which then decreases in pH 9.0 (-23.6 mV) and 7.0 (-22.2 mV) before slightly increasing in pH 6.5 (-24.8 mV) and pH 5.0 (-27.8 mV). This slight increase in the more neutral-acidic region could be due to equilibrium forming between the negative charge on oxygen groups and the positive charge on nitrogen groups. After pH 5.0, the zeta potential flips positive for pH 3.0 (+22.7 mV) and pH 1.0 (+23.8 mV), however, the potential is still showing mild stability indicating that the particles are not

agglomerating due to the nitrogen groups on TCPP withstanding the pH change and increase positive charge in solution.

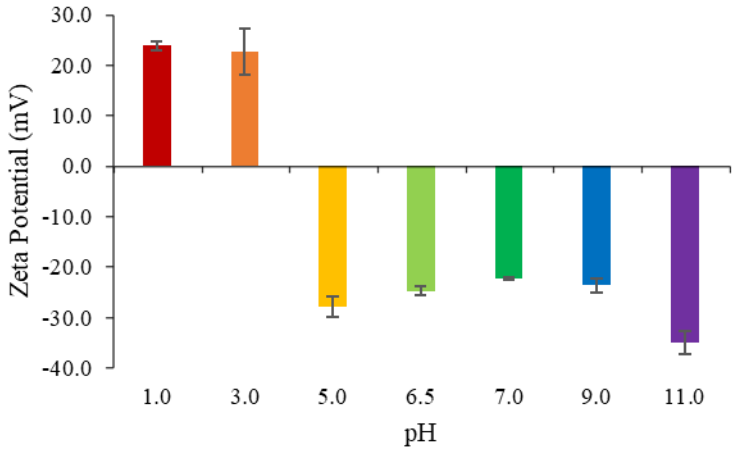

Figure 4.4: Zeta potential measurements of 38 µg/mL PGQDs in pH 1.0-11.0 buffer solutions after 30 min sonication.

The surface functional groups were characterized using FT-IR. The FT-IR spectra of GQDs, PGQDs, CBDA-2 and TCPP (Figure 4.5) were analyzed to determine functional groups and any chemical changes that occurred during the synthesis process. For the PGQDs, it was observed that the streching vibration frequency (black dashed line) of carbonyl attached to porphyrin macrocycles was missing compared to TCPP. Additionally, PGQDs contain C=C (1647 cm^{-1}, green (a)) and C=N (1541 cm^{-1}, blue (b)) double bonds that are broadened, suggesting a chemical change and the formation of QDs. PGQDs also contain the same C=N peak (1378 cm^{-1}, yellow (c) green dashed line) that is also observed in TCPP, suggesting that the porphyrin ring was maintained throughout the synthesis that was contributing to the PGQDs fluorescence characteristics.[217]

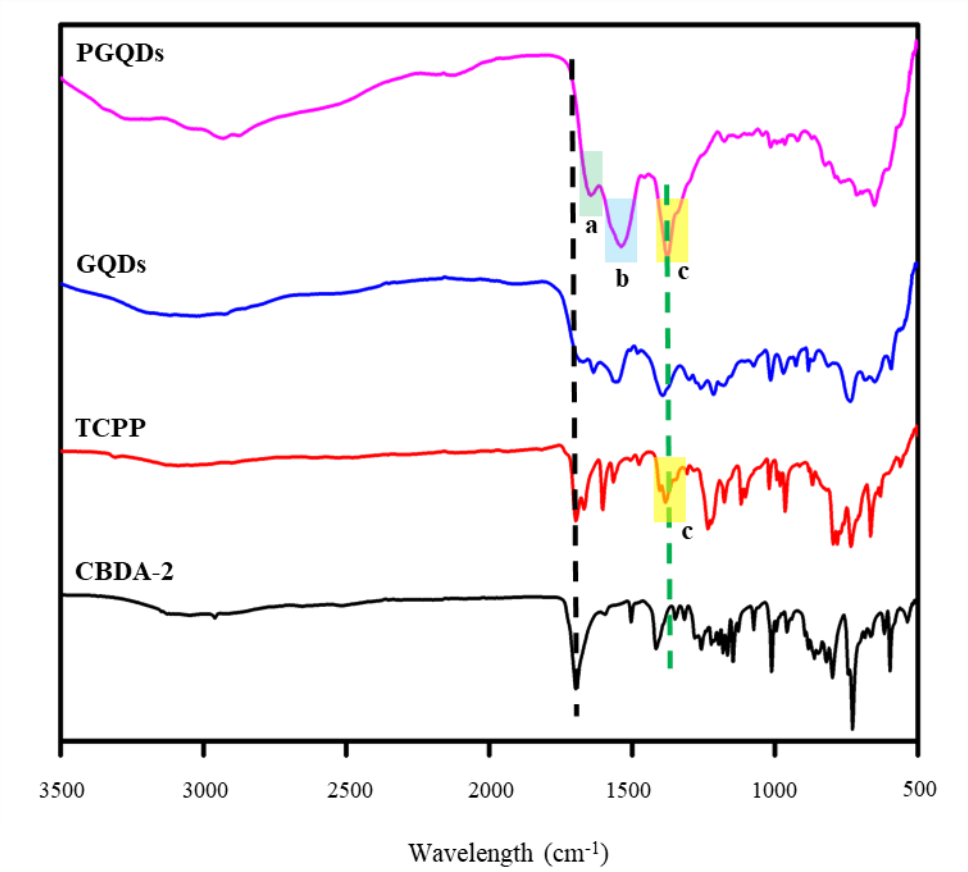

Figure 4.5: FT-IR spectra of GQDs, PGQDs, TCPP, and CBDA-2, all dried to a powder.

The presence of these functional groups was confirmed with the use of XPS, a form of elemental analysis. The XPS spectrum (Figure 4.6A) shows three distinct element peaks of carbon (285 eV), nitrogen (400 eV), and oxygen (533 eV). This is consistent with the elements observed in both starting compounds and the bonds observed in FT-IR. Both TCPP and CBDA-2 contribute to the oxygen and carbon peaks while only TCPP will contain nitrogen, further confirming the presence of the porphyrin ring being maintained through the synthesis process. This also explains the abundance of carbon and oxygen compared to nitrogen.

Additionally, the graphene lattice is essential in this work as its formation aids in the structural stabilization of the particles compared to carbon quantum dots without the internal lattice due to different hybridization. To confirm the graphene lattice, XRD of the PGQDs was analyzed. A shallow peak at 20° in the XRD spectrum of the PGQDs (Figure 4.6B) points to carbon in a graphene lattice[218] while no other peaks were observed in the spectrum.

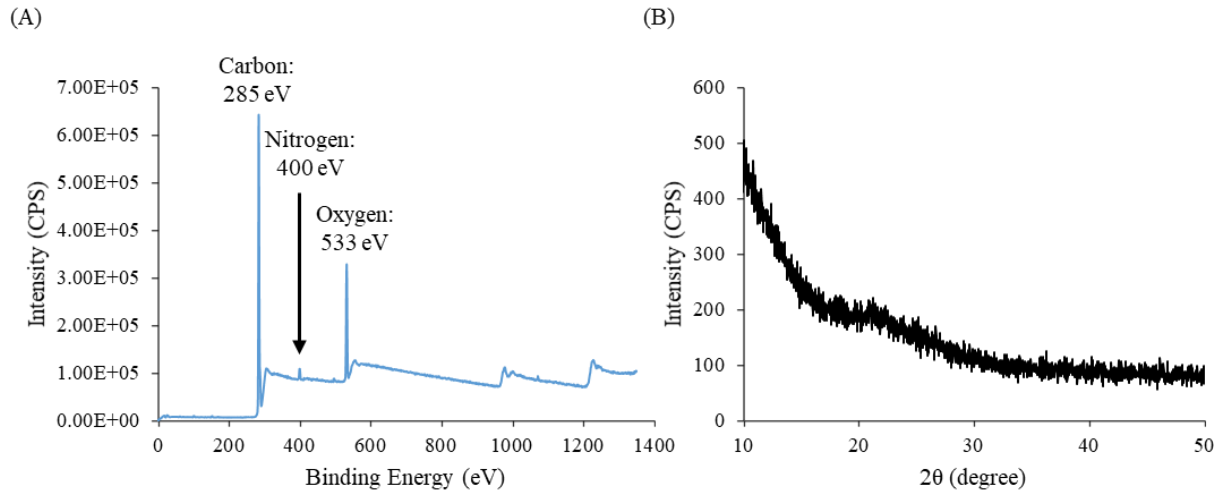

Figure 4.6: (A) XPS spectrum of the PGQDs shows carbon, nitrogen, and oxygen peaks. (B) XRD spectrum of dried powder PGQDs shows graphene lattice at 20°.

4.3.3. Optical properties of PGQDs

With the aim of this work being targeted for cell fluorescence imaging, it is important to acquire information on the PGQDs optical properties. This includes absorption and fluorescence as well as solution condition impacts such as pH, concentration, and excitation. The absorption spectrum of PGQDs after synthesis and drying (Figure 4.7A) showed a decrease in Q-bands from residual TCPP. Furthermore, drying the PGQDs to remove residual TCPP did not impact the fluorescence spectrum which shows a peak excitation of 420 nm that yields an emission peak at 650 nm (Figure 4.7B); again, slightly shifted from previously noted TCPP fluorescence of 416 nm

excitation and 640 nm emission. This strongly indicates that the red emission is coming from the PGQDs and not residual TCPP in solution. Additionally, changing the excitation light for the PGQDs (Figure 4.7C) shows no radiation dependent behavior as there is no noted red-shifting with increasing excitation light was seen with GQDs, previously. The PGQDs do, however, show concentration dependency (Figure 4.7D) as increasing concentrations of PGQDs increases the fluorescence intensity. This is vital due to porphyrins known self-quenching tendencies[219,220] with increasing concentration and thus the attachment of TCPP to the GQDs has aided in removing this self-quenching characteristic.

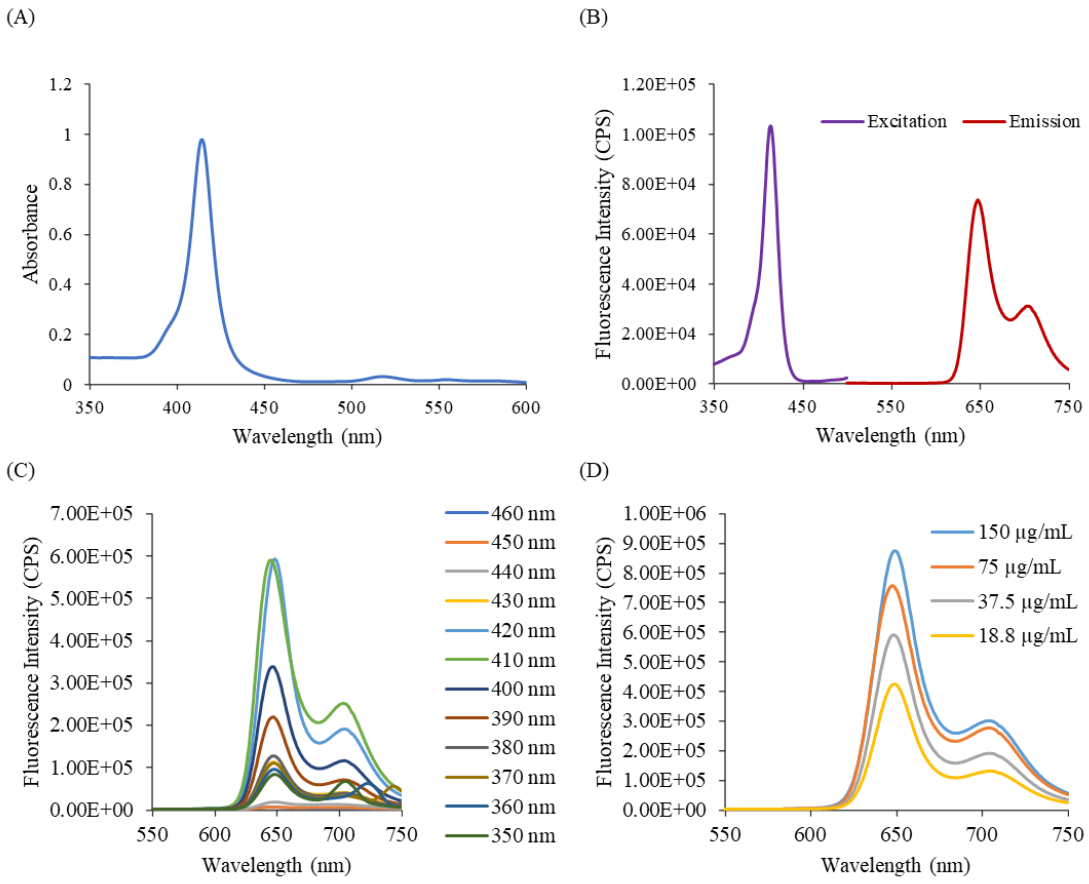

Figure 4.7: Optical properties of PGQDs. (A) Absorption profile of PGQDs. (B) Excitation (420 nm) and emission (650 nm) fluorescence spectrum of PGQDs (37.5 µg/mL) in 20 mM HEPES pH 7.0 buffer. (C) Changing excitation light for PGQDs depicts excitation-dependent properties. (D) Changing concentration of PGQDs.

Additionally, for the use of these PGQDs in bioanalysis and bioimaging, the stability and potential quenching of these particles in different pHs is critical to determine. Negatively surface charged GQDs are well known to experience quenching in acidic conditions, such as pH 1.0, due to full protonation of oxygen and carboxy functional groups[221,222] leading to agglomeration. Therefore, the PGQDs fluorescence were tested in the same pH range of 1.0 - 11.0 where the fluorescence decreases linearly until pH 6.5, where it drastically drops to near zero fluorescence intensity at pH 5.0, 3.0, and 1.0. Fluorescence quenching at pH 3.0 - 5.0 is attributed to the agglomeration of carbon-based particles in acidic conditions and the degradation of the π-bonds in the porphyrin ring[223] of the PGQDs rather than agglomeration due to the zeta potential analysis previously discussed (section 4.3.2.1) showing particle stability and little to no agglomeration of the PGQDs in pH 1.0 - 5.0 (Figure 4.8).

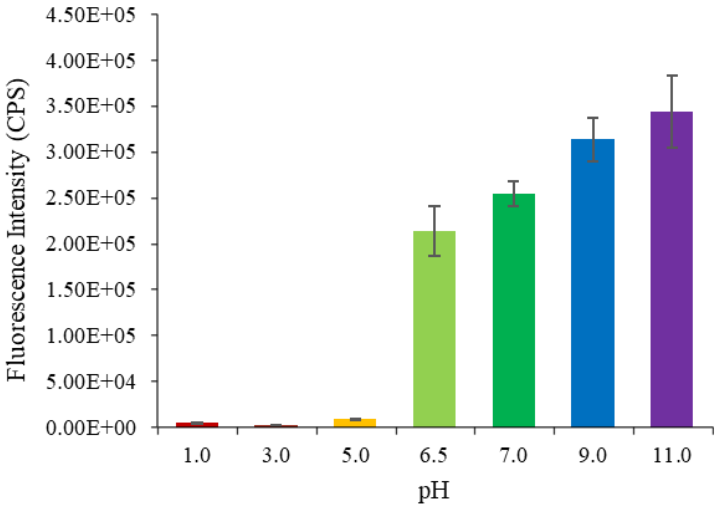

Figure 4.8: Fluorescence intensity measurements of the PGQDs shows quenching effects in maelate pH 1.0 and citrate pH 3.0 – 5.0 while neutral and basic pHs of 6.5 – 11.0 (HEPES 6.5 – 7.0, CHES 9.0, and CAPS 11.0) depict an increasing fluorescence signal with the more alkaline the solution becomes. All solutions were 190 μg/mL PGQDs.

However, the stability and maintenance of fluorescence in the neutral pHs is encouraging for the biological application of cell imaging these PGQDs are targeted for. However, TCPP and other porphyrins are well known for their poor photostability[224,225] and therefore vital for the application of cell labeling to improve the photostability for prolonged analyses and cell imaging without the fluorescence signal being lost. Therefore, the photostability of the PGQDs was examined in comparison to previously made GQDs from CBDA-2[226] and FITC dye as a standard (Figure 4.9). After 30 min of excitation light exposure, the PGQDs (excitation 420 nm, emission 650 nm) decreased to 63.7% of their original intensity compared to 67.1% of the GQDs (excitation 310 nm, emission 440 nm). FITC (excitation 495 nm, emission 519 nm) decreased to 8.7% after the 30 min trial, losing 80% of its original intensity in the first 700 sec. Therefore, it can be concluded that the PGQDs exhibit exceptional photostability for prolonged analysis applications.

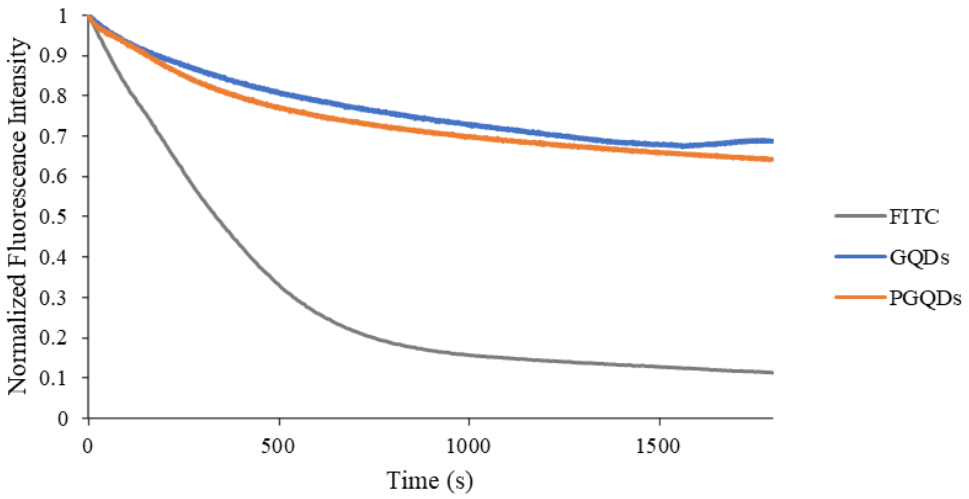

Figure 4.9: Photostability of FITC, GQDs, and PGQDs. FITC was prepared in 20 mM CHES pH 9.0 while both GQDs and PGQDs were in 20 mM HEPES pH 7.0.

4.3.4. In vitro cell imaging

The feasibility of the particles to be used as fluorescent agents in cell labeling was examined as well to determine particle-cell compatibility. For this purpose, the cytotoxicity was evaluated, utilizing the LDH assay with HeLa cells for 24 h incubation. The results (Figure 4.10) show negligible toxicity in comparison to the control group with PGQDs up to 200 µg/mL, strongly indicating superior biocompatibility of the PGQDs, although there is some evidence of graphene-based particle toxicity at concentrations higher than 500 µg/mL[226,227].

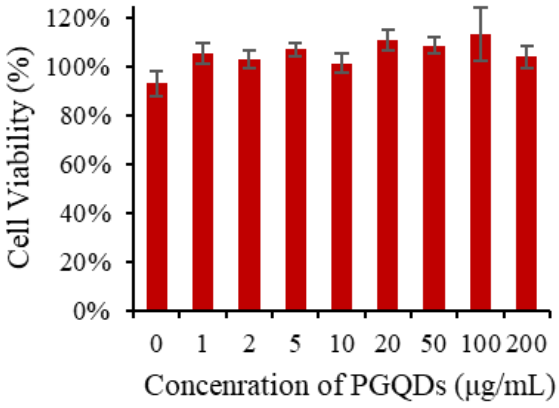

Figure 4.10: LDH assay results of PGQDs incubated with HeLa cells 24 h at various concentrations.

The negligible cytotoxicity results indicated that the PGQDs might be used as fluorescent cell staining agents. To test this idea, HeLa cells were incubated with PGQDs for 3 h before the cells were fixed and imaged via fluorescence confocal microscopy using the Alexa 488 channel. Control HeLa cells with no PGQDs were imaged (Figure 4.11A) along with the brightfield image of the cells demonstrating minimal basal autofluorescence (Figure 4.11B). However, the HeLa cells with PGQDs (Figure 4.11C) demonstrated robust staining verifying cellular uptake of the

PGQDs. Brightfield imaging verified an intact morphologic phenotype of the PGQDs treated cells consistent with no toxicity at this concentration (Figure 4.11D).

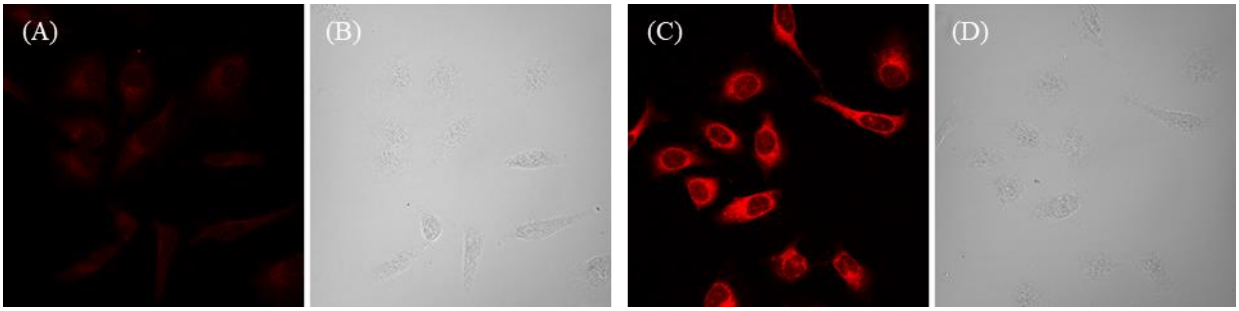

Figure 4.11: (A) HeLa cells with no PGQDs. (B) Brightfield of blank HeLa cells. (C) 20 µg PGQDs incubated with HeLa cells. (D) Brightfield of PGQDs with HeLa cells.

Lastly, with porphyrins being known to be sensitive to metal ions[228-232], various metal ions were tested to ensure that the natural concentration of metals in biological systems would not interfere with the fluorescence intensity of the PGQDs. Metal ions of Fe^{3+}, Fe^{2+}, Cu^{2+}, Pb^{2+}, and Hg^{2+} were analyzed at concentrations of 1, 5, 10, and 50 µM (Figure 4.12). Fe^{3+} and Fe^{2+} showed the least quenching up to 50 µM. Pb^{2+} showed the most linear decrease in fluorescence intensity with increasing concentrations. Cu^{2+} showed the greatest quenching, dropping to less than 50% of the original fluorescence intensity at 5.0 µM, and was completely quenched at 50 µM. Hg^{2+} only slightly decreased up to 10 µM but then quenched to 40% fluorescence intensity with 50 µM. However, with no significant quenching with the lowest concentration of metal ions (1.0 µM), it is safe to confirm that the natural concentrations of metal ions in biological systems would not significantly impact the fluorescence intensity of the PGQDs negatively.

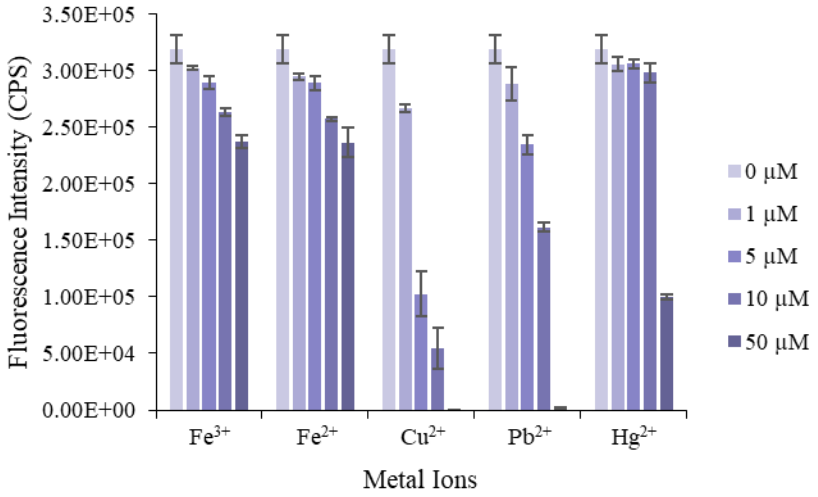

Figure 4.12: Metal ion analysis at various concentrations with 20 µg/mL PGQDs in 20 mM HEPES buffer pH 7.0.

4.4. Conclusions

Slight modification to the GQDs synthesis by using ethylenediamine instead of NH_4OH and introducing TCPP yielded red-emissive particles with similar quantum yield (46.6%). After drying the PGQDs at 60 °C, residual TCPP was successfully removed from the material. TEM and HRTEM images showed particles of 7.51 nm with an internal graphene lattice and some larger particle clusters, which resulted in the PGQDs being sonicated to help alleviate the agglomeration. DLS showed that the PGQDs agglomeration was proportional to concentration and sonication time. Lower concentrations of PGQDs required less sonication time, otherwise agglomeration would spike. Similarly, higher concentrations of PGQDs required longer sonication times yet had a time cut-off before agglomeration would worsen drastically. XPS, XRD, and FT-IR confirmed the presence of carbon-nitrogen bonds in the PGQDs as well as a graphene lattice. Zeta potential also indicated the presence of nitrogen as the particles were stable in acidic and basic pHs.

However, fluorescence quenching was observed for pHs > 6.5, most likely due to degradation of TCPP π-bonds in the porphyrin ring.

The various fluorescence spectra of the PGQDs shows a slightly shifted excitation and emission peak compared to TCPP, as well as a concentration dependency. However, no radiation dependency was noted, which was present in the GQDs also synthesized from CBDA-2. Cytotoxicity results showed negligible difference between the various concentration of PGQDs compared to the blank control, up to 200 μg/mL. *In vitro* confocal microscopy images of PGQDs incubated with HeLa cells showed exceptional particle integration into the cells that resulted in clear images for cell staining applications.

CHAPTER V

DEVELOPMENT OF BIODEGRADABLE GQDS-HMSNS FOR FLUORESCENCE IMAGING AND DUAL CANCER TREATMENT

5.1. Introduction

Cancer is one of the leading causes of death around the world[233] and since its discovery researchers have tried multiple means of treatment to find a cure for the deadly disease. Current methods of cancer treatment such as chemotherapy and radiology, although common and effective, are aggressive and as a result cause damage and stress to the patient under treatment. Physical symptoms of fatigue, hair loss, neutropenia, lymphedema, deep vein thrombosis, and psychological symptoms such as depression and memory loss are a short list of side effects brought on by traditional cancer treatment methods.[234-237] Therefore, several disciplines such as medicine, biology, and chemistry have begun to research alternative means of cancer treatment with less severe side effects for a better quality of life.[238-240] Nanoscience is one such discipline that has extensively researched the use of nanoparticles for cancer treatment.[241] Nanoparticles contain several unique properties that are being exploited, in the hope of finding new treatment methods that are not as taxing on the patient.

GQDs are a subset of nanoparticles defined by their size range of 2 – 10 nm. These particles contain several key characteristics including biocompatibility, low toxicity, resistance to photobleaching, high photostability, and photoluminescence that make them applicable in biological applications.[242,243] One vital feature of GQDs is their fluorescence capabilities, which allows them to be extensively used for bioimaging applications.[244-246] Over recent years, GQDs have been studied for their use in photodynamic therapy (PDT) for cancer treatment.[247] GQDs contain the natural ability to generate reactive oxidative species (ROS) due to the carbonyl

functional groups found on their surface, which create a cytotoxic mechanism in the target cancer cell, though the exact pathway is still unknown.[248] Under physiological conditions, cells continuously generate and eliminate ROS compounds and naturally control these fluctuating ROS levels.[249] However, disturbance in these pathways, such as excessive ROS levels, leads to DNA, protein, lipid damage, and other interrupted cellular pathways.[249,250] For effective PDT treatment there are three base requirements: a photosensitizer (PS), light, and oxygen.[251] Ideally for PDT, the cancer cells absorb the PS, in this case the GQDs, which are activated by light to form ROS compounds that terminate the harmful cells through either apoptosis, necrosis, or autophagy.[252] GQDs have proven to be viable candidates in previous experiments for PDT treatment as they generate $^1O_2$ and contain fluorescence characteristics.[253-255] However, due to their small particle size, GQDs struggle to remain in the target area for long periods of time in addition to being poor drug carriers.

Additionally, hollow mesoporous silica nanoparticles (hMSNs) have many unique properties for drug encapsulating capacity, drug release behavior, and enhancing antitumor immunity.[256] hMSNs are known to be highly biocompatible and biodegradable due to pH sensitivity[257], allowing for the avoidance of accumulation in the human body and making them viable for drug delivery applications.[257-260] Features such as surface modifications[261], pore size[262], and pore volume[263] allow hMSNs to be tailored for the drug type which they are intended to deliver into the targeted cancer cell.[264,265] Due to the intrinsic properties of GQDs and hMSNs, they are two kinds of many nanoparticles that have been extensively researched for their cancer treatment abilities.

Recently, research has been conducted utilizing GQD and hMSN nanoparticles in tandem for dual cancer treatment of PDT and drug delivery in addition to cell imaging.[266-269] For the goals

of this study, biomass-derived GQDs and biodegradable hMSNs will be synthesized together to make degradable GQDs-hMSNs that are also uniquely efficient at drug delivery, ROS formation, and fluorescence imaging. GQDs are synthesized in one of two ways: top-down or bottom-up.[270] The top-down method starts by breaking down carbon material using methods such as lithography and oxidation and bottom-up combines smaller carbon-containing compounds using methods such as pyrolysis and hydrothermal heating. For this project, GQDs will be synthesized from biomass-derived material[271] by dissolving the organic compound and subjecting the solution to heat for an extended time. For hMSNs synthesis, due to the vast number of synthesis methods that all impact the MSNs' ability to treat cancer effectively, it remains an important and innovative field of research. This study will use the Stöber method[272] which has successfully synthesized MSNs in the past and use Na_2CO_3 to hollow out the MSNs[270] into hMSNs.

A variety of analytical instrumentation were used to characterize the new GQDs-hMSNs. Firstly, their size distribution was examined using transmission electron microscopy (TEM) and dynamic light scattering (DLS) due to nanoparticles being defined by their size range of one dimension being 1-100 nm[273] and previous studies showing that nanoparticle size range greatly impacts their cell interactions[274,275]. Elemental composition analysis was determined using XPS to confirm the presence of silicon, oxygen, and carbon along with FT-IR to confirm bond formations. Zeta potential was determined due to solution stability and surface charge playing vital roles in cellular interactions, as charged particles typically are better ingested by cells than noncharged particles.[276,277] Then, their UV-Vis absorption and fluorescence features were collected to facilitate fluorescence imaging. Their biodegradability was also be tested using various pH solutions[278] to mimic biological environments. Lastly, utility was assessed for *in vitro* fluorescence cell imaging using confocal microscopy, ROS formation using cell viability tests for type II PDT treatment due

to $^1O_2$ formation via GQDs[278,279], and drug delivery by examining loading and releasing capabilities into the targeted cancer cells using FITC dye as a mock drug[280].

5.2. Experimental

5.2.1. Materials and sample preparations

A Millipore water purification system (18.3 Ω · cm) was used to produce deionized (DI) water. 3-(cyclohexylamine)-1-propanesulfonic acid (CAPS buffer, ≥99%), 2-(cyclohexylamino)ethanesulfonic acid (CHES buffer, ≥99%), 2-[4-(2-hydroxyethyl)piperazin-1-yl]ethanesulfonic acid (HEPES buffer, 99.5%), citric acid (≥99.5%), maleic acid (≥99%), phosphate-buffered saline (PBS buffer, tablet), dimethyl sulfoxide (DMSO, ≥99.7%), triethanolamine (TEA, ≥99%), tetraethyl orthosilicate (TEOS, 98%), cetyltrimethylammonium chloride (CTAC, 25 wt. % in H_2O), (3-aminopropyl)triethoxysilane (APTES, 99%), and cyclohexane (anhydrous, 99.5%) were purchased from Sigma-Aldrich (St. Louis, MO, USA). RAW 264.7 cells cell line was purchased from ATCC (Manassas, VA, USA). Cell culture media, penicillin-Streptomycin and trypsin were purchased from Gibco (Waltham, MA, USA).4% paraformaldehyde (PFA) was purchased from Electron Microscopy Sciences (Hatfield, PA, USA). Fetal bovine serum (FBS) was purchased from Peak Serum, Inc (Wellington, CO, USA). Fluoromount-G mounting media was purchased from Southern Biotech (Birmingham, AL, USA). 96-well plate, CyQUANT™ LDH Cytotoxicity Assay kit, Invitrogen LysoTracker ™ Red DND-99, and TO-PRO-3 were purchased from Thermo Fisher (Waltham, MA, USA). Cell culture plates were purchased from Greiner Bio one (Kremsmunster, Austrian). Lab-Tek II Chamber Slide system was purchased from Nalge Nunc International Corp. (Nalerville, IL, USA). The Micro cover glass was purchased from Sargent-Welch VWR Scientific (Buffalo Grove, IL, USA).

Olympus FV3000 Laser Scanning Confocal Microscope was purchased from Olympus Corporation (Shinjuku City, Tokyo, Japan). EXL800 microplate reader was purchased from Bio Tek (Winooski, VT, USA).

Buffers of maleic acid, citric acid, HEPES, CHES, and CAPS were prepared in 20 mM concentrations, and additional 10 mM PBS and citrate, in DI-water with the pH being adjusted by the addition of HCl or NaOH. Zeta potential and DLS samples were subjected to sonication for 5-10 minutes before analysis. For the drug delivery application of the GQDs-hMSNs, FITC was utilized as the mock drug. A 5.3 μM solution in DMSO was prepared for drug delivery applications. Degradation analysis was conducted in 10 mM PBS buffer, pH 6.5 and 7.0, to mimic a biological environment. The GQDs-hMSNs were added to both buffers, vortexed at 1000 rpm for 3 h at 37 °C for 6 days, and sampled on the first, third, and sixth day. Solutions were analyzed by DLS and TEM to confirm particle degradation over time.

5.2.2. Instrumentation used for characterization and analysis of GQDs-hMSNs

A Hitachi 7500 transmission electron microscope (TEM) was used to image the GQDs-hMSNs. A Malvern model of Nano-ZS Zetasizer was used to measure size distribution and the zeta potential. UV-Vis absorption was analyzed by a Perkin Elmer Lambda 1050 UV-250 UV/Vis/NIR spectrophotometer and the fluorescence spectra was acquired by a Shimadzu RF-6000 spectrophotometer. IR spectra of hMSNs, GQDs, and GQDs-hMSNs were collected on a Thermo Fisher Scientific Nicolet iS5 Fourier transform infrared spectrometer (FT-IR). A Benchmark MultiThermal (Cool – Heat – Shake) H5000-H vortex system was used to integrate of GQDs into the hMSNs. A PHI Model 10-360 electron spectrometer with non-monochromatized Al Kα (1486.3 eV) X-rays was used for X-ray photoelectron spectroscopy (XPS). An Olympus FV3000 Laser Scanning Confocal Microscope was used for the *in vitro* cell imaging of the GQDs-

hMSNs with two channels being used for imaging: red (Fura-Red (Ca-free)) and green (Alexa 488).

5.2.3. Synthesis of GQDs-hMSNs

GQDs were synthesized as they were in previous experiments.[211] To summarize, 20 mg CBDA-2[170] was dissolved in 20 mL DI-water with the pH adjusted to 10.0 using NH_4OH to help CBDA-2 dissolve before autoclaving for 12 h at 200 °C. The resulting solution was then dialyzed for 12 h using a 100-500 Da membrane against DI-water.

hMSNs were synthesized first by mixing 24 mL of CTAC and 0.16 mL TEA into 40 mL of DI-water. CTAC and TEA were dissolved before 2.5 mL of solid silica suspension (prepared by the Stöber method) was added and transferred to a round bottom flask. Next, 20 mL of a 10 v/v% solution of TEOS in cyclohexane was added to the round bottom flask in an oil bath on reflux at 60 °C. After 12 h, 2.0 mL of 10 v/v% APTES in cyclohexane was added and the solution was stirred for another 3 h at 60 °C. Then, the heat was lowered to 50 °C and 120 mL of 0.2 M Na_2CO_3 was added and allowed to stir for 3 h. The flask was removed from the oil bath and the solution was centrifuged for 30 min at 12,000 rpm at 20 °C. The supernatant was discarded and the remaining solid was washed with 20 mL HCl/EtOH (1:10) solution three times. EtOH was added after the last washing step and placed back into a round bottom flask and heated in an oil bath until the EtOH reached a boil for 2-3 h. The final product of hMSNs was then dried completely to a solid for further use.

10 mg of hMSNs were added to 10 mL of DI-water and sonicated for 5 min to completely dissolve (1.0 mg/mL) and then filtered through a 0.1 μm syringe. Then, 1.0 mL of the filtered hMSNs was added to 1.0 mL of GQDs (0.2 mg/mL) and 3.0 mL of 20 mM HEPES buffer (pH 7.0) and mixed at 1000 rpm at 37 °C for 3 h before being dried at 60 °C to a solid.

5.2.4. Cell toxicity

1.0 mL of 5.3 µM FITC (2.06 µg) was added to 1.0 mg GQDs-hMSNs in 4.0 mL of 20 mM HEPES buffer (pH 7.0) and vortexed at 1000 rpm for 3 h at 37 °C. The solution was then centrifuged at 10,000 rpm to separate any FITC not absorbed by the GQDs-hMSNs. Then, the particles were resuspended in 20 mM HEPES buffer pH 7.0 for absorption spectroscopy to quantify how much FITC was absorbed. Compared to the control, on average, 75% of FITC added was absorbed by the GQDs-hMSNs (FITC labeled GQDs-hMSNs).

Cell viability of GQDs-hMSNs was tested with CyQUANT^{TM} LDH Cytotoxicity Assay kit. Briefly, the cells were plated into a 96-well plate overnight. A gradient concentration of GQDs-hMSNs (0, 1, 2, 5, 10, 20, 50, 100, and 200 µg/mL) was added into the wells. After 24 h incubation in a CO_2 incubator at 37 ºC, 10 µL of 10X Lysis buffer was added into 3 wells of 0 µg/mL group to serve as the maximum LDH controls. After 45 mins, 50 µL aliquots of all groups were transferred to a new 96-well plate, mixed with 50 µL of the Reaction Mixture solution. After 30 minutes incubation at room temperature protected from light, 50 µL of Stop Solution was added to the wells, and the absorbance read using an EXL800 microplate reader to quantify cell viability.

5.2.5. Cell imaging, PDT, and drug delivery

Cell imaging of GQDs-hMSNs or GQDs-hMSNs was investigated by adding 0, 100, and 200 µg/mL GQDs-hMSNs in to an 8-well slide chamber with cells inside. After a 4 h of incubation, the wells were rinsed with 1X PBS for 15 min 3 times, then fixed with 4% PFA for 15 min. After additional washes with PBS, TO-PRO-3 was added to stain the nuclei for 15 min. After washing with PBS, the chamber was removed and the slide was covered with a cover slide by mounting medium. When dry, the slides were imaged using an Olympus FV3000 Laser Scanning Confocal Microscope.

PDT analysis of GQDs-hMSNs was conducted using a LysoTracker Red lysosome kit and LDH assay. For cell viability assays, cells were seeded into a 96-well plate and incubated overnight. GQDs-hMSNs were then added in concentrations of 0, 1, 2, 5, 10, 20, 50, 100, and 200 μg/mL and incubated for 4 h before being washed with 1×PBS buffer. The cells were then subjected to 785 nm laser irradiation for 30 min at 11.81 mW/cm^2 and then incubated for another 24 h before analysis of the LDH assay kits. For confocal imaging, RAW 264.7 cells were seeded in an 8-well slide chamber and incubated overnight. After incubation with 200 μg/mL GQDs-hMSNs for 4 h, the cells were washed with 1×PBS buffer and after a 30 min incubation, fresh medium was added before for confocal imaging.

5.3. Results

5.3.1. Design of GQDs-hMSNs

The primary focus of this study is to derive nanoparticles from biomass that help support their biocompatibility and biodegradation. Using CBDA-2, a biomass-derived molecule, for synthesizing the GQDs yields synthetically green and environmentally friendly graphene-based particles. Additionally, with CBDA-2 being synthesized from agricultural waste provides the means to recycle waste products into potentially vital nanoparticles for cancer imaging and treatment. Furthermore, the nanoparticles need to be biodegradable as to avoid accumulation in the patient body that could eventually lead to toxicity. Stöber method-based silica nanoparticles have previously been shown to possess excellent biocompatibility[281-283] and, with their pH sensitivity, are prone to biodegradation[283-285] in a matter of days or weeks. These key features make them valuable to avoid host accumulation and toxicity over time as the human body will naturally break down the silica for use in biological pathways. Thus, GQDs were synthesized using CBDA-2.

To start, CTAC and TEA were mixed together before a Stöber silica suspension was spiked in. The solution was allowed to react before TEOS was added. After heating for 12 h on reflux at 60 °C, APTES was added to introduce amine functional groups to the particle surface to help in biocompatibility, low pH stability, and agglomeration, and the solution was allowed to react for another 3 h while stirring at 60 °C. This resulted in mesoporous silica nanoparticles (MSNs). Na_2CO_3 was added, and the solution was stirred for another 3 h at 50 °C before being washed with HCl/EtOH three times. EtOH was added to resuspend particles and allowed to boil for 2-3 h at 80 °C. These steps etched out the silica core of the MSNs to make hMSNs. Once the EtOH evaporated, the hMSNs were dried to a solid. 1.0 mg was dissolved in 1.0 mL of DI-water and 0.2 mg GQDs were added before the solution was diluted to 5.0 mL total volume with 20 mM HEPES pH 7.0 buffer. The solution was vortexed for 3 h at 1,000 rpm before being centrifuged and dried to purify the final product of GQDs-hMSNs (Schematic 5.1).

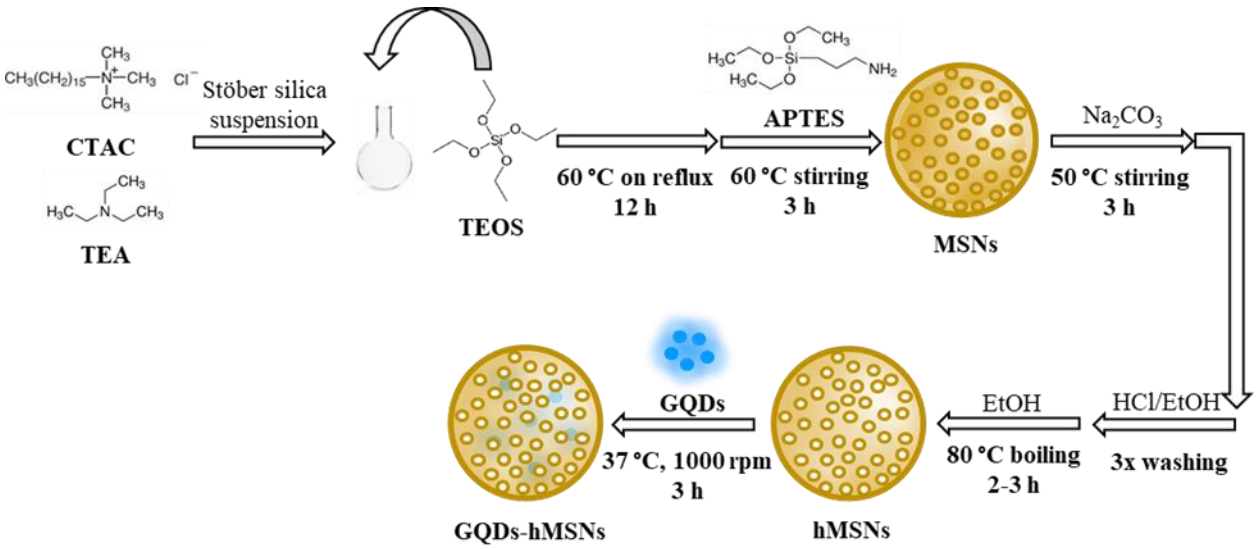

Schematic 5.1: CTAC, TEA, and Stöber silica suspension were mixed together, and the solution was heated in an oil bath on reflux for 12 h. APTES was then added and the solution was stirred for another 3 h before the particles were etched with Na_2CO_3 to make hMSNs. The particles were then washed with HCl/EtOH, suspended in EtOH and dried to a solid. GQDs were added later after the hMSNs were filtered and allowed to react for 3 h at 1000 rpm.

5.3.2. Characterization of GQDs-hMSNs

5.3.2.1. Size distribution and surface morphology

Particle size is essential to determine for nanoparticles as it is the determining factor as to whether or not they can be classified as nanoparticles. It is also important to determine particle size for biological applications as larger nanoparticles can struggle to diffuse across the cell membrane for imaging or drug delivery. Smaller particles tend to diffuse quicker and easier across the cell membrane; however, they are more common to cause cell toxicity.[286] Therefore, two different analyses were conducted to determine the size distribution of the GQDs-hMSNs. TEM images showed particles ranging from 20 – 50 nm (Figure 5.1A). The larger particles were more difficult to differentiate between single particles and smaller clusters. Thus, DLS was also used to determine particle size, averaging 47.0 ± 19.0 nm (Figure 5.1B).

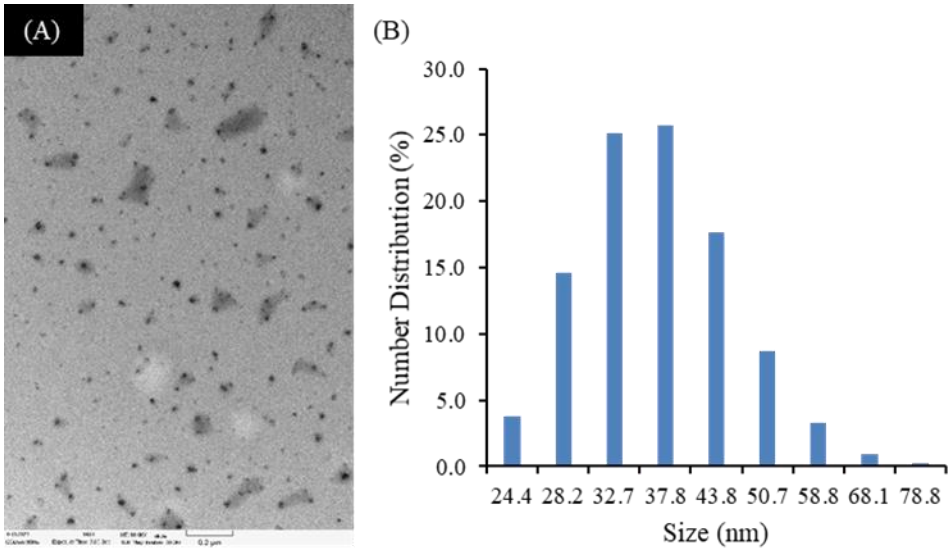

Figure 5.1: (A) TEM image of 80 µg/mL GQDs-hMSNs. (B) DLS of 32 µg/mL GQDs-hMSNs in DI-water after 5 min sonication.

Surface charge is also essential for nanoparticle determination as the charge will impact cellular uptake. Since uncharged particles are more difficult for cells to ingest, it is important to ensure and analyze the surface charge of the GQDs-hMSNs. Therefore, zeta potential measurements were taken at various pHs (1.0-11.0) and depict a decreasing potential from +5.71 to -21.8 mV (Figure 5.2). The most agglomeration and solution instability occurred in the more acidic pHs (1.0-5.0) but increased in stability from pH 7.0-11.0, indicating an overall negative surface charge. Lower agglomeration and greater solution stability in neutral pHs benefit biological applications. Additionally, higher agglomeration was observed for prolonged sonication times, greater than 30 min, and at concentrations higher than 50 µg/mL.

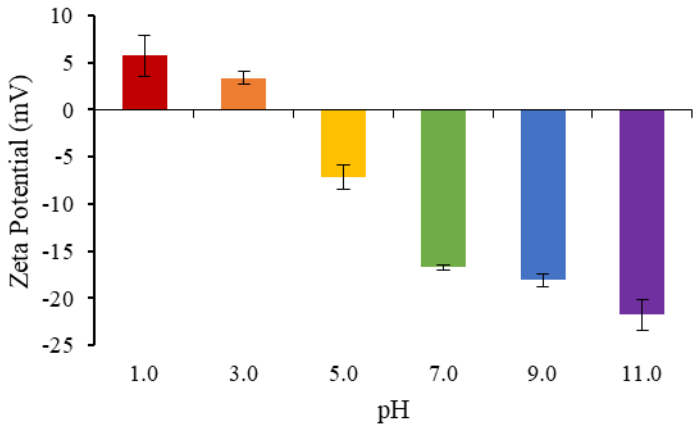

Figure 5.2: Zeta potential of GQDs-hMSNs (32 µg/mL) in various pHs (maleate 1.0, citrate 3.0-5.0, HEPES 7.0, CHES 9.0, and CAPS 11.0).

5.3.2.2. Functional group formation and elemental composition

Functional groups are essential for biological applications and additionally provide insight into the surface composition of the newly synthesized GQDs-hMSNs. FT-IR spectra were collected for hMSNs, GQDs, and GQDs-hMSNs to compare the differences of functional groups and additional bond formation after the synthesis of the nanoparticles and quantum dots together

(Figure 5.3). For hMSNs without additional GQDs, functional groups were determined to be Si-O-H stretching (3222 cm^{-1}, Figure 5.3A(a)), Si-O-Si bending (1058 cm^{-1}, Figure 5.3A(b)), Si-OH vibration (944 cm^{-1}, Figure 5.3A(c)), and Si-O vibration (796 cm^{-1}, Figure 5.3A(d)).[287-289] GQDs functional groups have been identified as -OH (3114 cm^{-1}, Figure 5.3B(e)), C=O (1668 cm^{-1}, Figure 5.3B(f)), and C-O/C-N (1384 cm^{-1}, Figure 5.3B (g)). The spectrum of GQDs-hMSNs contained both bonds found in hMSNs and GQDs, indicating the compilation of the two nanoparticle species, along with an additional C-H bond formation (2821 cm^{-1}, Figure 5.3C(h)). Furthermore, the -OH and C-O peaks are more distinct than what is observed in the GQDs spectrum, along with a decrease in C=O. This indicates the breaking of C=O bonds and the formation of Si-O-C bonds and potential C-Si bonds between the GQDs and hMSNs which signifies that the GQDs are chemically bonding to the surface of the hMSNs rather than being absorbed into the pores.[290,291] This is beneficial as the GQDs are less likely to escape the hMSNs before being delivered into the cancer cells for imaging and PDT treatment in addition to not interfering or interacting with the mock loading drug for delivery.

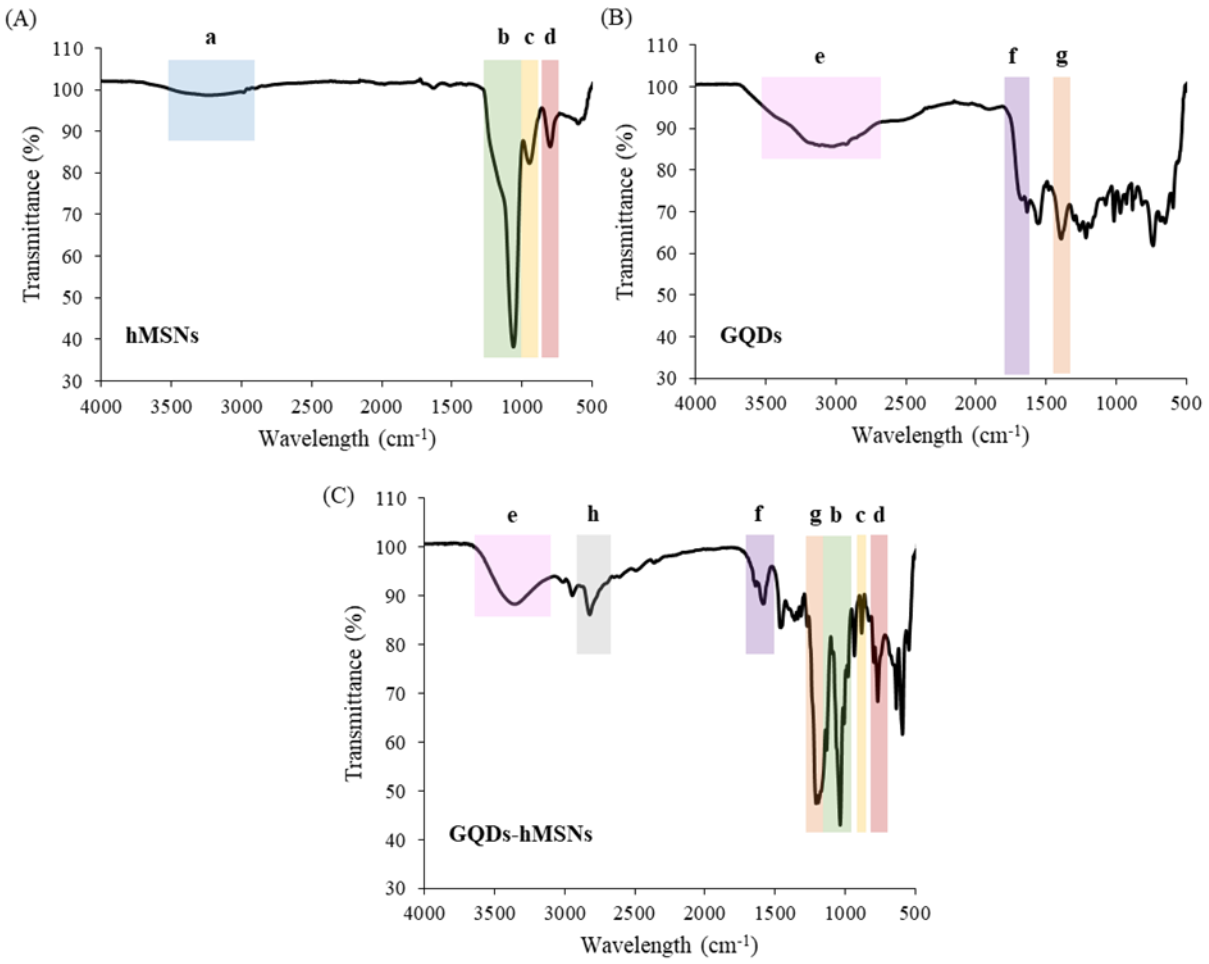

Figure 5.3: FT-IR spectra of hMSNs (A), GQDs (B), and GQDs-hMSNs (C). Peaks are attributed to (a, blue) Si-O-H stretching, (b, green) Si-O-Si bending, (c, yellow) Si-OH vibration, (d, red) Si-O vibration, (e, pink) -OH, (f, purple) C=O, (g, orange) C-O/C-N, and (h, gray) C-H.

XPS analysis was also conducted to confirm the elemental composition and bond formation of the GQDs-hMSNs seen in the FT-IR spectra and ensure that silicon, oxygen, and carbon were all present in the new synthesized particles. These three primary elements were identified in addition to the presence of nitrogen. This nitrogen content was attributed to APTES bonded to the hMSNs surface.[292] The elements of silicon and oxygen were attributed to be from the hMSNs, carbon and oxygen from the GQDs, and nitrogen from APTES. High-resolution scans of the

carbon, nitrogen, and silicon peaks of the GQDs-hMSNs showed C-O/C-N and C-C/C-Si bonds within the carbon peak (Figure 5.4A), NSi_2O and NSi_2O_x in the nitrogen peak (Figure 5.4B), and the silicon showed SiO and SiO_x bonds (Figure 5.4C). The presence of the C-Si bond supported the spectrum seen in FT-IR and confirmed the chemical binding of GQDs to the hMSNs surface, and further explained the slight peak shift in the excitation wavelength.

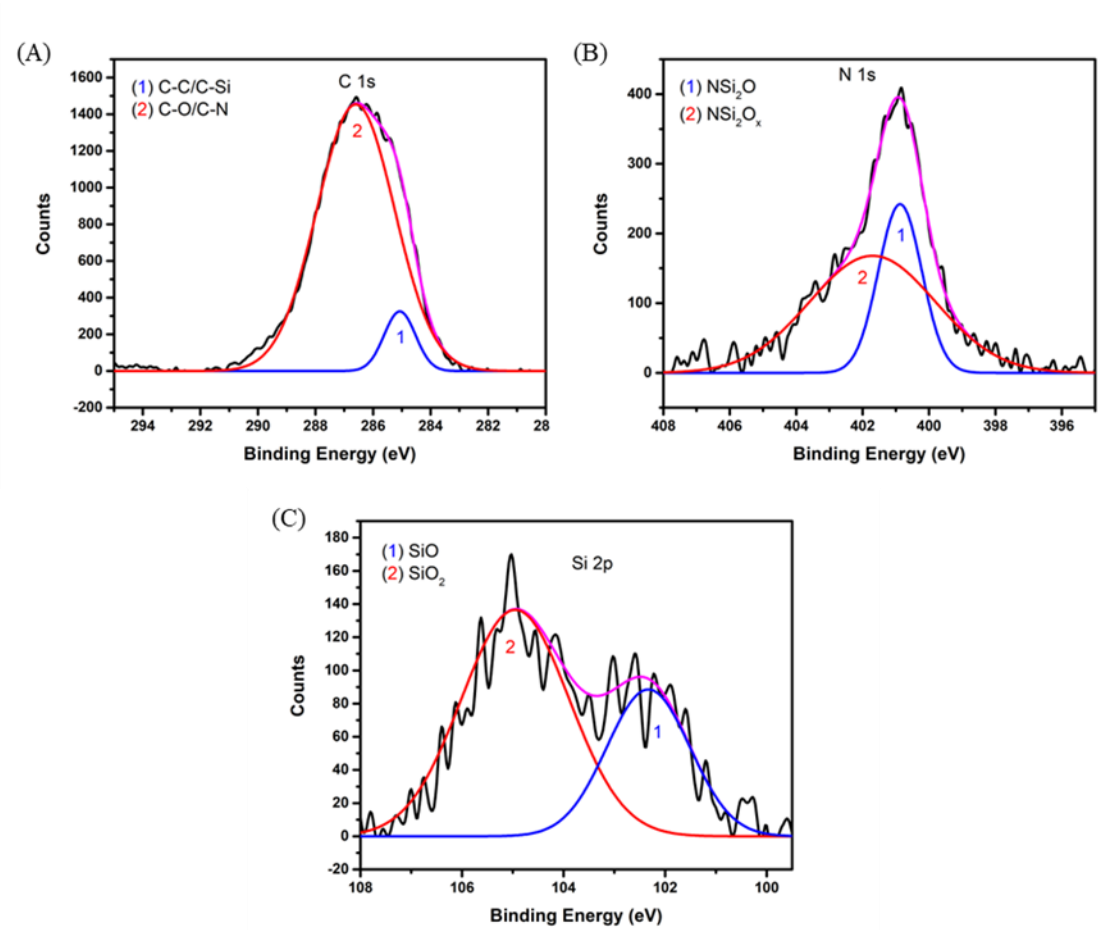

Figure 5.4: XPS high-resolution scans of (A) carbon, (B) nitrogen, and (C) silicon peaks in GQDs-hMSNs. The carbon peak shows C-O, C-Si, C-C, and C-N bonds. The nitrogen peak is primarily NSi_2O_x. Lastly, the silicon peak shows SiO_x bonds.

5.3.2.3. Optical properties and pH effects

Cell labeling for confocal microscopy imaging require fluorescent characteristics of nanoparticles in order to be applicable. Thus, the absorption, excitation and emission spectra were collected of the GQDs-hMSNs. The absorbance of 300 nm, excitation of 310 nm, and emission of 440 nm for the GQDs were previously analyzed in another study.[211] However, after conversion with hMSNs, the new GQDs-hMSNs spectral features slightly shifted, with an absorbance at 310 nm (Figure 5.5A) and an excitation peak at 330 nm (Figure 5.5B) due to chemical binding on the silica surface. The emission peak at 440 nm remained the same (Figure 5B). Additionally, the GQDs-hMSNs showed concentration dependence (Figure 5.5C) as the GQDs have shown previously. However, the radiation dependency and red-shifting of the emission peak with increasing excitation (270 – 370 nm) did not occur as analyzed before (Figure 5.5D), and thus the GQDs now displayed rapid internal conversion from higher initial excited states to lower states that prevented the red-shift since being attached to hMSNs.

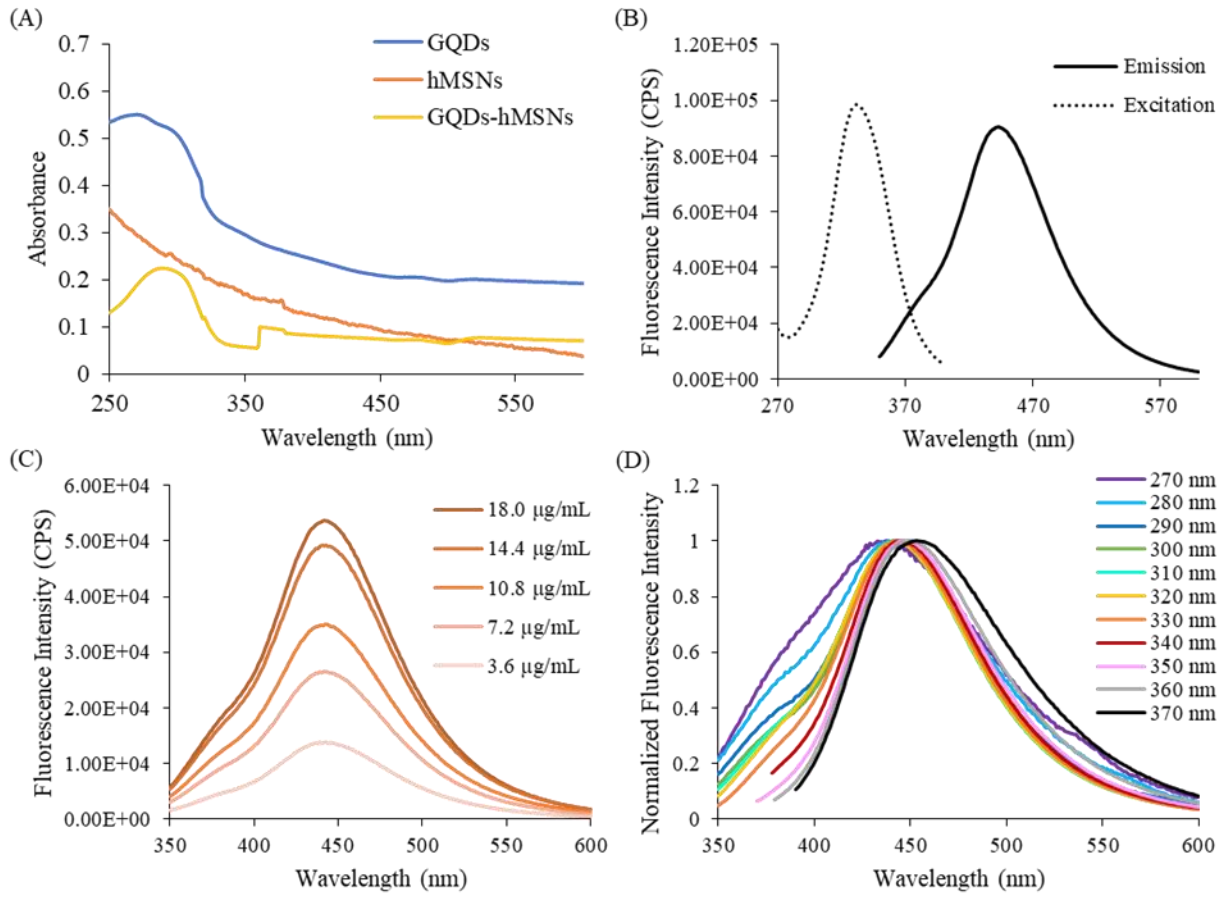

Figure 5.5: (A) Absorption spectra of GQDs (100 µg/mL), hMSNs (10 µg/mL), and GQDs-hMSNs (10.8 µg/mL). (B) Excitation and emission spectrum of GQDs-hMSNs (10.8 µg/mL). (C) Concentration dependency pattern of GQDs-hMSNs. (D) Changing excitation light showing no red-shift of the emission peak (18 µg/mL).

The human body contains a range of pHs, so the GQDs-hMSNs are required to show fluorescence stability across different pHs and avoid quenching to optimize *in vitro* cell imaging. Therefore, the GQDs-hMSNs fluorescence was analyzed at pHs 1.0 – 11.0 for any quenching tendencies. For pHs 5.0 – 9.0, the GQDs-hMSNs retained their fluorescence, and were only slightly quenched at pH 11.0. Furthermore, pHs 1.0 and 3.0 showed greater quenching, with pH 1.0 nearly losing fluorescence altogether (Figure 5.6). However, this is typical of GQDs as

extremely acidic conditions lead to agglomeration and solution instability, as seen in the zeta potential analysis (section 5.3.2.1). Nonetheless, the highest fluorescence observed in the neutral pHs was encouraging for cell labeling applications as the fluorescence will be maintained in the biological pHs.

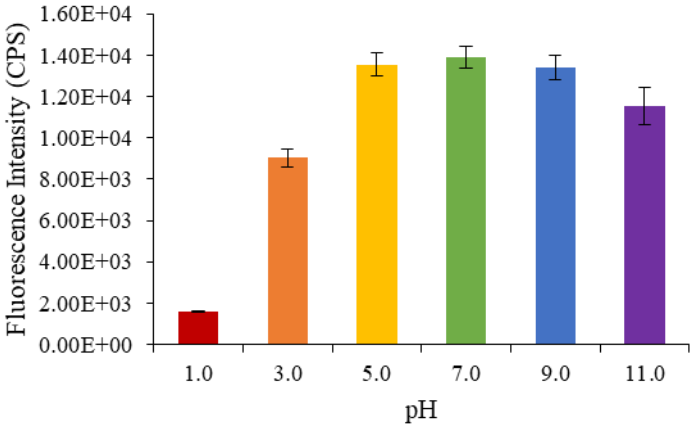

Figure 5.6: GQDs-hMSNs with changing pH (maleate pH 1.0, citrate 3.0-5.0, HEPES 7.0, CHES 9.0, CAPS 11.0) of the GQDs-hMSNs (36 µg/mL). The same trend was observed for GQDs, where quantum dots quench in pH 1.0 but remain steady in the neutral pHs.

5.3.3. GQDs-hMSNs biodegredation

A goal of this project is to lessen immune system taxation via traditional cancer treatments and therefore it is important to ensure that the GQDs-hMSNs are not retained long-term in the patient body and are broken down after a couple of weeks or at least after they have fulfilled their purpose for drug delivery and PS agent for PDT treatment. Solutions of 10 mM PBS buffer, pH 7.0 and 6.5, and 10 mM citrate buffer pH 5.0 and 4.0, were used to analyze the biodegradation of the GQDs-hMSNs to mimic biological systems. The GQDs-hMSNs were added to the buffer pHs (0.2 mg/mL) and vortexed for 6 days at 37 °C, 1000 rpm. Samples were taken every 24 h and analyzed via DLS and TEM to observe particle degradation over time.

DLS of pH 4.0 revealed particle agglomeration after the first 24 h in the buffer (Figure 5.7A). The TEM image of day 1 depicts large, swollen particles with some already rupturing under the acidic conditions (Figure 5.7B). For day 3, the particles were approximately the same size as on day 1, as observed in the DLS. However more debris particles emerged in lower quantities (Figure 5.7C). Lastly, day 6 TEM depicted a large increase in debris particles along with breakage and misshaped larger particles as they continued to degrade (Figure 5.7D). For pH 5.0, a similar trend was observed for the first day, with increased particle agglomeration observed in the DLS (Figure 5.7E). Under TEM, day 1 GQDs-hMSNs at pH 5.0 depicted the same enlarged particles. However, they appeared to aggregate together instead of swelling like at pH 4.0 (Figure 5.7F). By day 3, the particles at pH 5.0 TEM (Figure 5.7G) were similar to day 3 particles at pH 4.0 while the DLS also confirmed the slight degradation of the particles although they were degrading more slowly. Day 6 TEM (Figure 5.7H) showed rupturing particles that clumped together to yield larger size distributions observed in DLS.

PBS buffers showed slightly different particle formations. For pH 6.5, the particles immediately aggregated and swelled after one day, as observed in DLS and TEM (Figure 5.7I and 5.7J). However, the swelling was more severe than in the more acidic buffers. Day 3 TEM images showed a small decrease in particle size (Figure 5.7K), with less swollen particles and the appearance of smaller degradation debris particles. Day 6 TEM (Figure 5.7L) showed even more debris particles, as seen in the DLS.

In comparison, pH 7.0 showed a similar trend as the 6.5 pH. After day 1, the DLS results (Figure 5.7M) showed the same particle size distribution as observed previously (section 5.3.2.1). However, the TEM images for day 1 (Figure 5.7N) showed burst or rippled particles, indicating that even after a short period of time, the particles started to degrade and lose their surface integrity.

Day 3 for pH 7.0 (Figure 5.7O) showed increased particle agglomeration and swelling with smaller debris particles, much like pH 6.5 on day 6. Lastly, for day 6 at pH 7.0, there was an increase in debris particles with some swollen and agglomerated particles (Figure 5.7P).

Therefore, the GQDs-hMSNs have a prolonged degradation at pH 7.0 compared to 4.0. Thus, they will function longer at a natural, healthy pH, allowing the particles more time to accumulate in cancerous cells without releasing the chemotherapy drug or GQDs. Furthermore, as observed in the zeta potential measurements (section 5.3.2.1) the GQDs-hMSNs show agglomeration and solution instability in acidic pHs. This will contribute to the increased agglomeration seen at pH 5.0 and 4.0 after one day of exposure. From there, the particles degraded faster at pH 4.0 based on the particle size in TEM. However, retained agglomeration at pH 5.0 for day 6 yielded a larger particle size in DLS than what was observed in TEM. Furthermore, pH 7.0 and 6.5 showed less severe particle agglomeration after one day, as expected due to the zeta potential measurements previously discussed. Nonetheless, the slightly more acidic pH of 6.5 showed larger particle size and agglomeration, initially, compared to pH 7.0 and showed a faster rate of degradation. Therefore, the GQDs-hMSNs will most likely degrade faster in cancerous environments that are more acidic, releasing the chemotherapy drug and GQDs into the cancer cells for treatment and imaging.

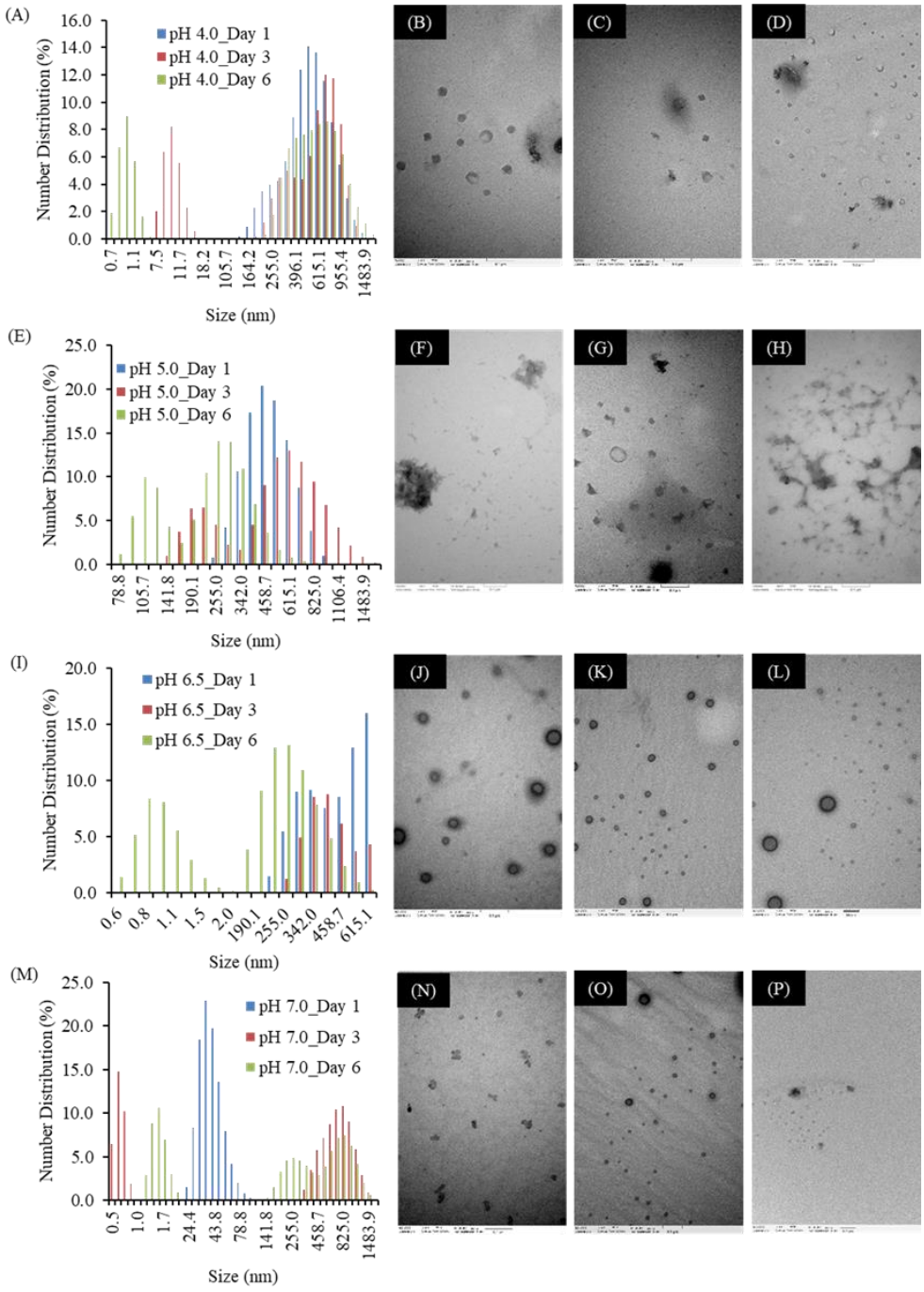

Figure 5.7: (A) DLS of 32 µg/mL GQDs-hMSNs particle degradation in pH 4.0 for 6 days. TEM images of particles in pH 4.0 after (B) day 1, (C) day 3, and (D) day 6. (E) DLS of 32 µg/mL GQDs-hMSNs particle degradation in pH 5.0 for 6 days. TEM images of particles in pH 5.0 after (F) day 1, (G) day 3, and (H) day 6. (I) DLS of 32 µg/mL GQDs-hMSNs particle degradation in pH 6.5 for 6 days. TEM images of particles in pH 6.5 after (J) day 1, (K) day 3, and (L) day 6. (M) DLS of 32 µg/mL GQDs-hMSNs particle degradation in pH 7.0 for 6 days. TEM images of particles in pH 7.0 after (N) day 1, (O) day 3, and (P) day 6.

5.3.4. Cell viability, in vitro cell imaging, PDT treatment, and mock drug delivery of GQDs-hMSNs

In order to determine the biocompatibility of the GQDs-hMSNs, cytotoxicity tests were also analyzed using LDH assays. Effects of GQDs-hMSNs on cell viability were tested using RAW 264.7 cells, incubating the cells for 24 h with different concentrations of GQDs-hMSNs. Thermos Fisher CyQUANT™ LDH Cytotoxicity Assay Kit was performed to measure cell viability. The cells showed no signs of toxicity up to 100 μg/mL. However, at 200 μg/mL the cell counts decreased to 70 - 60% of the original amount (Figure 5.8). This is attributed to the hMSNs as the GQDs showed no cytotoxicity up to 200 μg/mL in previous studies.[211]

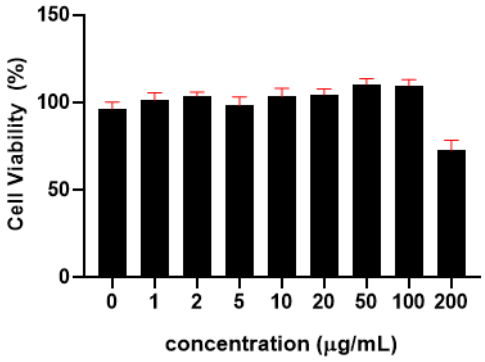

Figure 5.8: LDH assay cytotoxicity analysis of GQDs-hMSNs up to 200 μg/mL in RAW 264.7 cells.

Furthermore, to determine GQDs-hMSNs applicability in cell imaging, *in vitro* confocal microscopy images were collected using RAW 264.7 cells. The cells were incubated for 4 h with 100 and 200 μg/mL GQDs-hMSNs (Figure 5.9A). Additionally, TO-PRO-3 dye was used to label the cell nucleus. Upon imaging, weak fluorescence signal was found using the 488 nm laser for the GQDs-hMSNs (Figure 5.9B). This is due to the 488 nm laser being just outside the GQDs

optimal excitation wavelength. However, the concentration of GQDs added in the synthesis can be increased to bind more GQDs to the surface of the hMSNs to provide a stronger fluorescent signal in the cells.

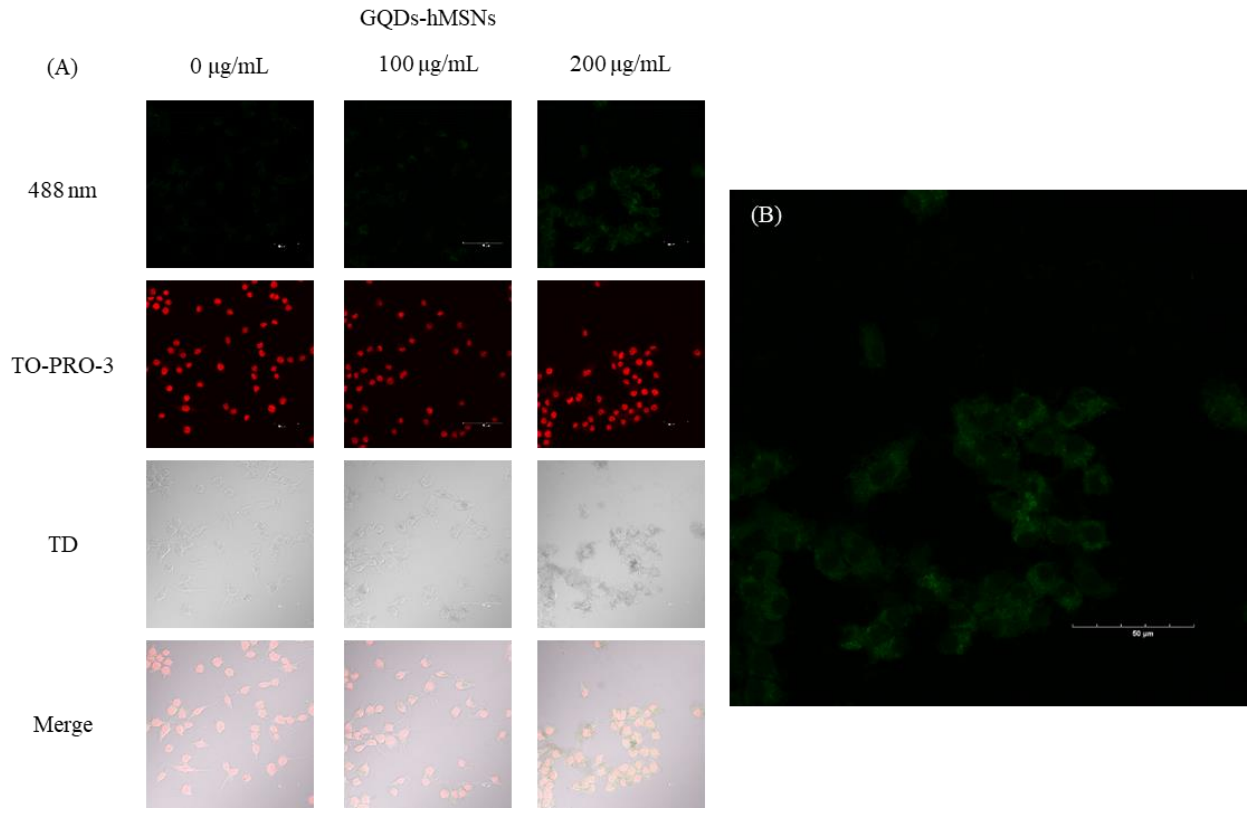

Figure 5.9: *In vitro* images of RAW 264.7 cells with GQDs-hMSNs. (A) 0, 100, and 200 µg/mL cell cultures with TO-PRO-3 labeled nucleus. (B) 200 µg/mL GQDs-hMSNs using the 488 nm laser showed a weak fluorescence signal. Transmitted (T) and merged images depict the cell integration of GQDs-hMSNs in the cytoplasm.

The GQDs-hMSNs were also examined for their use in PDT treatment of RAW 264.7 cells using LysoTracker Red in confocal microscopy and LDH assay for cytotoxicity analysis. A concentration range of 0 - 200 µg/mL GQDs-hMSNs was tested and after 30 min of laser irradiation at 11.81 mW/cm^2, the cells were incubated for another 24 h. The cytotoxicity showed a linear decrease in cell viability with increasing concentrations of GQDs-hMSNs until 20 µg/mL,

signifying that the GQDs-hMSNs were generating $^1O_2$ and induced toxicity in the RAW 264.7 cells (Figure 5.10A). Concentrations higher than 20 μg/mL decreased cell viability compared to the control, however, the decrease was similar to the 20 μg/mL concentration. This decrease in $^1O_2$ generation is attributed to the induced toxicity of the hMSNs observed in the cytotoxicity analysis previously discussed. The cells are subjected to a greater toxicity due to the presence of hMSNs before the GQDs could generate $^1O_2$. Thus, fewer viable cells would be available for PDT treatment and display a decrease in effective PDT treatment, but not necessarily due to a lack of $^1O_2$ generation. Additionally, LysoTracker Red was used to track the ROS generation within the RAW 264.7 cells. Confocal microscope images were taken using the 488 nm laser (Figure 5.10B) for GQDs-hMSNs and the 561 nm laser (Figure 5.10C) for LysoTracker Red. The TD (Figure 5.10D) and merged (Figure 5.10E) images showed that the GQDs-hMSNs and LysoTracker Red are in the RAW 264.7 cells' cytoplasm. This signifies that the ROS generation comes from the incubated GQDs-hMSNs, which are the main contributor to the cells' decrease in viability.

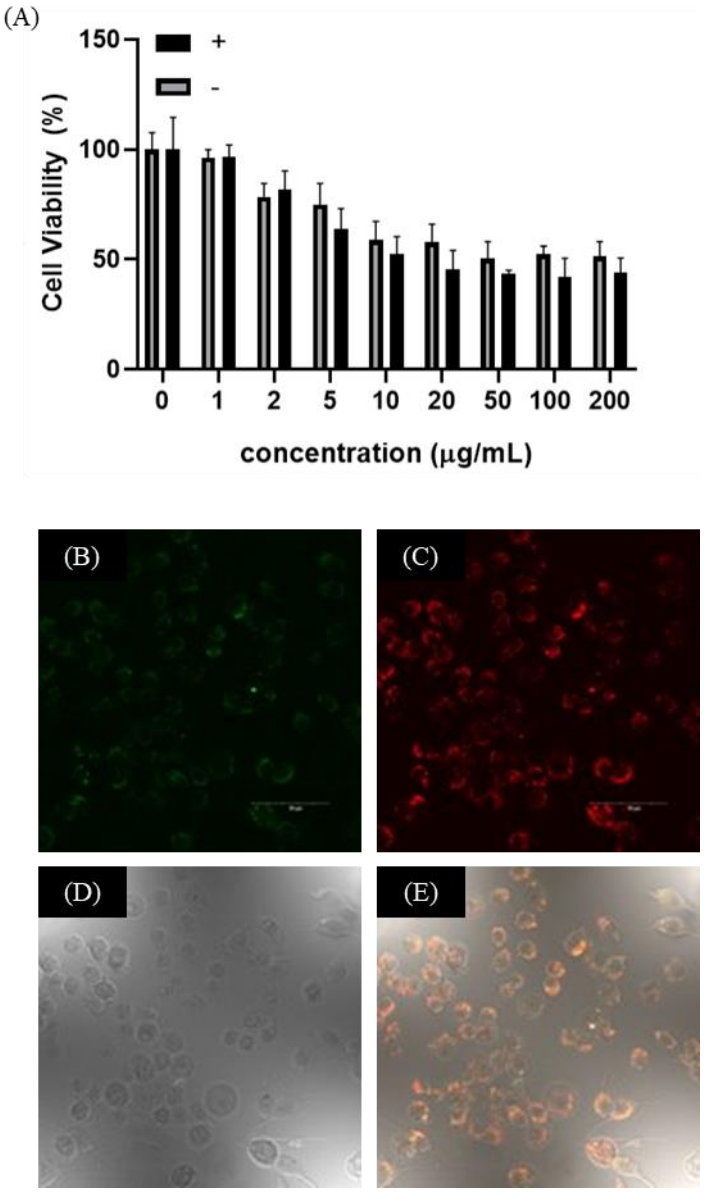

Figure 5.10: PDT treatment of RAW 264.7 cells with GQDs-hMSNs. (A) LDH assay cytotoxicity analysis after 24 h treatment at different concentrations (0 - 200 μg/mL); (+), 785 nm laser irradiation; (-), no laser irradiation. Confocal microscope images of LysoTracker Red with 200 μg/mL GQDs-hMSNs (B) 488 nm laser, (C) 561 nm laser, (D) TD, and (E) merged.

Drug delivery via GQDs-hMSNs using FITC dye as a mock drug was also analyzed by confocal microscopy. Concentrations of 0, 50, 100, and 200 μg/mL FITC labeled GQDs-hMSNs were cultured with RAW 264.7 cells for 4 h. The results showed an increasing fluorescence signal

with increasing concentration of FITC labeled GQDs-hMSNs (Figure 5.11A), confirming that FITC is being delivered by the GQDs-hMSNs. Lower concentrations, such as 100 µg/mL of the FITC labeled GQDs-hMSNs still adequately delivered the mock drug and yielded exceptional cell images (Figure 5.11B).

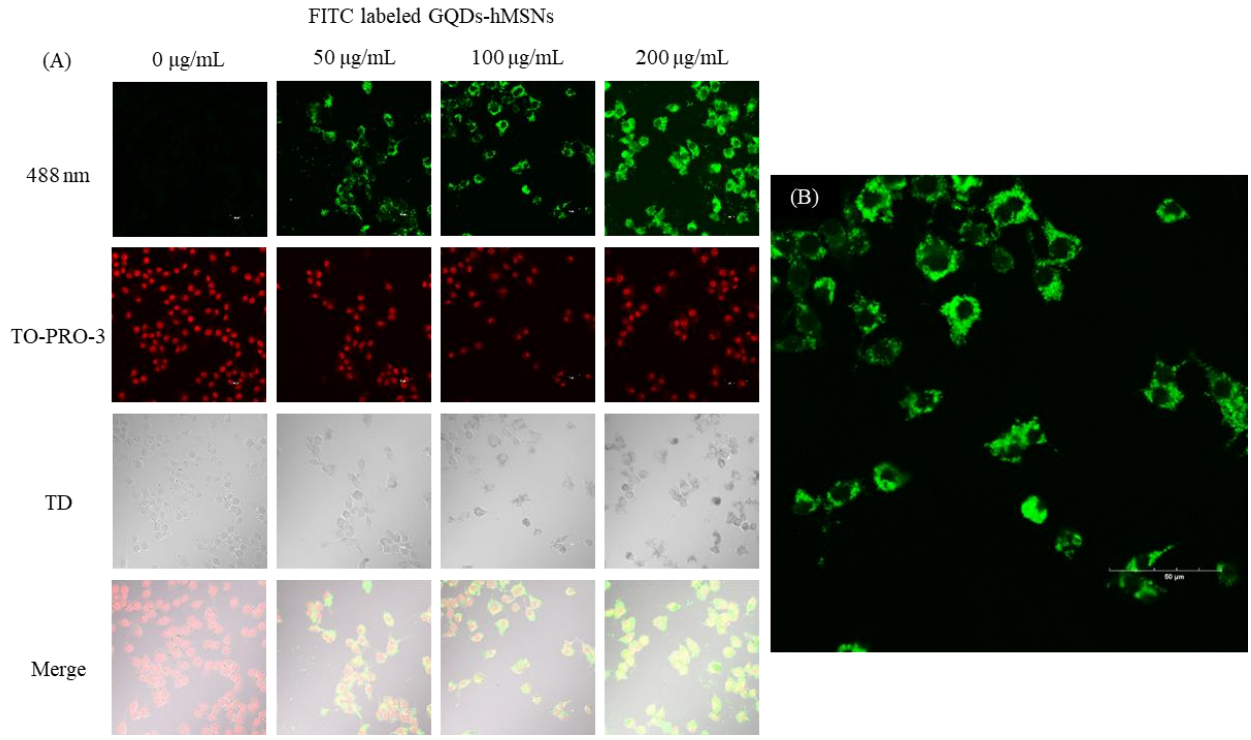

Figure 5.11: *In vitro* images of RAW 264.7 cells with GQDs-hMSNs doped with FITC dye as the mock drug. (A) 0, 50, 100, and 200 µg/mL cell cultures with TO-PRO-3 labeled nucleus. (B) 100 µg/mL GQDs-hMSNs with FITC.

5.4. Conclusions

hMSNs were successfully synthesized using the Stöber method that allowed GQDs to be incorporated onto their surface to form GQDs-hMSNs for cell imaging and dual cancer treatment. DLS and TEM confirmed the presence of particles in the size range of 47.0 ± 19 nm. DLS and TEM were also used to confirm particle degradation in pH 7.0 and 6.5 after being vortexed for 6 days at 1000 rpm, 37 °C. Samples were taken on the days 1, 3, and 6 and examined by DLS and

TEM. After 6 days, it was observed that the GQDs-hMSNs in pH 7.0 degrade at a slower rate compared to pH 6.5, indicating that the particles would degrade faster in cancer cells and would not linger in the patient to induce toxic effects. Additionally, the fluorescence characteristics of the GQDs was maintained with only a slight shift observed in the excitation spectrum compared to GQDs without hMSNs. The fluorescence patterns of the GQDs-hMSNs were comparable to GQDs, showing pH sensitivity in acidic conditions, zeta potential measurements showed particle agglomeration in pH 3.0-1.0, and concentration dependency. However, red-shifting on the GQDs was not observed in the GQDs-hMSNs, a strong indication of chemical binding on the silica particle surface to prolong stability of the GQDs. Furthermore, FT-IR confirmed the functional group difference between GQDs, hMSNs, and GQDs-hMSNs. An increase in the C-O band and a decrease in the -OH band found in GQDs-hMSNs compared to GQDs indicates the GQDs binding to the hMSNs through oxygen bands, as the hMSNs containing both Si-OH and Si-O showed a decrease in Si-OH in GQDs-hMSNs but a preservation of Si-O. XPS also yield an elemental spectrum of GQDs-hMSNs that shows bond formation between GQDs and hMSNs, along with the elements of C, O, and Si being present, in addition to N from APTES.

The GQDs-hMSNs showed slight cytotoxic effects at 200 μg/mL, attributed to the hMSNs. However, the GQDs-hMSNs were successful absorbed by RAW 264.7 cells after 4 h of incubation to yield fluorescent *in vitro* images via confocal microscopy. Furthermore, RAW 264.7 cells were successfully imaged using the GQDs-hMSNs via confocal microscopy. However, higher concentrations were needed as the 488 nm laser was out of range for optimal excitation of the GQDs-hMSNs. Nonetheless, the hMSNs have shown great adaptability to the GQDs, and thus a higher concentration of GQDs can be added during the synthesis to increase their concentration for cell imaging without increasing the concentration of hMSNs to reduce toxicity. PDT treatment

was also successful using the GQDs-hMSNs, showing induced toxicity with increasing concentration as more $^1O_2$ was generated. Additionally, the hMSNs also displayed excellent drug loading and releasing characteristics, utilizing FITC dye as the mock drug. RAW cells were incubated with the GQDs-hMSNs doped with FITC, and the resulting confocal images displayed excellent delivery of FITC into the cells.

CHAPTER VI

CONCLUSIONS

Using the bottom-up approach allows the particles to be synthesized to be quite small. Using DLS, TEM, and HRTEM, the GQDs and PGQDs were both confirmed to be within the QD size range with an average size of 6.50 ± 3.5 nm and 7.95 ± 7.1 nm, respectively. Furthermore, the Stöber for hMSNs typically produces particles that are on average 50 nm in size. The hMSNs synthesized in this dissertation were close to that size, being 47 ± 19 nm. Zeta potential measurements were predicted to show particle stability in neutral and basic pHs for the GQDs as the oxygen groups will provide stability in basic conditions. This was observed for the GQDs, the oxygen groups were not able to withstand increasing positive charge in acid pHs, thus resulted in particle agglomeration and a decrease in potential. In comparison, the PGQDs were showed to have a greater stability in acidic pHs due to the presence of nitrogen in the porphyrin ring. hMSNs showed similar trends to the GQDs as they also formed negative charges due to oxygen presence in SiO_2.

Given the use of biomass-derived material to synthesize the GQDs, the main elemental composition primarily was carbon with some oxygen due to its presence in biomass material, CBDA-2. For PGQDs, TCPP contains additional nitrogen in the central ring and therefore it was still be present after synthesis. This elemental makeup was confirmed using XPS. Further chemical bonds were analyzed using FT-IR. Bonds of C-O, C=O, and -OH were confirmed in the spectra of GQDs and PGQDs, with added C=N in PGQDs. Additionally, silica bonds were identified in hMSNs, primarily in the form Si-O-Si and Si-OH. The element of silicon was also observed in XPS. Lastly, the graphene lattice appeared at 20° in XRD spectra for the GQDs and PGQDs,

confirming that the particles are comprised of a lattice that yields increased particle stability for fluorescence imaging and prolonged light exposure for photostability.

For the optical properties of GQDs and PGQDs, the GQDs contained the common blue-green emission light at 440 nm with an excitation light of 310 nm. However, the GQDs also contained a rare NIR peak at 850 nm. The PGQDs were red-emissive with a peak at 650 nm at an excitation of 420 nm. Some quenching effects were observed in pHs lower than 3.0 for the GQDs while the PGQDs showed less severe quenching in the acidic environments due to the presence of nitrogen. hMSNs were not expected to have any fluorescence characteristics and when examined they indeed did not display any fluorescence properties.

Using MTT and LDH assays, the GQDs and PGQDs showed little to no toxic effects on RAW 264.7 and MCF-7 cells up to 200 µg/mL. This low toxicity was attributed to their chemical composition being that of biomass-derived material and natural pigments allowing for improved symbiosis interactions. Additionally, their smaller particle size allowed them to pass through the cell membranes and be incorporated into the cell cytoplasm for confocal imaging. MCF-7 cells were used for the GQDs and HeLa cells were used for the PGQDs for the *in vitro* confocal microscopy imaging. Both cell lines were successful in incorporating the particles into the cytoplasm and were clearly imaged without any leaching out of the cells.

For GQDs-hMSNs, a slight increase in toxicity was observed in the 200 µg/mL concentration in RAW 264.7 cells. This is attributed to the hMSNs rather than the GQDs due to the low toxicity GQDs previously observed. They were also successfully imaged in RAW 264.7 cells using confocal microscopy, although there was a decrease in fluorescence compared to GQDs. However, utilizing FITC dye, the GQDs-hMSNs were successfully loaded with the mock drug and delivered it into the RAW 264.7 cells. Additionally, using the lysosome kits, ROS

compounds were successfully tracked within the cells for PDT treatment and imaged using confocal microscopy. LDH assays also indicated induced toxicity of the GQDs-hMSNs after laser irradiation produced $^1O_2$ which induced toxicity in the cells.

REFERENCES

1. Khan, I.; Saeed, K.; and Khan, I. Nanoparticles: properties, applications and toxicities. *Arab. J. Chem.* **2019**, *12*, 908.
2. Bayda, S.; Adeel, M.; Tuccinardi, T.; Cordani, M.; and Rizzolio, F. The history of nanoscience and nanotechnology: from chemical-physical applications of nanomedicine. *Molecules.* **2020**, *25(1)*, 112.
3. McSweeney, P. The safety of nanoparticles in sunscreens: an update for general practice. *Aust. Fam. Physician.* **2016**, *45(6)*, 397.
4. Paramsothy, M. Nanotechnology in clothing and fabrics. *Nanomater.* **2022**, *12(1)*, 67.
5. Singh, T.; Shukla, S.; Kumar, P.; Wahla, V.; Bajpai, V.; and Rather, I. Application of nanotechnology in food science: perception and overview. *Front. Microbiol.* **2017**, *8*, 1501.
6. Shepard, Z.; and Oyanedel-Craver, V. A review of the impact of testing conditions on the performance and quality control of locally manufactured, point-of-use ceramic water filters. *Environ. Sci.: Water Res. Technol.* **2022**, *8*, 510.
7. World Health Organization (WHO), https://www.who.int/news-room/fact-sheets/detail/cancer#:~:text=Cancer%20is%20a%20leading%20cause,and%20rectum%20and%20prostate%20cancers, accessed 1 May 2022.
8. Mayo Clinic, https://www.mayoclinic.org/tests-procedures/cancer-treatment/in-depth/cancer-treatment/art-20047246, accessed 1 May 2022.
9. Wang, C.; Taki, M.; Sato, Y.; and Yamaguchi, S. A photostable fluorescent marker for the superresolution live imaging of the dynamic structure of the mitochondrial cristae. *Biol. Sci.* **2019**, *116(32)*, 15817.

10. Ojo, O.; Olayide, I.; Akalabu, M.; Ajiboye, B.; Ojo, A.; Oyinloye, B.; and Ramalingam, M. Nanoparticles and their biomedical applications. *Biointer. Res. Appl. Chem.* **2020**, *11*, 8431.
11. Sigma Aldrich, https://www.sigmaaldrich.com/US/en/technical-documents/technical-article/materials-science-and-engineering/biosensors-and-imaging/quantum-dots, accessed 1 May 2022.
12. de Oliveira, P.; Torresi, R.; Emmerling, F.; and Camargo, P. Challenges and opportunities in the bottom-up mechanochemical synthesis of noble metal nanoparticles. *J. Mater. Chem. A.* **2020**, *8*, 16114.
13. Teng, Z.; Wei, L.; Tang, Y.; Elzatahry, A.; Lu, G.; and Zhao, D. Mesoporous organosilica hollow nanoparticles: synthesis and applications. *Adv. Mater.* **2019**, *31*, 1707612.
14. Sengul, A.; and Asmatulu, E. Toxicity of metal and metal oxide nanoparticles: a review. *Environ. Chem. Lett.* **2020**, *18*, 1659.
15. Meng, W.; Bai, X.; Wang, B.; Liu, Z.; Lu, S.; and Yang, B. Biomass-derived carbon dots and their applications. *Energy Environ. Mater.* **2019**, *2*, 172.
16. Lee, J.; Youn, Y.; Kwon, I.; and Ko, N. Recent advances in quantum dots for biomedical applications. *J. Pharm. Investig.* **2018**, *48*, 209.
17. Tabish, T.; Scotton, C.; Ferguson, D.; Lin, L.; van der Veen, A.; Lowry, S.; Ali, M.; Jabeen, F.; Ali, M.; Winyard, P.; and Zhang, S. Biocompatibility and toxicity of graphene quantum dots for potential application in photodynamic therapy. *Nanomedicine (Lond).* **2018**, *13*, 1923.

18. Singh, U.; Teja, A.; Walia, S.; Vaswani, P.; Dalvi, S.; and Bhatia, D. Water stable, red emitting, carbon nanoparticles stimulate 3D cell invasion via clathrin-mediated endocytic uptake. *Nanoscale Adv.* **2022**, *4*, 1375.
19. Ghimire, P.; and Jaroniec, M. Renaissance of Stöber method for synthesis of colloidal particles: new developments and opportunities. *J. Colloid Interf. Sci.* **2021**, *584*, 838.
20. Fernandes, R.; Raimundo Jr., I.; and Pimentel, M. Revising the synthesis of Stöber silica nanoparticles: a multivariate assessment study on the effects of reaction parameters on the particle size. *Colloid Surf. A. Physicochem. Eng. Asp.* **2019**, *577*, 1.
21. Zhang, M.; Yang, J.; Cai, Z.; Feng, Y.; Wang, Y.; Zhang, D.; and Pan, X. Detection of engineered nanoparticles in aquatic environments: current status and challenges in enrichment, separation, and analysis. *Environ. Sci.: Nano.* **2019**, *6*, 709.
22. Garbovskiy, Y. Biological contamination of nanoparticles and its manifestation in optical absorbance measurements. *Anal. Chem.* **2017**, *89*, 7282.
23. Wilson, N. Nanoparticles: environmental problems or problem solvers? *BioScience.* **2018**, *68*, 241.
24. Huang, H.; Lee, Y.; Hsu, Y.; Liao, C.; Lin, Y.; and Chiu, H. current strategies in assessment of nanotoxicity: alternatives to in vivo animal testing. *Int. J. Mol. Sci.* **20121**, *22(8)*, 4216.
25. National Nanotechnology Initiative, https://www.nano.gov/you/nanotechnology-benefits, accessed 2 February 2020.
26. Lowry, G.; Gregory, K.; Apte, S.; and Lead, J. Transformations of nanomaterials in the environment. *Environ. Sci. Technol.* **2012**, *46*, 6893-6899.
27. Nanobiomedical Centre, http://cnbm.amu.edu.pl/en/nanomaterials, accessed 2 February 2020.

28. Gupta, R.; and Xie, H. Nanoparticles in daily life: applications, toxicity, and regulations. *J. Environ. Pathol. Toxicol. Oncol.* **2018**, *37(3)*, 209-230.
29. Lehman, S.; Morris, A.; Mueller, P.; Salem, A.; Grassian, V.; and Larsen, S. Silica nanoparticle-generated ROS as a predictor of cellular toxicity: mechanistic insights and safety by design. *Environ. Sci.: Nano.* **2016**, *3*, 56-66.
30. Mugica, I.; Fito, C.; Domat, M.; Dohányosová, P.; Gutierrez-Cañas, C.; and López-Videl, S. Novel techniques for detection and characterization of nanomaterials based on aerosol science supporting environmental applications. *Sci. Total Environ.* **2017**, *609*, 348-359.
31. Qiu, T.; Clement, P.; and Haynes, C. Linking nanomaterial properties to biological outcomes: analytical chemistry challenges in nanotoxicology for the next decade. *Chem. Commun.* **2018**, *54*, 12787.
32. Pietroiusti, A.; Stockmann-Juvala, H.; Lacaroni, F.; and Savolainen, K. Nanomaterial exposure, toxicity, and impact on human health. *WIREs Nanomed Nanobiotechnol.* **2018**, *10(5)*, 1513.
33. Ganguly, P.; Breen, A.; and Pillai, S. Toxicity of nanomaterials: exposure, pathways, assessment, and recent advances. *ACS Biomater Sci Eng.* **2018**, *4*, 2237.
34. Jahan, S.; Yusoff, I.; Alias, Y.; and Bakar, A. Reviews of the toxicity behavior of five potential engineered nanomaterials (ENMs) into the aquatic ecosystem. *Toxicol Rep.* **2017**, *4*, 211.
35. Saleh, T. Trends in the sample preparation and analysis of nanomaterials as environmental contaminants. *Trends Environ. Anal. Chem.* **2020**, *28*, e00101.

36. Peters, R.; van Bemmel, G.; Milani, N.; den Hertog, G.; Undas, A.; van der Lee, M.; and Bouwmeester, H. Detection of nanoparticles in Dutch surface waters. *Sci. Total Environ.* **2018**, *621*, 210-218.

37. Dayem, A.; Hossain, M.; Lee, S.; Kim, K.; Saha, S.; Yang, G.; Choi, H.; and Cho, S. The role of reactive oxygen species (ROS) in the biological activities of metallic nanoparticles. *Int. J. Mol. Sci.* **2017**, *18*, 120.

38. Yu, Z.; Li, Q.; Wang, J.; Yu, Y.; Wang, Y.; Zhou, Q.; and Li, P. Reactive oxygen spcies-related nanoparticle toxicity in the biomedical field. *Nanoscale Res. Lett.* **2020**, *15*, 115.

39. Perillo, B.; Di Donato, M.; Pezone, A.; Di Zazzo, E.; Giovannelli, P.; Galasso, G.; Castoria, G.; and Migliaccio, A. ROS in cancer therapy: the bright side of the moon. *Exp. Mol. Med.* **2020**, *52*, 192-203.

40. Liou, G.; and Storz, P. Reactive oxygen species in cancer. *Free Radic Res.* **2010**, *44(5)*.

41. Aggarwal, V.; Tuli, H.S.; Varol, A.; Thakral, F.; Yerer, M.B.; Sak, K.; Varol, M.; Jain, A.; Khan, M.A.; and Sethi, G.; Role of reactive oxygen species in cancer progression: molecular mechanisms and recent advancements. *Biomolecules.* **2019**, *9(11)*, 735.

42. OECD, https://www.oecd.org/chemicalsafety/nanosafety/overview-testing-programme-manufactured-nanomaterials.htm, accessed 20 April 2020.

43. Savage, D.; Hilt, J.; and Dziubla, T. In vitro methods for assessing nanoparticle toxicity. *Methods Mol. Biol.* **2019**, *1894*, 1-29.

44. Balke, J.; Volz, P.; Neumann, F.; Brodwolf, R.; Wolf, A.; Pischon, H.; Radbruch, M.; Mundhenk, L.; Gruber, A.; Ma, N.; and Alexiev, U. Visualizing oxidative cellular stress induced by nanoparticles in the subcytotoxic range using fluorescence lifetime imaging. *Small*. **2018**, *14(23)*.

45. Wu, L.; Sedgwick, A.; Sun, X.; Bull, S.; He, X.; and James, T. Reactive-based fluorescent probes for the detection and imaging of reactive oxygen, nitrogen, and sulfur species. *Acc. Chem. Res.* **2019**, *52*, 2582.

46. Dai, Y.; Yang, Z.; Cheng, S.; Wang, Z.; Zhang, R.; Zhu, G.; Wang, Z.; Yung, B.; Tian, R.; Jacobson, O.; Xu, C.; Ni, Q.; Song, J.; Sun, X.; Niu, G.; and Chen, X. Toxic reactive oxygen species enhanced synergistic combination therapy by self-assembled metal-phenolic network nanoparticles. *Adv. Mater.* **2018**, *30*, 1707877.

47. Kumar, V.; Sharma, N.; and Maitra, S. In vitro and in vivo toxicity assessment of nanoparticles. *Int. Nano Lett.* **2017**, *7*, 243.

48. Dönmez Güngüneş, Ç.; Şeker, Ş.; Elçin, A.; and Elçin, Y. A comparative study on the *in vitro* cytotoxic responses of two mammalian cell types to fullerenes, carbon nanotubes and iron oxide nanoparticles. *Drug. Chem. Toxicol.* **2017**, *40(2)*, 215.

49. Li, N.; Chen, L.; Zeng, C.; Yang, H.; He, S.; and Wei, Q. Comparative toxicity, biodistribution and excretion of ultra-small gold nanoclusters with different emission wavelengths. *J. Biomed. Nanotechnol.* **2021**, *17(9)*, 1778.

50. Gao, Y.; Wu, W.; Qiao, K.; Feng, J.; Zhu, L.; and Zhu, X. Bioavailability and toxicity of silver nanoparticles: determination based on toxicokinetic-toxicodynamic processes. *Water Res*. **2021**, *204*, 117603.

51. Zhang, Y.; Poon, W.; Tavares, A.; McGilvray, I.; and Chan, W. Nanoparticle-liver interactions: cellular uptake and hepatobiliary elimination. *JCR.* **2016**, *240*, 332.

52. Pritchard, N.; Kaitu'u-Lino, T.; Harris, L.; Tong, S.; and Hannan, N. Nanoparticles in pregnancy: the next frontier in reproductive therapeutics. *Hum. Reprod. Update.* **2021**, *27*, 280.

53. Báez, D.; Gallardo-Toledo, E.; Paz Oyarzún, M.; Araya, E.; and Kogan, M. The influence of size and chemical composition of silver and gold nanoparticles on in vivo toxicity with potential applications to central nervous system diseases. *Int. J. Nanomed*. **2021**, *16*, 2187.
54. Strojny, B.; Kurantowicz, N.; Sawosz, E.; Grodzik, M.; Jaworski, S.; Kutwin, M.; Wierzbicki, M.; Hotowy, A.; Lipińska, L.; and Chwalibog, A. Long term influence of carbon nanoparticles on health and liver status in rats. *PLoS ONE*. **2015**, *10(12).*
55. Zhang, M.; Bishop, B.; Thompson, N.; Hildahl, K.; Dang, B.; Mironchuk, O.; Chen, N.; Aoki, R.; Holmberg, V.; and Nance, E. Quantum dot cellular uptake and toxicity in the developing brain: implications for use as imaging probes. *Nanoscale Adv.* **2019**, *1*, 3424.
56. Xie, J.; Shen, Z.; Anraku, Y.; Kataoka, K.; and Chen, X. Nanomaterial-based blood-brain-barrier (BBB) crossing strategies. *Biomaterials.* **2019**, *224*, 119491.
57. Lee, D.; and Minko, T. Nanotherapeutics for nose-to-brain drug dlievery: an approach to bypass the blood brain barrier. *Pharmaceutics*. **2021**, *13(12)*, 2049.
58. Chowdhry, A.; Kaur, J.; Khatri, M.; Puri, V.; Tuli, R.; and Puri, S. Characterization of functionalized multiwalled carbon nanotubes and comparison of their cellular toxicity between HEK 293 cells and zebra fish in vivo. *Heliyon*. **2019**, *5(10)*, e02605.
59. Marisa, I.; Asnicar, D.; Matozzo, V.; Martucci, A.; Finos, L.; and Marin, M. Toxicological effects and bioaccumulation of fullerene C60 (FC60) in the marine bivalve Ruditapes philippinarum. *Ecotoxicol. Environ. Saf.* **2021**, *207*, 111560.
60. Tian, J.; Li, J.; Yin, H.; Ma, L.; Zhang, J.; Zhai, Q.; Duan, S.; and Zhang, L. In vitro and in vivo uterine metabolic disorders induced by silica nanoparticles through the AMPK signaling pathway. *Sci. Total Environ.* **2021**, *762*, 143152.

61. Lindén, M. Biodistribution and excretion of intravenously injected mesoporous silica nanoparticles: implications for drug delivery efficiency and safety. *Enzymes*. **2018**, *43*, 155.
62. Bartucci, R.; Paramanandana, A.; Boersma, Y.; Olinga, P.; and Salvati, A. Comparative study of nanoparticle uptake and impact in murine lung, liver and kidney tissue slices. *Nanotoxicology*. **2020**, *14(6)*, 847.
63. Waegeneers, N.; Brasseur, A.; Van Doren, E.; Van der Heyden, S.; Serreyn, P.; Pussemier, L.; Mast, J.; Schneider, Y.; Ruttens, A.; and Roels, S. Short-term biodistribution and clearance of intravenously administered silica nanoparticles. *Toxicol. Res*. **2018**, *5*, 632.
64. Mohammadpour, R.; Yazdimamaghani, M.; Cheney, D.; Jedrzkiewicz, J.; and Ghandehari, H. Subchronic toxicity of silica nanoparticles as a function of size and porosity. *JCR*. **2019**, *304*, 216.
65. Huang, Y.; Cambre, M.; and Lee, H. The toxicity of nanoparticles depends on multiple molecular and physicochemical mechanisms. *Int. J. Mol. Sci.* **2017**, *18(12)*, 2702.
66. Zhao, X.; Wang, Y.; Ji, Y.; Mei, R.; Chen, Y.; Zhang, Z.; Wang, X.; and Chen, L. Polystyrene nanoplastics demonstrate high structural stability in vivo: a comparative study with silica nanoparticles via SERS tag labeling. *Chemosphere*. **2022**, *300*, 134567.
67. Rana, A.; Yadav, K.; Jagadevan, S. A comprehensive review on green synthesis of nature-inspired metal nanoparticles: mechanism, application and toxicity. *J. Clean. Prod.* **2020**, *272*, 122880.
68. Rosário, F.; Duarte, I.; Pinto, R.; Santos, C.; Hoet, P.; and Oliveira, H. Biodistribution and pulmonary metabolic effects of silver nanoparticles in mice following acute intratracheal instillations. *ESPR*. **2020**, *28(2)*, 2301.

69. Zhang, Y.; Liu, A.; Cornejo, Y.; Van Haute, D.; and Berlin, J. A systematic comparison of in vitro cell uptake and in vivo biodistribution for three classes of gold nanoparticles with saturated PEG coatings. *PLoS ONE.* **2020**, *15(7)*, e0234916.

70. Janßen, H.; Angrisani, N.; Kalies, S.; Hansmann, F.; Kietzmann, M.; Warwas, D.; Behrens, P.; and Reifenrath, J. Biodistribution, biocompatibility and targeted accumulation of magnetic nanoporous silica nanoparticles as drug carrier in orthopedics. *J. Nanobiotechnol.* **2020**, *18(1)*, 14.

71. Mohammadpour, R.; Cheney, D.; Grunberger, J.; Yazdimamaghani, M.; Jedrzkiewicz, J.; Isaacson, K.; Dobrovolskaia, M.; and Ghandehari, H. One-year chronic toxicity evaluation of single dose intravenously administered silica nanoparticles in mice and their Ex vivo human hemocompatibility. *JCR.* **2020**, *324*, 471.

72. Chrishtop, V.; Prilepskii, A.; Nikonorova, V.; and Mironov, V. Nanosafety vs nanotoxicology: adequate animal models for testing in vivo toxicity of nanoparticles. *Toxicology*. **2021**, *462*, 152952.

73. Weaver, J.; Tobin, G.; Ingle, T.; Bancos, S.; Stevens, D.; Rouse, R.; Howard, K.; Goodwin, D.; Knapton, A.; Li, X.; Shea, K.; Stewart, S.; Xu. L.; Goering, P.; Zhang, Q.; Howard, P.; Collins, J.; Khan, S.; Sung, K.; and Tyner, K. Evaluating the potential of gold, silver, and silica nanoparticles to saturate mononuclear phagocytic system tissues under repeat dosing conditions. *Part. Fibre Toxicol.* **2017**, *14:25*.

74. Pu, K.; Chattopadhyay, N.; and Rao, J. Recent advances of semiconducting polymer nanoparticles in *in vivo* molecular imaging. *J. Control. Release.* **2016**, *240*, 312-322.

75. Voigt, N.; Henrich-Noack, P.; Kockentiedt, S.; Hintz, W.; Tomas, J.; and Sabel, B.A. Toxicity of polymeric nanoparticles in vivo and in vitro. *J. Nanopart. Res.* **2014**, *16*, 2379.

76. NIST, https://www.nist.gov/news-events/news/2019/08/solving-big-problem-measuring-tiny-nanoparticles, accessed 10 June 2021.

77. Shang, J.; and Gao, X. Nanoparticle counting: towards accurate determination of the molar concentration. *Chem. Soc. Rev.* **2014**, *43(12)*, 7267-7278.

78. Sayes, C.; Reed, K.; and Warheit, D. Assessing toxicity of fine and nanoparticles: comparing in vitro measurements to in vivo pulmonary toxicity profiles. *Toxicol. Sci.* **2007**, *97(1)*, 163-180.

79. Fischer, H.; and Chan, W. Nanotoxicity: the growing need for in vivo study. *Curr. Opin. Biotechnol.* **2007**, *18*, 565-571.

80. Jesus, S.; Schmutz, M.; Som, C.; Borchard, G.; Wick, P.; and Borges, O. Hazard assessment of polymeric nanobiomaterials for drug delivery: what can we learn from literature so far. *Bioeng. Biotechnol.* **2019**, *7*, 261.

81. Hund-Rinke, K.; Baun, A.; Cupi, D.; Fernandes, T.; Handy, R.; Kinross, J.; Navas, J.; Peijnenburg, W.; Schlich, K.; Shaw, B.; and Scott-Fordsmand, J. Regulatory ecotoxicity testing of nanomaterials – proposed modifications of OECD test guidelines based on laboratory experience with silver and titanium dioxide nanoparticles. *Nanotoxicol.* **2016**, *10(10)*, 1442.

82. Rasmussen, K.; Gonzalez, M.; Kearns, P.; Riego Sintes, J.; Rossi, F.; and Sayre, P. Review of achievements of the OECD working party on manufactured nanomaterials' testing and assessment programme: from exploratory testing to testing guidelines. *Reg. Toxicol. Pharm.* **2016**, *74*, 147-160.

83. Oberbek, P.; Kozikowski, P.; Czarnecka, K.; Sobiech, P.; Jakubiak, S.; and Jankowski, T. Inhalation exposure to various nanoparticles in work environment – contextual information and results of measurements. *J. Nanopart. Res.* **2019**, *21*, 222.

84. Felley-Bosco, E.; and MacFarlane, M. Asbestos: Modern insights for toxicology in the era of engineered nanomaterials. *Chem. Res. Toxicol.* **2018**, *31*, 994-1008.

85. Kim, J.; Jo, M.; Kim, Y.; Kim. T.; Shin, J.; Kim, B.; Kim, H.; Lee, H.; Kim, H.; Ahn, K.; Oh, S.; Cho, W.; and Yu, I. 28-Day inhalation toxicity study with evolution of lung deposition and retention of tangled multi-walled carbon nanotubes. *Nanotoxicol.* **2019**, *14*, 250-262.

86. Fujita, K.; Obara, S.; Maru, J.; and Endoh, S. Cytotoxicity profiles of multi-walled carbon nanotubes with different physico-chemical properties. *Toxicol. Mech. Methods.* **2020**, *30*, 477-489.

87. OECD, https://www.oecd.org/env/ehs/testing/test-no-412-subacute-inhalation-toxicity-28-day-study-9789264070783-en.htm, accessed 2 April 2021.

88. Nerl, H.; Cheng, C.; Goode, A.; Bergin, S.; Lich, B.; Gass, M.; and Porter, A. Imaging methods for determining uptake ad toxicity of carbon nanotubes *in vitro* and *in vivo*. *Nanomedicine.* **2011**, *6(5)*, 849-865.

89. Lama, S.; Merlin-Zhang, O.; and Yang, C. *In vitro* and *in vivo* models for evaluating the oral toxicity of nanomedicines. *Nanomaterials.* **2020**, *10(11)*, 2177.

90. Mader, B.; Ellefson, M.; and Wolf, S. Measurements of nanomaterials in environmentally relevant water matrices using liquid nebulization/differential mobility analysis. *Environ. Toxicol. Chem.* **2015**, *34*, 833.

91. Barbosa, F.; Adeyemi, J.; Bocato, M.; Comas, A.; and Campiglia, A. A critical viewpoint of current issue, limitations, and future research needs on micro- and nanoplastic studies: from the detection to the toxicological assessment. *Environ. Res.* **2020**, *182*, 109089.

92. Krug, H.F. The uncertainty with nanosafety: validity and reliability of published data. *Colloids Surf. B.* **2018**, *172*, 113-117.

93. AIHA, https://aiha-assets.sfo2.digitaloceanspaces.com/AIHA/resources/Nanoparticle-Sampling-and-Analysis-Fact-Sheet.pdf, accessed 25 March 2020.

94. Desai, N. Challenges in development of nanoparticle-based therapeutics. *AAPS J.* **2012**, *14(2)*, 282-295.

95. Sahu, S.; and Hayes, A. Toxicity of nanomaterials found in human environment: a literature review. *Toxicol. Res. Appl.* **2017**, *1*, 1-13.

96. Lead, J.; Batley, G.; Alvarez, P.; Croteau, M.; Handy, R.; McLaughlin, M.; Judy, J.; and Schirmer, K. Nanomaterials in the environment: behavior, fate, bioavailability, and effects – an updated review. *Environ. Toxicol. Chem.* **2018**, *37(8)*, 2029-2063.

97. TSI, https://tsi.com/products/particle-sizers/particle-size-spectrometers/, accessed 17 June 2021.

98. TSI, https://tsi.com/products/particle-sizers/electrostatic-classifiers-and-dmas/differential-mobility-analyzer-3081/, accessed 17 June 2021.

99. TSI, https://tsi.com/discontinued-products/nano-water-based-condensation-particle-counter-(cpc)-3788/, accessed 17 June 2021.

100. Savić-Zdraković, D.; Milošević, D.; Uluer, E.; Duran, H.; Matić, S.; Stanić, S.; Vidmar, J.; Šćančar, J.; Dikic, D.; and Jovanović, B. A multiparametric approach to cerium

oxide nanoparticle toxicity assessment in non-biting midges. *Environ. Toxicol. Chem.* **2020**, *39*, 131-140.

101. OECD, https://www.oecd-ilibrary.org/environment/test-no-218-sediment-water-chironomid-toxicity-using-spiked-sediment_9789264070264-en, accessed 5 April 2021.

102. Hadioui, M.; Knapp, G.; Azimzada, A.; Jreije, I.; Frechette-Viens, L.; and Wilkinson, K. Lowering the size detection limits of Ag and TiO_2 nanoparticles by single particle ICP-MS. *Anal. Chem.* **2019**, *91*, 13275-13284.

103. Tharaud, M.; Louvat, P.; and Benedetti, M. Detection of nanoparticles by single-particle ICP-MS with complete transport efficiency through direct nebulization at few-microliters-per-minute uptake rates. *Anal. Bioanal. Chem.* **2021**, *413*, 923-933.

104. Cui, X.; Fryer, B.; Zhou, D.; Lodge, R.; Khlobystov, A.; Valsami-Jones, E.; and Lynch, I. Core-shell $NaHoF_4$@TiO_2 NPs: a labeling method to trace engineered nanomaterials of ubiquitous elements in the environment. *ACS Appl. Mater. Interfaces.* **2019**, *11*, 19452-19461.

105. Turco, A.; Moglianetti, M.; Corvaglia, S.; Rella, S.; Catelani, T.; Marotta, R.; Malitesta, C.; and Pompa, P. Sputtering-enabled intracellular X-ray photoelectron spectroscopy: a versatile method to analyze the biological fate of metal nanoparticles. *ACS Nano.* **2018**, *12*, 7731-7740.

106. López-Serrano Oliver, A.; Haase, A.; Peddinghaus, A.; Wittke, D.; Jakubowski, N.; Luch, A.; Grützkau, A.; and Baumgart, S. Mass cytometry enabling absolute and fast quantification of silver nanoparticle uptake at the single cell level. *Anal. Chem.* **2019**, *91*, 11514-11519.

107. Forest, V. Experimental and computational nanotoxicology – Complementary approaches for nanomaterial hazard assessment. *Nanomaterials.* **2022**, *12*, 1346.

108. Tsukanov, A.; Turk, B.; Vasiljeva, O.; and Psakhie, S. Computational indicator approach for the assessment of nanotoxicity of two-dimensional nanomaterials. *Nanomaterials.* **2022**, *12*, 650

109. Huang, H.; Lee, Y.; Hsu, Y.; Liao, C.; Lin, Y.; and Chiu, H. Current strategies in assessment of nanotoxicity: alternatives to in vivo animal testing. *Int. J. Mol. Sci.* **2021**, *22*, 4216.

110. Taka, A.; Tata, C.; Klink, M.; Mbianda, X.; Mtunzi, F.; and Naidoo, E. A review on conventional and advancing methods for nanotoxicology evaluation of engineered nanomaterials. *Molecules.* **2021**, *26*, 6536.

111. Monikh, F.; Chupani, L.; Vijver, M.; Vancová, M.; and Peijnenburg, W. Analytical approaches for characterizing and quantifying engineered nanoparticles in biological matrices from an (eco)toxicological perspective: old challenges, new methods, and techniques. *Sci. Tot. Environ.* **2019**, *660*, 1283-1293.

112. Arvidsson, R.; Baun, A.; Furberg, A.; Hansen, S.; and Molander, S. Proxy measures for simplified environmental assessment of manufactured nanomaterials. *Environ. Sci. Technol.* **2018**, *52*, 13670-13680.

113. Fakhrullin, R.; Nigamatxyanova, L.; Fakhrullina, G. Dark field/hyperspectral microscopy for detecting nanoscale particles in environmental nanotoxicology research. *Sci. Tot. Environ.* **2021**, *772*, 145478.

114. Ellis, L.; Valsami-Jones, E.; and Lynch, I. Exposure medium and particle ageing moderate the toxicological effects of nanomaterials to Daphnia magna over multiple generations: a case for standard test review? *Environ. Sci.: Nano.* **2020**, *7*, 1136-1149.

115. Wigger, H.; Kägi, R.; Wiesner, M.; and Nowack, B. Exposure and possible risks of engineered nanomaterials in the environment – current knowledge and directions for the future. *Rev. Geophys.* **2020**, *58*, e2020RG000710.

116. Demirbaş, K.; and Çevik, S. Regulatory policies for safety of nanomaterials. *Open J. Nano.* **2020**, *5(1)*, 1-16.

117. Chugh, G.; Siddique, K.; and Solaiman, Z. Nanobiotechnology for agriculture: smart technology for combating nutrient deficiencies with nanotoxicity challenges. *Sustainability.* **2021**, *13*, 1781.

118. Nanotechnology Products Database, https://product.statnano.com/, accessed 27 May 2022.

119. Wang, D.; Chen, J.; and Dai, L. Recent advances in graphene quantum dots for fluorescence bioimaging from cells through tissues to animals. *Part. Part. Syst. Charact*. **2015**, *32*, 515-523.

120. Gurunathan, S.; Kim, E.; Han, J.; Park, J.; and Kim, J. Green chemistry approach for synthesis of effective anticancer palladium nanoparticles. *Molecules*. **2015**, *20*, 22476-22498.

121. Liu, J.; Zhang, F.; Allen, A.; Johnston-Peck, A.; and Pettibone, J. Comparing sulfidation kinetics of silver nanoparticles in simulated media using direct and indirect measurement methods. *Nanoscale.* **2018**, *10*, 22270-22279.

122. Griffin, S.; Masood, M.; Nasim, M.; Sarfraz, M.; Ebokaiwe, A.; Schäfer, K.; Keck. C.; and Jacob, C. Natural Nanoparticles: A particular matter inspired by nature. *Antioxidants.* **2018**, *7*, 3.

123. Chen, W.; Lv, G.; Hu, W.; Li, D.; Chen, S.; and Dai, Z. Synthesis and applications of graphene quantum dots: a review. *Nanotechnol Rev.* **2018**, *7(2)*, 157-185.

124. Tadyszak, K.; Wychowaniec, J.; and Litowczenko, J. Biomedical applications of graphene-based structures. *Nanomaterials.* **2018**, *8*, 944-964.

125. Atchudan, R.; Edison, T.; Perumal, S.; Clament Sagaya Selvam, N.; and Lee, Y. Green synthesized multiple fluorescent nitrogen-doped carbon quantum dots as an efficient label-free optical nanoprobe for in vivo live-cell imaging. *J. Photochem Photobiol A.* **2019**, *372*, 99-107.

126. Sun, J.; Cui, F.; Zhang, R.; Gao, Z.; Ji, J.; Ren, Y.; Pi, F.; Zhang, Y.; and Sun, X. Comet-like heterodimers “gold nanoflower @graphene quantum dots” probe with FRET “off” to DNA circuit signal “on” for sensing and imaging MicroRNA in vitro and in vivo. *Anal. Chem.* **2018**, *90*, 11538-11547.

127. Zhao, M. Direct synthesis of graphene quantum dots with different fluorescence properties by oxidation of graphene oxide using nitric acid. *Appl. Sci.* **2018**, *8*, 1303-1313.

128. Jiang, D.; Chen, Y.; Li, W.; Wang, Z.; Zhu, J.; Zhang, H.; Liu, B.; and Xu, S. Synthesis of luminescent graphene quantum dots with high quantum yield and their toxicity study. *Plos One.* **2015**, *10(12)*.

129. Tian, P.; Tang, L.; Teng, K.; and Lau, S. Graphene quantum dots from chemistry applications. *Mater. Today. Chem.* **2018**, *10*, 221-258.

130. Şenel, B.; Demir, N.; Büyükköroğlu, G.; and Yıldız, M. Graphene quantum dots: synthesis, characterization, cell viability, genotoxicity for biomedical applications. *Saudi Pharm. J.* **2019**.

131. Ting, S.; Ee, S.; Ananthanarayanan, A.; Leong, K.; and Chen, P. Graphene quantum dots functionalized gold nanoparticles for sensitive electrochemical detection of heavy metal ions. *Electrochimica Acta.* **2015**, *172*, 7-11.

132. Zhou, C.; Jiang, W.; and Via, B. Facile synthesis of soluble graphene quantum dots and its improved property of detecting heavy metal ions. *Colloids Suf B Biointerfaces*. **2014**, *118*, 72-76.

133. Yousaf, M.; Ahmad, M.; Ahmad Bhatti, I.; Nasir, A.; Hasan, M.; Jian, X.; Kalantar-Zadeh, K.; and Mahmood, N. In vivo and In vitro monitoring of amyloid aggregation via BSA@FGQDs multimodal probe. *ACS Sens.* **2019**, *4*, 200-210.

134. Liu, J.; Qin, L.; Kang, S.; Li, G.; and Li, X. Gold nanoparticles/glycine derivatives/graphene quantum dots composite with tunable fluorescence and surface enhanced Raman scattering signals for cellular imaging. *Mater. Design.* **2017**, *123*, 32-38.

135. Zhao, W.; Li, Y.; Yang, S.; Chen, Y.; Zheng, J.; Liu, C.; Qing, Z.; Li, J.; and Yang, R. Target-activated modulation of dual-color and two-photon fluorescence of graphene quantum dots for in vivo imaging of hydrogen peroxide. *Anal. Chem.* **2016**, *88*, 4833-4840.

136. Nair, R.; Thomas, R.; Sankar, V.; Muhammad, H.; Dong, M.; and Pillai, S. Rapid, acid-free synthesis of high-quality graphene quantum dots for aggregation induced sensing of metal ions and bioimaging. *ACS Omega.* **2017**, *2*, 8051-8061.

137. Kalluri, A.; Debnath, D.; Dharmadhikari, B.; and Patra, P. Graphene quantum dots: synthesis and applications. *Methods Enzymol*. **2018**, *609*, 335-353.

138. Zeng, X.; Yuan, Y.; Wang, T.; Wang, H.; Hu, X.; Fu, Z.; Zhang, G.; Liu, B.; and Lu, G. Targeted imaging and induction of apoptosis of drug-resistant Hepatoma cells by miR-122-loaded graphene-lnP nanocompounds. *Nanobiotechnol.* **2017**, *15:9*.

139. Yao, C.; Tu, Y.; Ding, L.; Li, C.; Wang, J.; Fang, H.; Huang, Y.; Zhang, K.; Lu, Q.; Wu, M.; and Wang, Y. Tumor cell-specific nuclear targeting of functionalized graphene quantum dots in vivo. *Bioconjugate Chem.* **2017**, *28*, 2608-2619.

140. Ramachandran, S.; Sathishkumar, M.; Kothurkar, N.; and Senthilkumar, R. Synthesis and characterization of graphene quantum dots/cobalt ferrite nanocomposite. *IOP. Conf. Ser.:Mater. Sci. Eng.* **2018**, *310*, 012139.

141. Zhang, L.; Peng, D.; Lian, R.; and Qiu, J. Graphene-based optical nanosensors for detection of heavy metal ions. *Trends Anal. Chem.* **2018**, *102*, 280-289.

142. Feng, L.; Wu, Y.; Zhang, D.; Hu, X.; Zhang, J.; Wang, P.; Song, Z.; Zhang, X.; and Tan, W. Near infrared graphene quantum dots-based two-photon nanoprobe for Direct bioimaging of endogenous ascorbic acid in living cells. *Anal. Chem.* **2017**, *89*, 4077-4084.

143. Huang, D.; Zhou, H.; Wu, Y.; Wang, T.; Sun, L.; Gao, P.; Sun, Y.; Huang, H.; Zhou, G.; and Hu, J. Bottom-up synthesis and structural design strategy for graphene quantum dots with tunable emission to the near infrared region. *Carbon*. **2019**, *142*, 673-684.

144. Bao, X.; Yuan, T.; Chen, J.; Zhang, B.; Li, D.; Zhou, D.; Jing, P.; Xu, G.; Wang, Y.; Holá, K.; Shen, D.; Wu, C.; Song, S.; Liu, C.; Zboĥil, R.; and Qu, S. In vivo theranostics with near-infrared-emitting carbon dots – highly efficient photothermal therapy based on passive targeting after intravenous administration. *Light Sci. Appl.* **2018**, *7*, 91-102. https://doi.org/10.1038/s41377-018-0090-1.

145. Laurenti, M.; Paez-Perez, M.; Algarra, M.; Alonso-Cristobal, P.; Lopen-Cabarcos, E.; Mendez-Gonzalez, D.; and Rubio-Retama, J. Enhancement of the upconversion rmission by visible-to-near-infrared fluorescent graphene quantum dots for miRNA detection. *Appl. Mater. Interfaces.* **2016**, *8*, 12644-12651.

146. Tang, L.; Ji, R.; Li, X.; Bai, G.; Liu, C.; Hao, J.; Lin, J.; Jiang, H.; Teng, K.; Yang, Z.; and Lau, S. Deep ultraviolet to near-infrared emission and photoresponse in layered N-doped graphene quantum dots. *ACS Nano.* **2014**, *8(6)*, 6312.

147. Ayoubi, M.; Naserzadeh, P.; Hashemi, M.; Rostami, M.; Tamjid, E.; Tavakoli, M.; and Simchi, A. Biochemical mechanisms of dose-dependent cytotoxicity and ROS-mediated apoptosis induced by lead sulfide/graphene oxide quantum dots for potential bioimaging applications. *Sci. Reports.* **2017**, *7*, 12896.

148. Lee, B.; McKinney, R.; Hasan, T.; and Naumov, A. Graphene quantum dots as intracellular imaging-based temperature sensors. *Materials*. **2021**, *14*, 616.

149. Tayyebi, A.; Akhavan, O.; Lee, G.; and Outokesh, M. Supercritical water in top-down formation of tunable-sized graphene quantum dots applicable in effective photothermal treatments of tissues. *Carbon*. **2018**, *130*, 267-272.

150. Kumawat, M.; Thakur, M.; Gurung, R.; and Srivastava, R. Graphene quantum dots from Mangifera Indica: application in near-infrared bioimaging and intracellular nanothermometry. *ACS Sustainable Chem. Eng.* **2017**, *5*, 1382-1391.

151. Zhu, P.; Zhang, T.; Li, J.; Ma, J.; Ouyang, X.; Zhao, X.; Xu, M.; Wang, D.; and Xu, Q. Near-infrared emission Cu, N-doped carbon dots for human Umbilical Vein Endothelial cell labeling and their biocompatibility in vitro. *J. Appl. Toxicol.* **2021**, *41(5)*, 789-798.

152. Huang, P.; Shi, J.; Zhang, M.; Jiang, X.; Zhong, H.; Ding, Y.; Cao, X.; Wu, M.; and Lu, J. Anomalous light emission and wide photoluminescence spectra in graphene quantum dot: quantum confinement from edge microstructure. *J. Phys. Chem. Lett.* **2016**, *7*, 2888-2892.

153. Kuo, Q.; Shen, X.; Chang, C.; Kao, H.; Lin, S.; Wang, J.; and Wu, P. Multiplexed graphene quantum dots with excitation-wavelength-independent photoluminescence, as two-photon probes, and in ultraviolet-near infrared bioimaging. *ACS Nano.* **2020**, *14*, 11502-11509.

154. Jeong, H.; Song, J.; Jeong, S.; and Chang, W. Graphene/PbS quantum dot hybrid structure for application in near-infrared photodetectors. *Sci. Rep.* **2020**, *10*, 12475.

155. Hai, X.; Feng, J.; Chen, X.; and Wang, J. Tuning the optical properties of graphene quantum dots for biosensing and bioimaging. *J. Mater. Chem. B.* **2018**, *6*, 3219-3234.

156. Chen, F.; Gao, W.; Qui, X.; Zhang, H.; Liu, L.; Liao, P.; Fu, W.; and Luo, Y. Graphene quantum dots in biomedical applications: recent advances and future challenges. *Front. Lab. Med.* **2017**, *1*, 192-199.

157. Li, K.; Liu, W.; Ni, Y.; Li, D.; Lin, D.; Su, Z.; and Wei, G. Technical synthesis and biomedical applications of graphene quantum dots. *J. Mater. Chem. B.* **2016**, *00*, 1-3.

158. Wang, L.; Wang, Y.; Xu, T.; Liao, H.; Yao, C.; Liu, Y.; Li, Z.; Chen, Z.; Pan, D.; Sun, L.; and Wu, M. Gram-scale synthesis of single-crystalline graphene quantum dots with superior optical properties. *Nat. Commun.* **2014**, *5*, 5357.

159. Tang, L.; Ji, R.; Cao, X.; Lin, J.; Jiang, H.; Li, X.; Teng, K. S.; Luk, C. M.; Zeng, S.; Hao, J.; and Lau, S.P. Deep ultraviolet photoluminescence of water-soluble self-passivated graphene quantum dots. *ACS Nano* **2012**, *6*, 5102–5110.

160. Wang, Z.; Yu, J.; Zhang, X.; Li, N.; Liu, B.; Li, Y.; Wang, Y.; Wang, W.; Li, Y.; Zhang, L.; Dissanayake, S.; Suib, S.L.; and Sun, L. Large-scale and controllable synthesis of graphene quantum dots from rice husk biomass: a comprehensive utilization strategy. *ACS Appl. Mater. Interfaces.* **2016**, *8* (2), 1434–1439.

161. Suryawanshi, A.; Biswal, M.; Mhamane, D.; Gokhale, R.; Patil, S.; Guin, D.; and Ogale, S. Large scale synthesis of graphene quantum dots (GQDs) from waste biomass and their use as an efficient and selective photoluminescence on–off–on probe for Ag^{+} ions. *Nanoscale* **2014**, *6* (20), 11664–11670.

162. Prasannan, A.; and Imae, T. One-pot synthesis of fluorescent carbon dots from orange waste peels. *Ind. Eng. Chem. Res.* **2013**, *52* (44), 15673–15678.

163. Park, S. Y.; Lee, H. U.; Park, E. S.; Lee, S. C.; Lee, J.-W.; Jeong, S. W.; Kim, C. H.; Lee, Y.-C.; Huh, Y. S.; and Lee, J. Photoluminescent green carbon nanodots from food-waste-derived sources: large-scale synthesis, properties, and biomedical applications. *ACS Appl. Mater. Interfaces* **2014**, *6* (5), 3365–3370.

164. Dong, Y.; Shao, J.; Chen, C.; Li, H.; Wang, R.; Chi, Y.; Lin, X.; and Chen, G. Blue luminescent graphene quantum dots and graphene oxide prepared by tuning the carbonization degree of citric acid. *Carbon N. Y.* **2012**, *50* (12), 4738–4743.

165. Wu, X.; Tian, F.; Wang, W.; Chen, J.; Wu, M.; and Zhao, J. X. Fabrication of highly fluorescent graphene quantum dots using L-glutamic acid for in vitro/in vivo imaging and sensing. *J. Mater. Chem. C* **2013**, *1* (31), 4676–4684.

166. Ding, Z.; Li, F.; Wen, J.; Wang, X.; and Sun, R. Gram-scale synthesis of single-crystalline graphene quantum dots derived from lignin biomass. *Green Chem.* **2018**, *20* (6), 1383–1390.

167. Bozell, J. J.; and Petersen, G. R. Technology Development for the production of biobased products from biorefinery carbohydrates—the US Department of Energy's "Top 10" revisited. *Green Chem.* **2010**, *12* (4), 539–554.

168. Mika, L. T.; Cséfalvay, E.; and Németh, Á., Catalytic conversion of carbohydrates to initial platform chemicals: chemistry and sustainability *Chem. Rev.* **2018**, *118*, 505-613.

169. Bender, T. A.; Dabrowski, J. A.; and Gagné, M. R. Homogeneous catalysis for the production of low-volume, high-value chemicals from biomass *Nat. Rev. Chem.* **2018**, *2*, 35-46.

170. Wang, Z.; Scheuring, M.; Mabin, M.; Shahni, R.; Wang, Z. D.; Ugrinov, A.; Butz, J.; and Chu, Q. R. Renewable cyclobutane-1,3-dicarboxylic acid (CBDA) building block synthesized from furfural via photocyclization. *ACS Sustainable Chem. Eng.* **2020**, *8*, 8909-8917.

171. Wang, Z. D.; Elliott, Q.; Wang, Z.; Setien, R.; Puttkammer, J.; Ugrinov, A.; Lee, J.; Webster, D.; and Chu, Q. Furfural-derived diacid prepared by photoreaction for sustainable materials synthesis. *ACS Sustainable Chem. Eng.* **2018**, *6*, 8136-8141.

172. Horiba, https://www.horiba.com/en_en/applications/materials/material-research/quantum-dots/recording-fluorescence-quantum-yields/, accessed 6 December 2019.

173. Rode, J.E.; Dobrowolski, J.C.; and Rzączyńska, Z. DFT conformation and IR spectra of 1,1-dicarboxycylobutane. *J. Mol. Struct.* **2002**, *642*, 147-156.

174. NIST, https://webbook.nist.gov/cgi/inchi?ID=C1124136&Mask=80, accessed 1 December 2019.

175. Yu, N.; Peng, H.; Xiong, H.; Wu, X.; Wang, X.; Li, Y.; and Chen, Y. Graphene quantum dots combined with copper(II) ions as a fluorescent probe for turn-on detection of sulfide ions. *Microchim Acta*. **2015**, *182(13-14)*, 2139-2146.

176. Fan, T.; Zeng, W.; Tang, W.; Tuan, C.; Tong, S.; Cai, K.; Liu, Y.; Huang, W.; Min, Y.; and Epstein, A.J. Controllable size-selective method to prepare graphene quantum dots from graphene oxide. *Nanoscale. Res. Lett.* **2015**, *10*, 55.

177. Liu, Q.; Zhang, J.; He, H.; Huang, G.; Zing, B.; Jia, J.; and Zhang, C. Green preparation of high yield fluorescent graphene quantum dots from coal-tar-pitch by mild oxidation. *Nanomaterials.* **2018**, *8(10)*, 844.

178. Vasimalai, N.; Vilas-Boas, V.; Gallo, J.; de Fátima Cerqueira, M.; Ménendez-Miranda, M.; Costa-Fernández, J.; Diéguez, L.; Espiña, B.; and Fernández-Argüelles, T. Green synthesis of fluorescent carbon dots from species for in vitro imaging and tumour cell growth inhibition. *Beilstein J. Nanotechnol.* **2018**, *9*, 530-544.

179. Chhabra, V.A.; Kaur, R.; Kumar, N.; Deep, A.; Rajesh, C.; and Kim, K. Synthesis and spectroscopic studies of functionalized graphene quantum dots with diverse fluorescence characteristics. *RSC Adv.* **2018**, *8*, 11446-11454.

180. Moulder, J.; Stickle, W.; Sobol, P.; and Bomben, K. *Handbook of X-ray Photoelectron Spectroscopy.* Perkin-Elmer Corporation: Eden Prairie, 1992, 40-44.

181. Hashemzadeh, N.; Hasanzadeh, M.; Shadjou, N.; Eivazi-Ziaei, J.; Khoubnasabjafari, M.; and Jouyban, A. Graphene quantum dot modified glassy carbon electrode for determination of Doxorubicin hydrochloride in human plasma. *J. Pharm. Anal.* **2016**, *6*, 235-241.

182. Yan, R.; Wu, H.; Zheng, Q.; Wang, J.; Juang, J.; Ding, K.; Guo, Q.; and Wang, J. Graphene quantum dots cut from the graphene flakes: high electrocatalytic activity for oxygen reduction and low cytotoxicity. *RSC Adv.* **2014**, *4*, 23097.

183. Nair, R.; Thomas, R.; Sankar, V.; Muhammad, H.; Dong, M.; and Pillai, S. Rapid, acid-free synthesis of high-quality graphene quantum dots for aggregation induced sensing of metal ions and bioimaging. *ACS Omega.* **2017**, *2*, 8051-8061.

184. Lei, Q.; Pan, T.; Ou, L.; Ye, Z.; Yu, C.; Bao, B.; Wu, Z.; Cao, D.; and Dai, L. Biocompatible nucleus-targeted graphene quantum dots for selective killing of cancer cells via DNA damage. *Commun. Biol.* **2021**, *4*, 214.

185. Perini, G.; Palmieri, V.; Ciasca. G.; De Spirito, M.; and Papi, M. Unravelling the potential of graphene quantum dots in biomedicine and neuroscience. *Int. J. Mol. Sci.* **2020**, *21*, 3712.

186. Kumawat, M.; Thakur, M.; Gurung, R.; and Srvastava, R. Graphene quantum dots for cell proliferation, nucleus imaging, and photoluminescent sensing applications. *Sci. Rep.* **2017**, *7*, 15858.

187. Oh, N.; and Park, J. Endocytosis and exocytosis of nanoparticles in mammalian cells. *Int. J. Nanomed.* **2014**, *9*, 51-63.

188. Chen, W.; Lv, G.; Hu, W.; Li, D.; Chen, S.; and Dai, Z. Synthesis and applications of graphene quantum dots: a review. *Nanotechnol Rev.* **2018**, *7(2)*, 157-185.

189. Tadyszak, K.; Wychowaniec, J.; and Litowczenko, J. Biomedical applications of graphene-based structures. *Nanomaterials.* **2018**, *8*, 944-964.

190. Jovanović, S.; Syrgiannis, Z.; Marković, Z.; Bonasera, A.; Kepić, D.; Budimir, M.; Milivojević, D.; Spasojević, V.; Dramićanin, M.; Pavlović, V.; and Todorović Marković,

B. Modification of structural and luminescence properties of graphene quantum dots by gamma irradiation and their application in a photodynamic therapy. *ACS Appl. Mater. Interfaces.* **2015**, *7*, 25865-25874.

191. Mansuriya, B.; and Altintas, Z. Applications of graphene quantum dots in biomedical sensors. *Sensors.* **2020**, *20(4)*, 1072.

192. Wang, B.; Shen, J.; Huang, Y.; Liu, Z.; and Zhuang, H. Graphene quantum dots and enzyme-coupled biosensors for highly sensitive determination of hydrogen peroxide and glucose. *Int. J. Mol. Sci.* **2018**, *19(6)*, 1696.

193. Ayilliath, S.; Nair, S.; Lakshmi, G.; and Kunnatheery, S. Functionalized graphene quantum dots for cholesterol detection in human blood serum. *J. Fluoresc.* **2021**.

194. Raj. S.; Yadav, V.; Bhadu, G.; Patidar, R.; Kumar, M.; and Kulshrestha, V. Synthesis of highly fluorescent and water soluble graphene quantum dots for detection of heavy metal ions in aqueous media. *Envir. Sci. Pollut. Res.* **2020**.

195. Shah, H.; Xie, W.; Wang, Y.; Jia, X.; Nawaz, A.; Xin, Q.; Song, M.; and Gong, J. Preparation of blue- and green-emissive nitrogen-doped graphene quantum dots from graphite and their application in bioimaging. *Mater. Sci. Eng. C.* **2021**, *119*, 111643.

196. Minati, L.; and Del Piano, A. Facile synthesis of water-soluble, highly-fluorescent graphene quantum dots from graphene oxide reduction for efficient cell labelling. *C.* **2019**, *5(4)*, 77.

197. Polesskaya, O.; Baranova, A.; Bui, S.; Kondratev, N.; Kananykhina, E.; Nazarenko, O.; Shapiro, T.; Nardia, F.; Kornienko, V.; Chandhoke, V.; Stadler, I.; Lanzafame, R.; and Myakishev-Rampel, M. Optogenetic regulation of transcription. *Neurosci.* **2018**, *19*, 12-23.

198. Liu, K.; Song, S.; Sui, L.; Wu, S.; Jing, P.; Wang, R.; Li, Q.; Wu, G.; Zhang, Z.; Yuan, K.; and Shan, C. Efficient red/near-infrared-emissive carbon nanodots with multiphoton excited upconversion fluorescence. *Adv. Sci.* **2019**, *6*, 1900766.

199. Pan, L.; Sun, S.; Zhang, A.; Jiang, K.; Zhang, L.; Dong, C.; Huang, Q.; Wu, A.; and Lin, H. Truly fluorescent excitation-dependent carbon dots and their applications in multicolor cellular imaging and multidimensional sensing. *Adv. Mater.* **2015**, *27*, 7782-7787.

200. Kuo, W.; Shen, X.; Chang, C.; Kao, H.; Lin, S.; Wang, J.; and Wu, P. Multiplexed graphene quantum dots with excitation-wavelength-independent photoluminescence, as two-photon probes, and in ultraviolet-near infrared bioimaging. *ACS Nano.* **2020**, *14*, 11502-11509.

201. Song, Z.; Dai, X.; Li, M.; Teng, H.; Song, Z.; Xie, D.; and Luo, X. Biodegradable nanoprobe based on MnO_2 nanoflowers and graphene quantum dots for near infrared fluorescence imaging of glutathione in living cells. *Microchimica Acta.* **2018**, *185*, 485-493.

202. Campbell, E.; Hasan, M.; Rodriguez, R.; Akkaraju, G.; and Naumov, A. Doped graphene quantum dots for intracellular multicolor imaging and cancer detection. *ACS Biomater. Sci. Eng.* **2019**, *5*, 4671-4682.

203. Yang, D.; Yao, X.; Dong, J.; Wang, N.; Du, Y.; Sun, S.; Gao, L.; Zhong, Y.; Qian, C.; and Hong, H. Design and investigation of core/shell GQDs/hMSN nanoparticles for enhanced drug delivery platform in triple-negative breast cancer. *Bioconjugate Chem.* **2018**, *29*, 2776-2785.

204. Tahoun, M.; Gee, C.; McCoy, V.; Sander, P.; and Müller, C. Chemistry of porphyrins in fossil plants and animals. *RSC Adv*. **2021**, *11*, 7552.

205. Qi, Z.; Cheng, Y.; Xu, Z.; and Chen, M. Recent advances in porphyrin-based materials for metal ions detection. *Int. J. Mol. Sci.* **2020**, *21*, 5839.

206. Ussia, M.; Bruno, E.; Spina, E.; Vitalini, D.; Pellegrino, G.; Ruffino, F.; Privitera, V.; and Carroccio, S. Freestanding photocatalytic materials based on 3D graphene and polyporphyrins. *Sci Rep.* **2018**, *8*, 5001.

207. Hadmojo, W.; Yim, D.; Aqoma, H.; Ryu, D.; Shin, T.; Kim, H.; Hwang, E.; Jang, W.; Jung, I.; and Jang, S. Artificial light-harvesting n-type porphyrin for panchromatic organic photovoltaic devices. *Chem. Sci*. **2017**, *8*, 5095.

208. Jin, G.; He, R.; Liu, Q.; Lin, M.; Dong, Y.; Li, K.; Tang, B.; Liu, B.; and Xu, F. Near-infrared light-regulated theranostic nanoplatform based on aggregation-induced emission luminogen encapsulated upconversion nanoparticles. *Theranostics.* **2019**, *9*, 246-264.

209. Mahajan, P.; Dige, N.; Vanjare, B.; Phull, A.; Kim, S.; Hong, S.; and Lee, K. Synthesis, photophysical properties and application of new porphyrin derivatives for use in photodynamic therapy and cell imaging. *J. Fluoresc.* **2018,** *28*, 871-882.

210. Wang, D.; Zhang, Z.; Lin, L.; Liu, F.; Wang, Y.; Guo, Z.; Li, Y.; Tian, H.; and Chen, X. Porphyrin-based covalent organic framework nanoparticles for photoacoustic imaging-guided photodynamic and photothermal combination cancer therapy. *Biomater.* **2019**, *223*, 119459.

211. Reagen, S.; Wu, Y.; Liu, X.; Shahni, R.; Bogenschuetz, J.; Wu, X.; Chu, Q.; Oncel, N.; Zhang, J.; Hou, X.; Combs, C.; Vasquez, A.; and Zhao, J.X. *ACS Appl. Mater. Inter.* **2021**, *13*, 43952.

212. Li, B.; Wang, X.; Chen, L.; Zhou, Y.; Dang, W.; Chang, J.; and Wu, C. Ultrathin Cu-TCPP MOF nanosheets: a new theragnostic nanoplatform with magnetic resonance/near-infrared thermal imaging for synergistic phototherapy of cancers. *Theranostics.* **2018**, *8(15)*, 4086-4096.

213. Jia, Y.; Li, F.; Jia, T.; and Wang, Z. Meso-tetra(4-carboxylphenyl)porphine-enhanced DNA methylation sensing interface on a light-addressable potentiometric sensor. *ACS Omega*. **2019**, *4*, 12567-12574.

214. Wang, Z.; Elliot, Q.; Wang, Z.; Setien, R.; Puttkammer, J.; Ugrinov, A.; Lee, J.; Webster, D.; and Chu, Q.R. Fufural-derived diacid prepared by photoreaction for sustainable materials synthesis. *ACS Sustain. Chem. Eng.* **2018**, *6*, 8136-8141.

215. Wu, J.; Wang, W.; and Wang, Z. Porphin-based carbon dots for "turn off-on" phosphate sensing and cell imaging. *Nanomater.* **2020**, *10*, 326.

216. Zhang, X.; Hou, L.; Richard, F.; and Samori, P. Modular preparation of graphene-based functional architectures through two-step organic reactions: toward high-performance energy storage. *Chemistry.* **2018**, *24(69)*, 18518.

217. Liu, Q.; Li, H.; Zhao, Q.; Zhu, R.; Yang, Y.; Jia, Q.; Bian, B.; and Zhuo, L. Glucose-sensitive colorimetric sensor based on peroxidase mimics activity of porphyrin-Fe_3O_4 nanocomposites. *Mater. Sci. Eng. C.* **2014**, *41*, 142-151.

218. Nair, R.; Thomas, R.; Sankar, V.; Muhammad, H.; Dong, M.; and Pillai, S. Rapid, Acid-free Synthesis of High-quality Graphene Quantum Dots for Aggregation Induced Sensing of Metal Ions and Bioimaging. *ACS Omega.* **2017**, *2*, 8051-8061.

219. Shaikh, S.; Chakraborty, A.; Alatis, J.; Cai, M.; Danilov, E.; and Morris, A. Light harvesting and energy transfer in a porphyrin-based metal organic framework. *Faraday Discuss.* **2019**, *216*, 174-190.

220. Dehaen, R.; Vaz Serra, V.; Botequim, D.; Paulo, P.; Andrade, S.; and Costa, S. Fluorescence spectroscopy of porphyrins and phthalocyanines: some insights into supramolecular self-assembly, microencapsulation, and imaging microscopy. *Molecules.* **2021**, *26(14)*, 4264.

221. Yoon, H.; Park, M.; Kim, J.; Novak, T.; Lee, S.; and Jeon, S. Toward highly efficient luminescence in graphene quantum dots for optoelectronic applications. *Chem. Phys. Rev.* **2021**, *2(3)*, 031303.

222. Liu, C.; Zhang, F.; Hu, J.; Gao, W.; and Zhang, M. A mini review on pH-sensitive photoluminescence in carbon nanodots. *Front. Chem.* **2021**, *8*, 605028.

223. Choi, M.; Pollard, J.; Webb, M.; and McHale. J. Counterion-dependent excitonic spectra of tetra(p-carboxyphenyl)porphyrin aggregates in acidic aqueous solution. *J. Am. Chem. Soc.* **2003**, *125(3)*, 810-820.

224. Hassan, G.; El Hoda Saad, N.; Hmadeh, M.; and Karam, P. Enhancing porphyrin photostability when locked in metal-organic frameworks. *Dalton Trans.* **2018**, *47*, 15765-15771.

225. Sulek, A.; Pucelik, B.; Kobielusz, M.; Barzowska, A.; and Dabrowski, J. Photodynamic inactivation of bacteria with porphyrin derivatives: effect of charge,

lipophilicity, ROS generation, and cellular uptake on their biological activity in vitro. *Int. J. Mol. Sci.* **2020**, *21*, 8716.

226. Fasbender, S.; Allani, S.; Wimmenauer, C.; Cadeddu, R.; Raba, K.; Fischer, J.; Bulat, B.; Luysberg, M.; Seidel, C.; Heinzel, T.; and Haas, R. Uptake dynamics of graphene quantum dots into primary human blood cells following in vitro exposure. *RSC Adv.* **2017**, *7*, 12208-12216.

227. Perini, G.; Palmieri, V.; Ciasca, G.; De Spirito, M.; and Papi, M. Unravelling the potential of graphene quantum dots in biomedicine and neuroscience. *Int. J. Mol. Sci.* **2020**, *21*, 3712.

228. Wei, K.; Yao, F.; and Kang, X. Single-molecule porphyrin-metal ion interaction and sensing application. *Biosens. Bioelectron.* **2018**, *109*, 272-278.

229. Wang, Q.; Ke, W.; Lou, H.; Han, Y.; and Wan, J. A novel fluorescent metal-organic framework based on porphyrin and AIE for ultra-high sensitivity and selectivity detection of Pb^{2+} ions in aqueous solution. *Dyes Pigm.* **2021**, *196*, 109802.

230. Ermakova, E.; Koroleva. E.; Shokurov, A.; Arslanov, V.; and Kessmertnykh-Lemeune, A. Ultra-thin film sensors based on porphyrin-5-ylphosphonate diesters for selective and sensitive dual-channel optical detection of mercury (II) ions. *Dyes Pigm.* **2021**, *186*, 108967.

231. Fu, C.; Sun, X.; Zhang, G.; Shi, P.; and Chu, P. Porphyrin-based metal-organic framework probe: highly selective and sensitive fluorescent turn-on sensor for M^{3+} (Al^{3+}, Cr^{3+}, and Fe^{3+}) ions. *Inorg. Chem.* **2021**, *60*, 1116-1123.

232. Qi, Z.; Cheng, Y.; Xu, Z.; and Chen, M. Recent advances in porphyrin-based materials for metal ion detection. *Int. J. Mol. Sci.* **2020**, *21*, 5839.

233. Sung, H.; Ferlay, J.; Siegel, R.; Laversanne, M.; Soerjomataram, I.; Jemal, A.; and Bray, F. Global cancer statistics 2020: GLOBOCAN estimates of incidence and mortality worldwide for 36 cancers in 185 countries. *CA Cancer J. Clin.* **2021**, *71*, 209.

234. Palesh, O.; Scheiber, C.; Kesler, S.; Mustian, K.; Koopman, C.; and Schapira, L. Management of side effects during and post-treatment in breast cancer survivors. *Breast J.* **2017**, *24*, 167.

235. Liu, Y.; Wang, X.; He, D.; and Cheng, Y. Protection against chemotherapy- and radiotherapy-induced side effects: a review based on the mechanisms and therapeutic opportunities of phytochemicals. *Phytomedicine.* **2021**, *80*, 153402.

236. CDC, Cancer Patients: Diagnosis and Treatment | CDC, accessed 31 March 2022.

237. NIH, Side Effects of Cancer Treatment - National Cancer Institute, accessed 31 March 2022.

238. Pucci, C.; Martinelli, C.; and Ciofani, G. Innovative approaches for cancer treatment: current perspectives and new challenges. *Ecancer.* **2019**, *13*, 961.

239. Barroso-Sousa, R.; and Tolaney, S. Clinical development of new antibody-drug conjugates in breast cancer: to infinity and beyond. *BioDrugs.* **2021**, *35*, 159.

240. Broadfield, L.; Pane, A.; Talebi, A.; Swinnen, J.; and Fendt, S. Lipid metabolism in cancer: new perspectives and emerging mechanisms. *Dev. Cell.* **2021**, *56*, 1363.

241. Gavas, S.; Quazi, S.; and Karpinski, T. Nanoparticles for cancer therapy: current progress and challenges. *Nanoscale Res. Lett.* **2021**, *16*, 173.

242. Jain, R.; Vithalani, R.; Patel, D.; Lad, U.; Modi, C.; Suthar, D.; Solanki, J.; and Surati, K. Highly fluorescent nitrogen-doped graphene quantum dots (N-GQDs) as an

efficient nanoprobe for imaging of microbial cells. *Fuller. Nanotub. Car. N.* **2021**. DOI: 10.1080/1536383X.2021.1872548.

243. Fan, Z.; Li, S.; Yuan, F.; and Fan, L. Fluorescent graphene quantum dots for biosensing and bioimaging. *RSC Adv.* **2015**, *5*, 19773.

244. Wang, Z.; Liu, Z.; Gu, B.; Gao, B.; Wang, T.; Zheng, X.; Wang, G.; Guo, Q.; and Chen D. Ultraviolet light-driven controllable doping of graphene quantum dots with tunable emission wavelength for fluorescence bio-imaging. *Mater. Lett.* **2020**, *266*, 127468.

245. El-Shaheny, R.; Yoshida, S.; and Fuchigami, T. Graphene quantum dots as a nanoprobe for analysis of o- and p-nitrophenols in environmental water adopting conventional fluorometry and smartphone image processing-assisted paper-based analytical device. In-depth study of sensing mechanisms. *Michrochem.* **2020**, *158*, 105241.

246. Su, J.; Zhang, X.; Tong, X.; Wang, X.; Yang, P.; Yao, F.; Guo, R.; and Yuan, C. Preparation of graphene quantum dots with high quantum yield by a facile one-step method and applications for cell imaging. *Mater. Lett.* **2020**, *271*, 127806.

247. Fan, H.; Yu, X.; Wang, K.; Yin, Y.; Tang, Y.; Tang, Y.; and Liang, X. Graphene quantum dots (GQDs)-based nanomaterials for improving photodynamic therapy in cancer treatment. *Eur. J. Med. Chem.* **2019**, *182*, 111620.

248. Tabish, T.; Scotton, C.; Ferguson, D.; Lin, L.; van der Veen, A.; Lory, S.; Ali, M.; Jabeen, F.; Ali, M.; Winyard, P.; and Zhang, S. Biocompatibility and toxicity of graphene quantum dots for potential application in photodynamic therapy. *Nanomed.* **2018**, *13(15)*, 1923.

249. Aggarwal, V.; Singh Tuli, G.; Varol, A.; Thakral, F.; Betul Yerer, M.; Sak, K.; Varol, M.; Jain, A.; Khan, A.; and Sethi, G. Role of reactive oxygen species in cancer progression: molecular mechanisms and recent advancements. *Biomolecules.* **2019**, *9(11)*, 735.

250. Perillo,B.; Di Donato, M.; Pezone, A.; Di Zazzo, E.; Giovannelli, P.; Galasso, G.; Castoria, G.; and Migliaccio, A. ROS in cancer therapy: the bright side of the moon. *Exp. Mol. Med.* **2020**, *52*, 192.

251. Sarbadhikary, P.; George, B.; and Abrahamse, H. Recent advances in photosensitizers as multifunctional theranostic agents for imaging-guided photodynamic therapy of cancer. *Theranostics.* **2021**, *11(18)*, 9054.

252. Mroz, P.; Yaroslavsky, A.; Kharkwal, G.; and Hamblin, M. Cell death pathways in photodynamic therapy of cancer. *Cancers.* **2011**, *3(2)*, 2516.

253. Choi, S.; Baek, S.; Chang, S.; Song, Y.; Rafique, R.; Lee, K.; and Park, T. Synthesis of upconversion nanoparticles conjugated with graphene quantum dots and their use against cancer cell imaging and photodynamic therapy. *Biosens. Bioelectron.* **2017**, *93*, 267.

254. Li, Z.; Wang, D.; Xu, M.; Wang, J.; Hu, X.; Sadat, A.; Tedesco, A.; Morais, P.; and Bi, H. Fluorine-containing graphene quantum dots with a high singlet oxygen generation applied for photodynamic therapy. *J. Mater. Chem. B.* **2020**, *8*, 2598.

255. Wang, M.; Li, B.; Du, T.; Bu, H.; Tang, Y.; and Huang, Q. Fluorescence imaging-guided cancer photothermal therapy using polydopamine and graphene quantum dot-capped Prussian blue nanocubes. *RSC Adv.* **2021**, *11*, 8420.

256. Liu, Q.; Zhou, Y.; Li, M.; Zhao, L.; Ren, J.; Li, D.; Tan, Z.; Wang, K.; Li, H.; Hussain, M.; Zhang, L.; Shen, G.; Zhu, J.; and Tao, J. Polyethyleneimine hybrid thing-shell hollow mesoporous silica nanoparticles as vaccine self-adjuvants for cancer immunotherapy. *ACS Appl. Mater. Interfaces.* **2019**, *11*, 47798.

257. Möller, K.; and Bein, T. Degradable drug carriers: vanishing mesoporous silica nanoparticles. *Chem. Mater.* **2019**, *31*, 4364.

258. Zhang, B.; Liu, Q.; Liu, M.; Shi, P.; Zhu, L.; Zhang, L.; and Li, R. Biodegradable hybrid mesoporous silica nanoparticles for gene/chemo-synergetic therapy of breast cancer. *J. Biomater. Appl.* **2019**, *33(10)*, 1382.

259. Gao, F.; Wu, J.; Niu, S.; Sun, T.; Li, F.; Bai, Y.; Jin, L.; Lin, L.; Shi, Q.; Zhu, L.; and Du, L. Biodegradable, pH-sensitive hollow mesoporous organosilica nanoparticle (HMON) with controlled release of Pirfenidone and ultrasound-target-microbubble-destruction (UTMD) for pancreatic cancer treatment. *Theranostics.* **2019**, *9(20)*, 6002.

260. Lu, N.; Fan, W.; Yi, X.; Wang, S.; Wang, Z.; Tian, R.; Jacobson, O.; Liu, Y.; Yung, B.; Zhang, G.; Teng, Z.; Yang, K.; Zhang, M.; Niu, G.; Lu, G.; and Chen, X. Biodegradable hollow mesoporous organosilica nanotheranostics for mild hyperthermia-induced bubble-enhanced oxygen-sensitized radiotherapy. *ACS Nano.* **2018**, *12*, 1580.

261. Liberman, A.; Mendez, N.; Trogler, W.; and Kummel, A. Synthesis and surface functionalization of silica nanoparticles for nanomedicine. *Surf. Sci. Rep.* **2014**, *69*, 132.

262. Li, J.; Shen, S.; Kong, F.; Jiang, T.; Tang, C.; and Yin, C. Effects of pore size on *in vitro* and *in vivo* anticancer efficacies of mesoporous silica nanoparticles. *RSC Adv.* **2018**, *8*, 24633.

263. Gao, Y.; Zhong, S.; Xu, L.; He, S.; Dou, Y.; Zhao, S.; Chen, P.; and Cui, X. Mesoporous silica nanoparticles capped with graphene quantum dots as multifunctional drug carriers for photo-thermal and redox-responsive release. *Micropor. Mesopor. Mater.* **2019**, *278*, 130.

264. Vallet-Regí, M.; Colilla, M.; Izquierdo-Barba, I.; and Manzano, M. Mesoporous silica nanoparticles for drug delivery: current insights. *Molecules.* **2018**, *23*, 47.

265. Liu, J.; Luo, Z.; Zhang, J.; Luo, T.; Zhou, J.; Zhao, X.; and Cai, K. Hollow mesoporous silica nanoparticles facilitated drug delivery via cascade pH stimuli in tumor microenvironment for tumor therapy. *Biomaterials.* **2016**, *83*, 51.

266. Flak, D.; and Przysiecka, L. GQDs-MSNs nanocomposite nanoparticles for simultaneous intracellular drug delivery and fluorescent imaging. *J. Nanopart. Res.* **2018**, *20*, 306.

267. Dong, J.; Yao, X.; Sun, S.; Zhong, Y.; Qian, C.; and Yang, D.; In vivo targeting of breast cancer with a vasculature-specific GQDs/hMSN nanoplatform. *RSC Adv.* **2019**, *9*, 11576.

268. Dong, J.; Zhang, Y.; Guo, P.; Xu, H.; Wang, Y.; and Yang, D. GQDs/hMSN nanoplatform; singlet oxygen generation for photodynamic therapy. *J. Drug Deliv. Sci. Technol.* **2020**. *61(23)*, 102127.

269. Yang, D.; Yao, X.; Dong, J.; Wang, N.; Du, Y.; Sun, S.; Gao, L.; Zhong, Y.; Qian, C.; and Hong, H. Design and investigation of core/shell GQDs/hMSN nanoparticles as an enhanced drug delivery platform in triple-negative breast cancer. *Bioconjugate Chem.* **2018**, *29*, 2776.

270. Chen, F.; Gao, W.; Qui, X.; Zhang, H.; Liu, L.; Liao, P.; Fu, W.; and Luo, Y. Graphene quantum dots in biomedical applications: recent advances and future challenges. *Front. Lab. Med.* **2017**, *1*, 192.

271. Wang, Z.; Scheuring, M.; Mabin, M.; Shahni, R.; Wang, Z. D.; Ugrinov, A.; Butz, J.; and Chu, Q. R. Renewable cyclobutane-1,3-dicarboxylic acid (CBDA) building block synthesized from furfural via photocyclization. *ACS Sustainable Chem. Eng.* **2020**, *8*, 8909.

272. Han, Y.; Lu, Z.; Teng, Liang, J.; Guo, Z.; Wang, D.; Han, M.; and Yang, W. Unraveling the growth mechanism of silica particles in the Stöber method: in situ seeded growth model. *Langmuir*. **2017**, *33(23)*, 5879.

273. Britannica, https://www.britannica.com/science/nanoparticle, accessed 20 April 2022.

274. Bharti, C.; Nagaich, U.; Pal, A.; and Gulati, N. Mesoporous silica nanoparticles in target drug delivery system: a review. *Int. J. Pharm. Investig.* **2015**, *5(3)*, 124.

275. Shang, L.; Nienhaus, K.; and Nienhaus, G. Engineered nanoparticles interaction with cells: size matters. *J. Nanobiotechnol.* **2014**, *12*, 5.

276. Zhang, D.; Wei, L.; Zhong, M.; Xiao, L.; Li, H.; and Wang, J. The morphology and surface charge-dependent cellular uptake efficiency of upconversion nanostructures revealed by single-particle optical microscopy. *Chem. Sci.* **2018**, *9*, 5260.

277. Fröhlich, E. The role of surface charge in cellular uptake and cytotoxicity of medical nanoparticles. *Int. J. Nanomed.* **2012**, *7*, 5577.

278. Sivasubramanian, M.; Chuang, Y.; and Lo, L. Evolution of nanoparticle-mediated photodynamic therapy: from superficial to deep-seated cancers. *Molecules.* **2019**, *24(3)*, 520.

279. Jovanovic, S.; Syrgiannis, Z.; Budimir, M.; Milivojevic, D.; Jovanovic, D.; Pavlovic, V.; Papan, J.; Bartenwerfer, M.; Mojsin, M.; Stevanovic, M.; and Todorovic Markovic, B. Graphene quantum dots as singlet oxygen producer or radical quencher – the matter of functionalization with urea/thiourea. *Mater. Sci. Eng. C.* **2020**, *109*, 110539.

280. Guo, H.; Qian, H.; Sun, S.; Sun, D.; Yin, H.; Cai, X.; Liu, Z.; Wu, J.; Jiang, T.; Liu, X. Hollow mesoporous silica nanoparticles for intracellular delivery of fluorescent dye. *Chem. Cent. J.* **2011**, *5:1*.

281. Lu, N.; Fan, W.; Yi, X.; Wang, S.; Wang, Z.; Tian, R.; Jacobson, O.; Liu, Y.; Yung, B.; Zhang, G.; Teng, Z.; Yang, K.; Zhang, M.; Niu, G.; Lu, G.; and Chen, X. Biodegradable hollow mesoporous organosilica nanotheranostics for mild hyperthermia-induced bubble-enhanced oxygen-sensitized radiotherapy. *ACS Nano.* **2018**, *12*, 1580.

282. Zhang, B.; Liu, Q.; Liu, M.; Shi, P.; Zhu, L.; Zhang, L.; and Li, R. Biodegradable hybrid mesoporous silica nanoparticles for gene/chem-synergetic therapy of breasts cancer. *J. Biomater. Appl.* **2019**, *33(10)*, 1382.

283. Zhou, Y.; Chang, C.; Liu, Z.; Zhao, Q.; Xu, Q.; Li, C.; Chen, Y.; Zhang, Y.; and Lu, B. Hyaluronic acid-functionalized hollow mesoporous silica nanoparticles as pH-sensitive nanocarriers for cancer chemo-photodynamic therapy. *Langmuir.* **2021**, *37*, 2619.

284. Croissant, J.; and Brinker, C. Biodegradable silica-based nanoparticles: dissolution kinetics and selective bond cleavage. *Enzymes.* **2018**, *43*, 181.

285. Kong, M.; Tang, J.; Qiao, Q.; Wu, T.; Qi, Y.; Tan, S.; Gao, X.; and Zhang, Z. Biodegradable hollow mesoporous silica nanoparticles for regulating tumor microenvironment and enhancing antitumor efficiency. *Theranostics.* **2017**, *7(13)*, 3276.

286. Sukhanova, A.; Bozrova, S.; Sokolov, P.; Berestovoy, M.; Karaulov, A.; and Nabiev, I. Dependence of nanoparticle toxicity on their physical and chemical properties. *Nanoscale Res. Lett.* **2018**, *13*, 44.

287. Beganskiene, A.; Sirutkaitis, V.; Kurtinaitiene, M.; Juskenas, R.; and Kareiva, A. FTIR, TEM, and NMR investigations of Stöber silica nanoparticles. *J. Drug Deliv. Sci. Technol.* **2004**, *10*, 287.

288. Mehmood, Y.; Khan, I.; Shahzad, Y.; Khalid, S.; Asghar, S.; Irfan, M.; Asif, M.; Khalid, I.; Yousaf, A.; and Hussain, T. Facile synthesis of mesoporous silica nanoparticles using modified sol-gel method: optimization and in vitro cytotoxicity studies. *Pak. J. Pharm. Sci.* **2019**, *32*, 1805.

289. Rameli, N.; Jumbri, K.; Wahab, R.; Ramli, A.; and Huyop, F. Synthesis and characterization of mesoporous silica nanoparticles using ionic liquids as a template. *J. Phys.: Conf. Ser.* **2018**, *1123*, 012068.

290. Fang, J.; Liu, Y.; Chen, Y.; Ouyang, D.; Yang, G.; and Yu, T. Graphene quantum dots-gated hollow mesoporous carbon nanoplatform targetinging drug delivery and synergistic chemo-photothermal therapy. *Int. J. Nanomed.* **2018**, *13*, 5991.

291. Yao, X.; Tian, Z.; Liu, J.; Zhu, Y.; and Hanagata, N. Mesoporous silica nanoparticles capped with graphene quantum dots for potential chemo-photothermal synergistic cancer therapy. L*angmuir*. **2017**, *33*, 591.

292. Hao, N.; Jayawardana, K.; Chen, X.; De Zoysa, T.; and Yan, M. One-step synthesis of amine-functionalized hollow mesoporous silica nanoparticles as efficient antibacterial and anticancer materials. *ACS Appl. Mater. Inter.* **2015**, *7(2)*, 1040.